Human Powered Aircraft Group
at Virginia Tech
presents

The Iron Butterfly

A Human Powered Aircraft for Sport

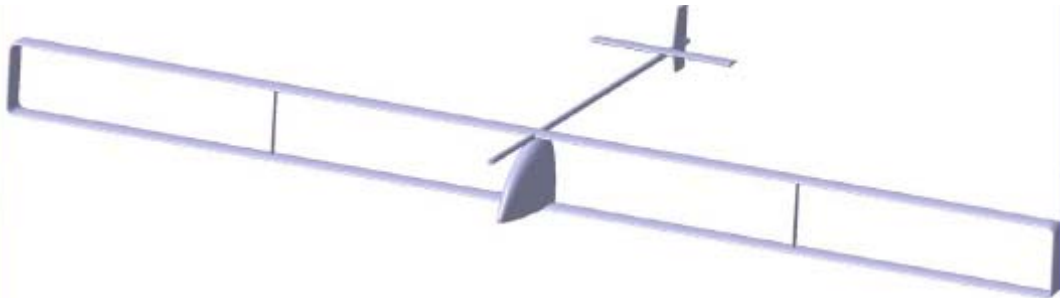

Aerospace and Ocean Engineering Department
Virginia Polytechnic Institute and State University

May 4, 2005

Team Members:

Chris Emory
Imraan Faruque
Matthew Janeway
Blake Jeans
Jason Roadman
Lee Skidmore
Wesley Slemp

Contents

1. Executive Summary

1.1 Conceptual Design

The first phase in the design process was conceptual design. The team thoroughly went over the rules for the Kremer Human Powered Aircraft (HPA) for Sport Prize. A mission analysis was performed to indicate how the airplane would need to perform. A set of design constraints was defined based on the rules, the mission analysis, and the capability of a human propulsion and control system. Given the design constraints, each team member developed a basic concept. The team evaluated the concepts and ranked them in a design matrix based on a number of criteria deemed important for a successful design.

1.2 Aerodynamics

Preliminary aerodynamic analysis began with a comparison between the top two conceptual designs. With a boxplane design coming out on top, airfoils were researched and the best options were selected. The wing area was then selected through a constraint analysis based on the design requirements. The drag of the design was analyzed in detail. The wing and tail surfaces were shaped and configured to give the most functional and lowest drag configuration.

1.3 Structures

The structural analysis began with a comparison between a monoplane and a biplane wing structure. Some simple models were built and tested. When the biplane model proved superior an analytical structural solution was created. Finite element analysis was used to further analyze and refine the structural design. The finite element analysis results were validated using the data from the simple biplane structure model tests. The number of struts on each wing was determined with a trade study considering mostly drag. The gap between the wings was determined through parametric study with the goal of minimizing drag. The materials were selected and the structural configuration was developed based on constraints which were set for the final structural design.

1.4 Stability and Control

Evaluation of stability and control began with defining detailed requirements for the airplane. The longitudinal stability and control characteristics were assessed first, followed by the lateral and directional. An initial control scheme derived from examination of similar aircraft was developed. The control surfaces were sized analytically. The aircraft dihedral was selected through parametric study of a simplified layout using a vortex lattice code. Finally, a more detailed model was developed to preform final verification of compliance with the requirements.

1.5 Human Propulsion

To gain a better understanding of the propulsion system for the airplane, human power production was researched. Learning that the process by which power was being produced for the airplane was about 25% efficient, a cooling system was designed for the cockpit to remove excess heat. A bicycle like drive train was designed to get the power from the pilot's legs to the aircraft's propeller. Research was conducted to determine the best pilot position and a seat was designed to accomodate this position.

1.6 Propeller Design

A propeller was designed using several methods to get very efficient power production at the design conditions. A automatic pitch controller was designed to regulate the propeller pitch to get the optimum performance at various flight conditions.

1.7 R/C Model Development

A quarter scale R/C model was designed to evaluate the dynamic stability and control of the model. The model was Froude scaled so it would behave dynamically similar to the full scale aircraft. The wing wing designed so it would perform like the the full scale wing. The structure was designed overly rigid to remove some aeroelastic effects and built with some artificial deflection so the deflection in flight would be the same for the quarter and full scale. Since the model was Froude scaled, it should behave dynamically similarly; however, the dynamic and control similarity was analyzed for verification. Some simple flight tests were conducted and some fixable problems were encountered.

2. Background and Narrative

The catalyst for most human-powered aircraft (HPA) activity for the past 40 years or so has been the Kremer Prizes offered by the Royal Aeronautical Society. The competitions have dictated the design criteria for most HPAs since the advent of the prize in 1959. The requirement of this first prize was to fly a figure-8 course. The completion of the objectives set out by the different prizes has separated the many failed HPA from the successful ones. The first successful HPA was Paul McCready's Gossamer Condor which won the first Kremer Prize in 1977 a whole 18 years after the prize had been introduced[1]. Many of the early attempts at HPA were based on emulating sailplanes. McCready changed the direction and expanded on the concepts used in hang-gilders to create his successful HPA. The major change in thought then went from trying to add human-power to sailplanes to creating extremely light airplanes.

McCready also won the next Kremer Cross Channel Prize only two years later in 1979[1]. The Gossamer Albatross was the plane his team created to cross the English Channel. Five years later the RAS offered a new prize for a speed aircraft. With a bit of a departure from the previous rules, the speed aircraft rules allowed for ten minutes of energy storage by the pilot just prior to the flight. There were two main competitors for the speed prize, again McCready and now a group of students from MIT. McCready's team designed the Bionic Bat and managed to attempt to fly the course before the MIT team. The attempt was initially declared successful; however, the officials governing the competition decided that McCready's method for proving the batters he used for energy storage only had the pilot's energy stored in them was not sufficient and the attempt was made void. McCready's team then departed from the energy storage method all together and attempted to modify the plane to do the lap in time under human power alone. The MIT group took this opportunity and adapted to the method for proving the batteries to be dead and successfully flew their entry Monarch to win the prize.

There have additionally been several non-Kremer entry successful HPAs. One of the earliest successful designs other than those by McCready was Chrysalis. It was a biplane designed by a group of MIT students in the late '70s. MIT also did a project to recreate the mythical flight of Daedalus from the island of Crete. The prototype for this project, called the Michelob Light Eagle, as well as two Daedalus aircraft, 88 and 89, were constructed. Germany has also had a few successful HPA the Velair 89 as well as the Musculair 1 and 2[2].

The designs of many of the successful HPA have several similar characteristics. Table 2.1 details some of the design points on all of the aircraft mentioned. The first and very important similarity is the pilot seating position. In all but the Condor, the pilot is seated in a recumbent position. This position proves to be much better for power production than the upright position. Another important similarity is the aft tail on all but the two Gossamer aircraft. This is likely for aerodynamic efficiency. With the exception of Chrysalis which was a biplane, all the planes have high and generally straight wings. The reason for high wings is likely prop clearance and possibly structure. One similarity between most the control systems is an all flying tail, many of them with anti-servo tabs. Most the planes have some type of ailerons. The main one that did not was Daedalus. They were cut from Daedalus to remove a small amount of weight and since the mission of Daedalus involved almost no turning they did not really seem necessary. There is a fairly even mixed bag when it comes to tractor or pusher prop configuration. All the MIT planes are tractors while all the other planes are pushers. In the table, the span of the Monarch is bolded because it is not like the others in the fact that it is much smaller. The Monarch had to fly the same course as the current Kremer prize requires where most the other planes with larger spans were for endurance.

The new set of rules for the Kremer Sport Prize contains one major difference from all the previous prizes. It has a minimum wind velocity required during the prize flight. As a result of this

Table 2.1. Comparison Table for previous HPAs

Span [ft]	Gossamer Condor 95	Gossamer Albatross 95	Chrysalis 72	Bionic Bat ?	Monarch 62	Daedalus 112	Velair 76	Musculair 64
Arrangment	high swept	high swept	biplane	high straight	high straight	high straight	high straight	high straight
Pilot Pos.	upright	recumbent	recumbent	recumbent	recumbent	recumbent	recumbent	recumbent
Tail Config.	forward	forward	aft	aft	aft	aft	aft	aft
Prop Pos.	pusher	pusher	tractor	pusher	tractor	tractor	pusher	pusher
Roll Control	wing warping	wing warping	wing warping	ailerons	ailerons	secondary	rotating tips	aileron

wind requirement the plane will have to have a significantly higher indicated airspeed. The plane will also have to be more docile to be able to deal with the two crosswind legs of the flight. The plane has to have a quick assembly and disassembly and be stored in a trailer of specified maximum size. The speed required due to the wind will likely require a smaller airplane than the previous prizes. The plane will have to be even lower drag and lighter than the previous aircraft. The prize flight will likely require a very well trained athlete capable of producing the higher power that will be needed to attain the required ground speed. The new plane will also need to make tighter turns so it does not have to fly a great bit further than the unreachable minimum of 1500 m. Considering the timed assembly and disassembly the structural and control linkages will have to be as simple as possible. All in all, to win the new prize a next step will have to be taken in the performance level of the airplane.

3. Conceptual Design

3.1 Mission Analysis

This aircraft was designed for the Kremer Sport Prize, whose rules are available from the Human Powered Aircraft Group of the Royal Aeronautical Society[1]. After careful examination of these rules, several key considerations were identified: complete of a 4920 ft long, triangular course in both directions in 7 min or less, cross the start/finish line at a minimum altitude of 16.4 ft, have low initial and repair costs, assemble within 30 min from a 26.4 ft long trailer, and be suitable for small batch or kit production.

A vital component of mission success is the identification of how the course must be flown. The Kremer Sport Competition rules state that the vehicle must fly about a course consisting of markers placed in an equilateral triangle with 1640 ft long sides. This flight must be conducted in both directions with wind speeds not less than 16.4 ft/sec (11.2 mph). See Fig. 3.1. During the flights, the vehicle must cross the start/finish line with a minimum height of 16.4 ft. Both flights must be completed in a total time of 7 min. A 1 hr recovery break is permitted between flights.

The designer is given the freedom to choose the specific path through which the HPA navigates the course and the speed and bank angle at which this must be conducted. This is an important consideration since the shortest path is not necessarily the quickest and may not even be possible. All HPAs to date have had severely limited roll control. To quantitatively identify the constraints that this course imposed on a vehicle, a reasonable, but not optimum, path was chosen through it, as shown in Fig. 3.1. The chosen path is more demanding than the optimum, to ensure a margin of safety with respect to time and performance. A vehicle designed to successfully navigate the chosen path within the specified time should be capable of completing a more optimum path in less time.

This mission can generally be then described as takeoff and climb, the three legs of the triangle,

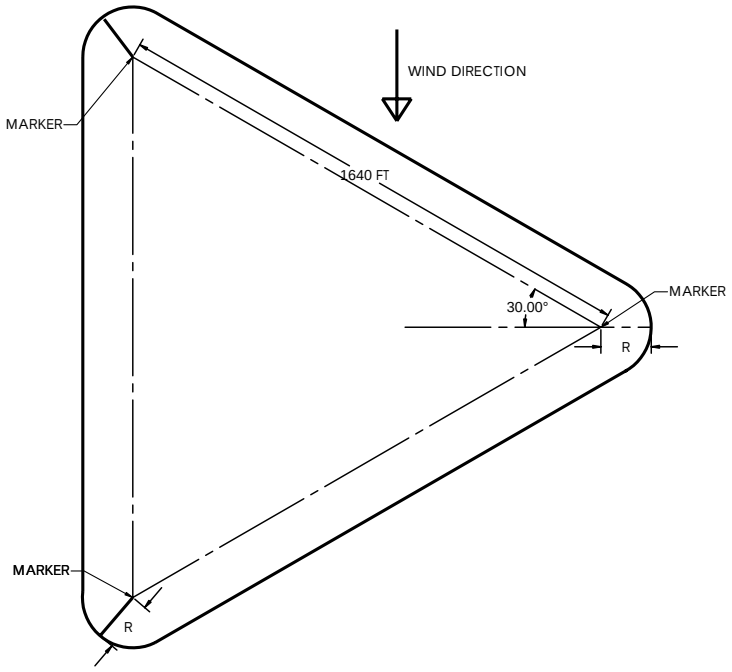

Figure 3.1. Kremer Sport Prize geometry and path.

the turns, and landing. Since the three straight legs and turns are the timed portion of the flight, this was the area of focus during mission analysis. Basic aircraft performance equations were used to model the vehicle's travel about the specified course. The ground speed v_g of an aircraft traveling along the straight legs can be found using the indicated airspeed v, the wind speed w, and the angle relative to the reference line θ. The ground speed can be found by the law of cosines to be:

$$v_g = w\cos(\theta) + \sqrt{w^2\cos^2(\theta) - w^2 + v^2} \tag{3.1}$$

The distance in the turns is a function of the turning radius, which can be found from the bank angle, direction, and flight speed. The turn radius equation is shown in Eq. (3.2), where a turn radius R is specified by the flight velocity v and the bank angle under the influence of gravity g. The average ground speed through these turns was based on the mean value theorem performed on vehicle heading with respect to wind.

$$R = \frac{v^2}{g\tan(\phi)} \tag{3.2}$$

A plot of course time vs. flight speed over a range of bank angles was constructed and is shown in Fig. 3.2. A hashed horizontal line was drawn at 7 min to mark the course deadline. While the time required to complete the course reduces with increasing bank angle, there is a point of

diminishing returns and there is little time savings for a bank angle greater than 15 deg. A bank angle this great substantially increases the loads, height, and control moments required for flight. Accordingly, the vehicle was constrained to fly at a velocity of 33ft/s (22.5 mph) and be capable of banking at 15 deg.

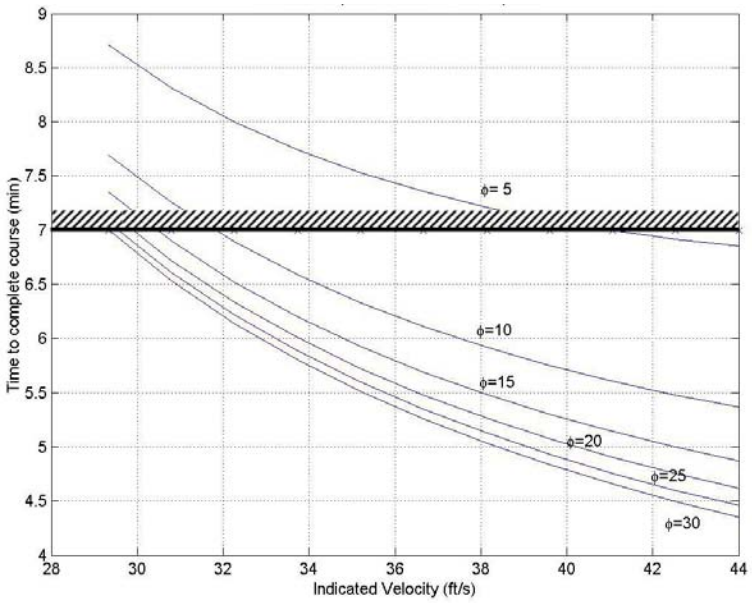

Figure 3.2. Speed, bank angle, and time required to complete course.

The idea behind the sport prize is to make HPAs more practical so that they may be created as a kit and assembled by a hobbyist at relatively low cost. Accordingly, it must be transported in a 26.4 ft maximum length trailer, and subsequently be assembled and ready to fly in less than 30 min. This puts limitations on the size of the aircraft, which must obviously be less than the inside length of the trailer. First, the Code of Virginia was consulted to ensure that a 26.4 ft long trailer was below the legal length limitation in the area in which it would be constructed. Aircraft length and wing panels were restricted to a maximum of 26 ft.

In summary, analysis of the mission creates the following constraints on the human powered airplane: a cruise speed of 33 ft/s or greater, a bank angle capability of 15 deg (in reasonable time), a maximum part length of 26 ft, and a maximum wingspan of 60 ft. Additionally, emphasis is placed on simplicity of construction to allow fast assembly.

3.2 Conceptual Configurations

With the results of the mission analysis and design constraints defined, each team member developed a conceptual design. Each unique viewpoint developed a unique concept configuration. Each configuration focused on different aspects required to complete the mission.

3.2.1 Feathers

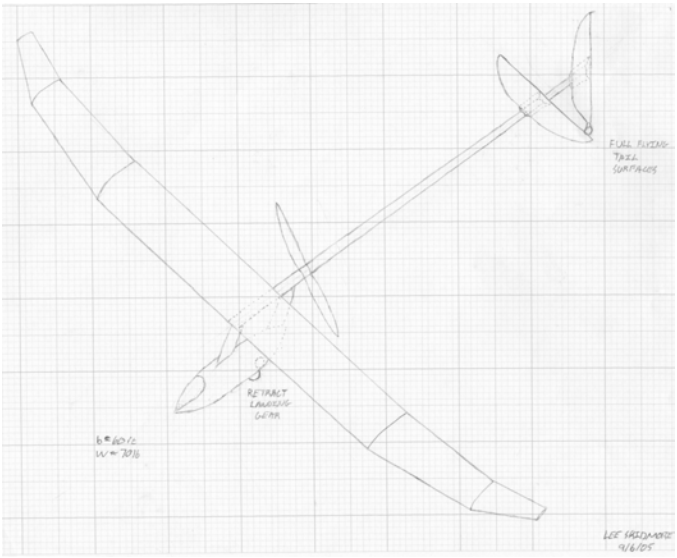

Figure 3.3. Sketch of Feathers concept.

The Feathers concept focuses solely on drag reduction. The wing planform is derived from high-performance sailplane configurations with high aspect ratio wings that reduce span loading and a triple-taper wing to approximate the "aerodynamically ideal" elliptical lift distribution. These two features minimize induced drag. The fuselage is a small pod just large enough to contain the pilot and mechanical components. The small pod has minimal area to reduce friction drag and a streamlined shape to reduce form drag. By mounting the wing on two small pylons, interference drag between the fuselage and the wing is minimized. This approach has been proven effective with world class Radio Controlled (R/C) sailplanes. Continuing to follow R/C sailplane design techniques the tail surfaces are fully flying and mounted to pylons attached to a long boom. The long tail moment arm reduces the required tail area and tail loads, thereby minimizing friction and induced drag. An unusual feature of this concept is the boom-centric propeller. This allows the wing and fuselage to operate in undisturbed air which reduces friction drag. The center wing sees increased air velocity while the tails operate in accelerated flow from the propeller increasing low speed control authority. Conversely, boom-centric propeller is mechanically difficult.

The Feathers concept has potential for very low drag. However, obtaining this low drag requires a large wingspan that is detrimental to turning performance and trailer space utilization. The pod-style fuselage also presents construction challenges and the attachment pylons may not be structurally efficient once landing conditions are considered. Due to trailer length limitations, the long tail boom requires two piece construction adding additional weight and structural complexity. While Feathers is very efficient aerodynamically, structural and practical construction

considerations negate these advantages.

3.2.2 Squished Bat

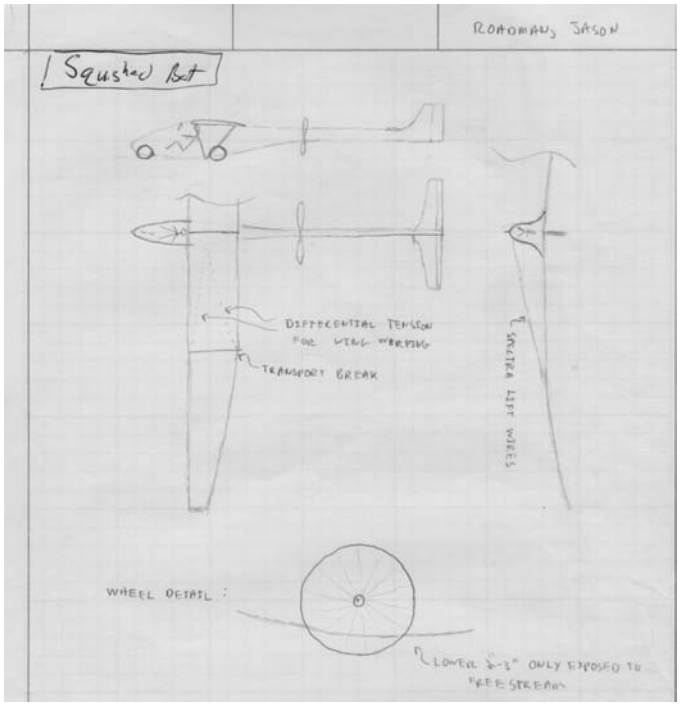

Figure 3.4. Squished Bat Concept sketch.

The Squished Bat concept was investigated in an attempt to build upon the success of Paul MacCready's Bionic Bat. The Bionic Bat was an HPA designed to fly a course similar to the Kremer Sport Prize; however, it utilized electronic power to supplement the pilot. The relatively simple and proven monoplane design was chosen to minimize aircraft drag and maximize overall efficiency. This also simplified aerodynamic and structural analysis.

For this concept, the Bionic Bat design was modified by shrinking the height of the fuselage in an attempt to further reduce its associated drag. The pilot is placed in a recumbent position with the top of his head flush with the top of the wing. Landing gear are placed fore and aft of the pilot, further reducing fuselage height. Placing the pilot in a more reclined position limits frontal area; however, a more upright riding style would allow for visibility.

Additionally, roll control through wing warping could be employed reducing the amount of sideslip and associated drag necessary in a turn. Two flying wires per wing would be used with separate mounting points along the chord. Differential tension in the wires would thereby twist the wings. The added drag from the flying wires is detrimental to performance.

3.2.3 Duck

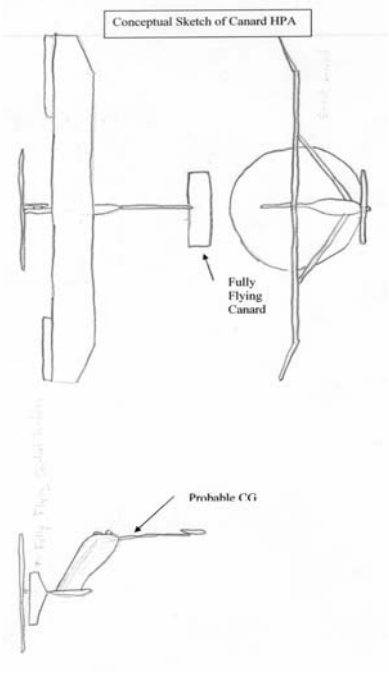

Figure 3.5. Duck.

The Duck concept was developed to be very similar to the Gossamer Condor, the first HPA to win a Kremer Prize[3]. The most distinguishing feature of the Duck was its use of a forward canard to balance and control the airplane. The design uses flying wires to twist the wing and tilt the canard. The tilted canard generates a yaw moment and a secondary roll moment due to roll-yaw coupling. Gossamer Condor's success has proven the control system to be effective. Further, the high wing and canard placement provide the pilot with improved visibility in flight.

The design exhibits poor aerodynamic efficiency due to the required flying wires. The need for flying wires to twist the wing increases the parasite drag. The uniqueness of the roll control scheme complicates control analysis. Stability restricts the wings lifting capabilities. While the Gossamer Condor met its design goals, it flew much slower than required for the Sport Prize.

3.2.4 Bert

The concept called Bert was an attempt to get the most use possible out of every part of the airplane. It had a tandem wing design where the area used for lifting was also used for longitudinal stability and control. The front lifting surface was made larger so it would carry more aerodynamic load to minimize induced drag. The larger front wing was drawn with a high aspect ratio to maximize aerodynamic efficiency. The smaller aft wing held all the controls for pitch and roll so

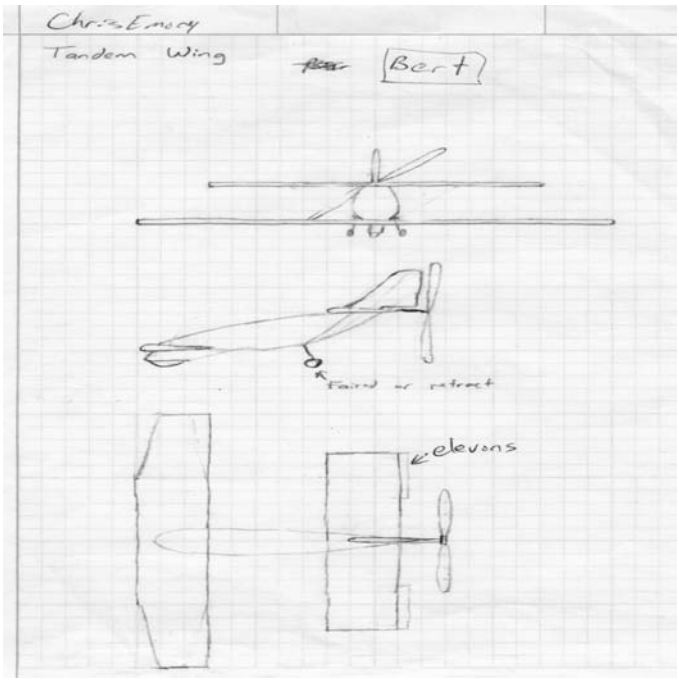

Figure 3.6. Tandem wing concept referred to as "Bert.".

the structure in the larger wing did not have to carry control loads. Roll controls on the smaller wing would have to be larger or deflected more, but would also require less structure due to the shorter moment arm. The fuselage was used to connect the two wings as well as house the pilot. The propeller was placed at the rear of the aircraft because it was the most convenient place, it kept the wings, fuselage, and controls in clean air flow, and it allowed the most propeller clearance.

The Bert concept had aerodynamic advantages because of the non-planar lifting configuration. It also posed the potential for low drag since it did not have a long tail boom and tail surfaces. Since all the load paths were short and direct, it had potential for a very light structure. The highly exposed fuselage would make it very easy to get the pilot inside and give the pilot better visibility. The drawback to the Bert design was that all the advantages would come from a great deal of work and were not guaranteed. The configuration would be complicated and difficult to analyze for aerodynamics and stability. With two separate wings that would need to be broken down to fit into the trailer, assembly was more complicated. Construction and structural analysis would also be difficult with the complex way the fuselage tied into the wings.

3.2.5 Fighting Fish

The fighting fish concept was developed by designing the aircraft around the ideal for the propulsion system. The pilot's position was first established and the rest of the aircraft was shaped around the pilot. The wing was placed above the cockpit to provide good visibility and increase the roll

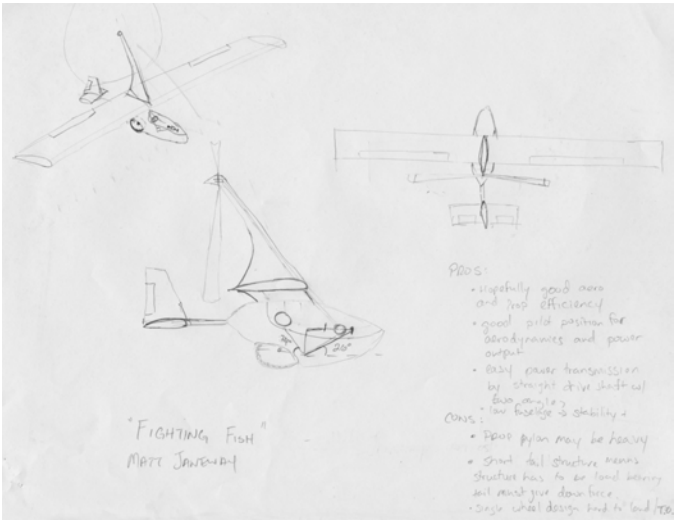

Figure 3.7. Fighting Fish concept sketch.

stiffness of the aircraft in the hope that the pilot need not concentrate extensively on flying while pedaling. Horizontal and vertical tails were placed in their conventional locations for simplicity of analysis. To fit a large propeller above the tail boom and to keep it out of the effects of the fuselage wake, a large propeller boom was designed above the wing. Finally, landing gear was added fore and aft of the pilot's seat to easily support the center of gravity.

Unfortunately, several negative issues become apparent quickly when analyzing this concept. First, the large propeller boom adds a significant amount of unwanted structure and weight. Placing the center of the propeller this high above the centerline of the aircraft also produces a very significant nose down pitching moment. Secondly, placing the propeller in this high position complicates the drive train by forcing two axis-of-rotation angle changes. Other designs only require one axis-of-rotation angle change of 90 deg.

3.2.6 Bipolar

The concept known as Bipolar was a biplane concept inspired by MIT's Chrysalis and resulted from a realization of the decrease in induced drag achieved with a biplane over a monoplane. A large span is desired to create a low drag profile. If an aircraft's span is limited to less than the optimum monoplane span, then a biplane configuration should be considered because it increases the effective aspect ratio. A biplane configuration also reduces the Reynolds number across the wing by reduction of the chord (versus the monoplane) aiding in the reduction of friction drag. This vehicle was envisioned to have full-flying tail surfaces to reduce the size and complexity thus reducing the total weight and assembly time of the surfaces. Struts placed between the wings to reduce the required weight of the spar structure and impose a smaller drag penalty than flying

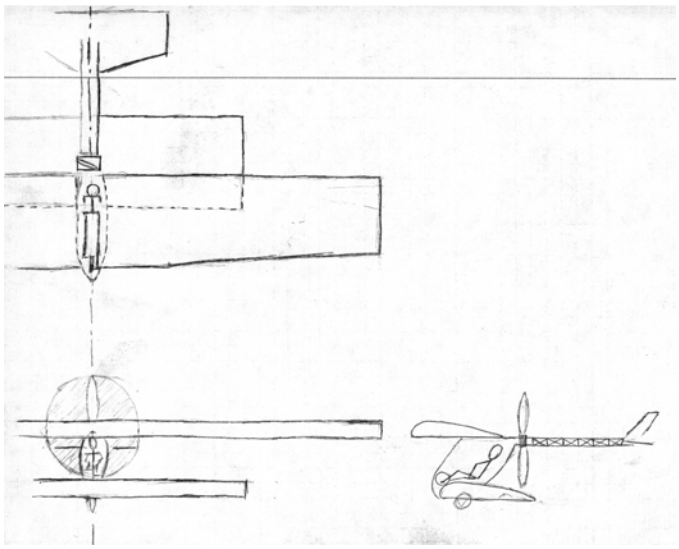

Figure 3.8. Conceptual sketch of Bipolar.

wires. A lightweight carbon-fiber or aluminum tail boom joins the fuselage to the tail.

Additionally, the tractor propeller configuration was selected for three reasons. First, the need for a large diameter prop to maintain efficiency means that the aft-mounted pusher prop would need to be mounted as high as possible, presumably boom-centric. A boom-centric propeller is mechanically complex and can easily be avoided with a tractor propeller. Second, in this configuration the propeller is presented with clean and undisturbed air flow which is required for its efficient operation. The final advantage to a tractor mounted propeller is the ram-air effect afforded to a pilot cooling duct on the fuselage.

There are disadvantages to this design. A biplane has lower induced drag only if the vehicle must have a limited span. At the time this concept was conceived, it was not clear whether the optimum span would be greater than that available with a three-piece monoplane wing span of 60 ft. There is the added task of fabricating two wings, and the fuselage must be stiffened between the wings. Analysis is more complicated leading to a potential for more errors. The lower wing offers less ground clearance and constrains low-altitude bank angles more than a high wing aircraft; however, adding dihedral to the lower wing could help remedy this problem. Finally, the ideal gap (vertical separation between the wings) is infinite, meaning that a taller fuselage is preferred aerodynamically.

3.3 Figure of Merit based Concept Selection

To objectively evaluate the relative capability of the concepts presented, a figure of merit system was used. The Feathers concept selected as the baseline because of its traditional layout. This

concept was then given the reference score of zero and all other concepts were benchmarked against it. In each category, a design was assigned a plus one if better than the reference, a minus one if worse, and a zero if there was no real difference. In the case of outstandingly superior performance in a category, a score of two might be assigned, but this was done sparingly. The concepts were rated on the basis of the following factors:

1. Efficiency of structure: This score was based on the subjective interpretation of how well structure (and hence mass) was utilized on the vehicle. Does the structure serve multiple purposes? Are the load paths clearly delineated and in areas of natural reinforcement?
2. Efficiency of aerodynamics: This score was based on how well the concept was expected to perform with respect to both skin friction and induced drag. For example, items with more protruding surfaces such as flying wires received lower scores here.
3. Trailer fitting/ease of assembly: This score reflects the vehicle's ease of assembly. Concepts which integrate extensive cross-bracing and have a high number of parts received lower scores here.
4. Simplicity of construction: As per the Kremer Prize rules the design must be suitable for batch production or assembly from a kit. This category evaluated each concept's ease of construction.
5. Wind tolerance: This was an assessment of the total vertical surface area as well as the ratio of vertical surface area ahead of the concept's aerodynamic center versus the vertical surface area aft of the aerodynamic center.
6. Simplicity of structure: Created to assess the relative complexity of the structure; therefore, the complexity of analyzing each structure. Straightforward concepts receive higher scores here.
7. Simplicity of stability and control: This was a measure of the difficulty in analyzing the stability and control of the design. More traditional design received better scores in this category.
8. Inherent stability: Due to the need for high power output from the pilot, natural stability will be required for ease of piloting. This category assessed the natural stability of the design.
9. Pilot integration: How well does the pilot fit into the design? The ideal concept is one where the natural structure defines a suitable place for the pilot to comfortably sit and pedal. This area also considered the relative ease with which the pilot could be loaded and unloaded (an area that has historically presented difficulty in many HPAs).
10. Propulsive adaptability and efficiency: This area considered the ease with which the drive train could be routed throughout the vehicle, and a propeller mounted. Short, direct drivelines

were preferred for lower weight and losses. Designs scored lower if the design required that the propeller be either a tractor or pusher.

11. Pilot visibility: Kremer Sport Prize rules stipulate that the pilot may not be assisted via radio from the ground. It is essential that the pilot have a good view of the surrounding area and good reference marks such that he or she can quickly ascertain the altitude and attitude of the aircraft to control it.

3.4 Conclusions

Based on the figure of merit evaluation scheme, two concepts were selected for further development: Feathers and Bipolar. Bipolar was clearly the leader in the concept scoring matrix (Table 3.1) and represented what the team believed was the most promising concept. Feathers was retained for continued analysis both for completeness and because the biplane configuration was new to the analysis team. If a more detailed analysis revealed that Bipolar was not as promising as initially thought, Feathers would be ready for continued design.

Evaluation of why the other vehicles were rejected shows little in the way of trends. The fact that the rejected concepts were all given negative scores in the category stability and control simplicity is apparent, as is the superiority of each of those designs in the area of pilot visibility.

The biplane concept emerged as the most viable concept and eventually developed into three concepts. These concepts are a biplane with the same span as the comparable monoplane (60 ft), a biplane that takes advantage of the effective aerodynamic increase in span and reduces its geometric span to 45 ft, and a final derivative concept, a “boxplane”. The boxplane concept, or Iron Butterfly as it has come to be known, is essentially a biplane with two winglets that extend the full length of the gap between the wings, forming an endplate at the wingtips. This concept can be seen in Fig. 3.9.

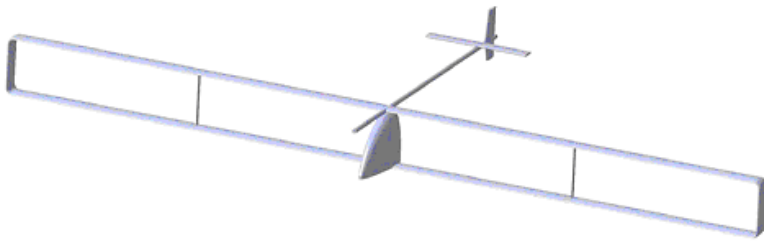

Figure 3.9. Iron Butterfly preferred concept.

While the boxplane concept introduces slightly more complexity, it also presents several advantages over any of the designs already discussed. The endplates have a beneficial induced drag reduction and are structural members that can carry enough load to significantly reduce the weight

Table 3.1. Figure of merit concept comparison relative to Feathers

Concept	Weight		Bipolar		Duck		Stealth		Bert		Fighting Fish	
Efficiency of Structure	5	1	5	-1	-5	-1	-5	1	5	-1	-5	
Efficiency of Aerodynamics	5	2	10	-1	-5	1	5	1	5	0	0	
Trailer Fitting/Ease of Assembly	5	-1	-5	0	0	-2	-10	-1	-5	-1	-5	
Simplicity of Aerodynamics	4	-1	-4	0	0	-1	-4	-1	-4	0	0	
Simplicity of Construction	4	0	0	0	0	1	4	-1	-4	-1	-4	
Wind Tolerance	4	1	4	-1	-4	-2	-8	0	0	-1	-4	
Simplicity of Structure	3	0	0	0	0	0	0	-1	-3	-1	-3	
Simplicity of Stability and Control	3	0	0	-1	-3	-2	-6	-2	-6	-1	-3	
Inherent Stability	3	-1	-3	-1	-3	-2	-6	1	3	0	0	
Pilot Integration	3	-1	-3	0	0	1	3	1	3	2	6	
Propulsive Adaptability/Efficiency	2	1	2	-1	-2	-1	-2	-1	-2	2	4	
Pilot Visibility	1	-1	-1	1	1	1	1	1	1	1	1	
Total			**5**		**-21**		**-28**		**-7**		**-13**	

of the spars used. Feathers, Iron Butterfly, and two biplane configurations were passed on to preliminary design.

4. Aerodynamics

4.1 Drag Analysis of Conceptual Designs

With the initial concepts reduced to a monoplane, two biplanes, and a boxplane, an analysis was required to arrive at a final concept. Because of the human power limit, drag becomes the most important attribute to be considered. The drag of the different concepts is largely dependent on the efficiency of the main wings; therefore, the tail moment arms, fuselage, and drag due to propulsion are assumed to be equal for all concepts. This simplified the drag analysis considerably. For analysis purposes, drag was catagorized into three main components: induced, friction and form, and interference.

A series of assumptions was made to conduct a simplified drag analysis. Based on previous HPAs, gross takeoff weight was estimated to be about 215 lb. This allows for a 150 lb pilot and 65 lb for the aircraft. The requirements for good turning performance and trailer limitations constrain the wingspan to 60 ft. To obtain a realistic C_L of about 0.8 for a cruise velocity of 33 ft/s the preliminary wing area was assumed to be 215 ft^2. The actual airfoil to be used is ignored in the preliminary drag analysis but the thickness is still required for an accurate drag analysis and is assumed to be 12%. This thickness allows for adequate structure and from previous airfoil experience was determined to be realistic. Without knowledge of the loading of the wing and the structural requirements the struts were given an arbitrary thickness of 20% and a chord of 5 in and the endplates were given a thickness of 12% and a chord equal to the wing chord.

Also, the horizontal tail volume coefficient was assumed to be 0.5, and the vertical tail volume coefficient was assumed to be 0.035 based on that used on Monarch[2]. To maintain an efficient tail, the aspect ratio of the horizontal and vertical tail was assumed to be 7 and the thickness of the tails was set at 12%. The tail surfaces for each concept were now fully defined and the only configuration dimension still required is the gap for the biplane and boxplane configurations. With the pilot in a recumbent position it was determined that a minimum gap of 54 in was required to fit the pilot and mechanics within the fuselage and so the gap was set to 54 in for both the biplanes and boxplane.

Induced drag is the drag that results from the production of lift. Induced drag is directly proportional to the strength of the wing trailing vortices and any reduction in the vortices will result in a reduction in induced drag. It is due to the reduction of these vortices that the biplane and boxplane configurations are considered. Because a biplane can affect a larger volume of air than a monoplane it is able to impart a smaller average velocity change to the air and therefore has less induced drag than a monoplane. If the gap of a biplane is made infinite then each wing

will carry 1/2 the load of the monoplane wing and the trailing vortex will be 1/4 as strong as the monoplane. This means that at infinite gap, the biplane has 1/2 the induced drag of a monoplane. A boxplane is advantageous over a biplane because the end plates affect the strength of the trailing vortex such that it is more efficient than a biplane at smaller gap to span ratios. An effective way of comparing the efficiency biplane and the boxplane to the monoplane is by saying that the gap effectively increases the aspect ratio. Figure 4.1 by Hoerner shows the increased aspect ratio as a function of gap/span ratio and shows the increased efficiency of the boxplane[4].

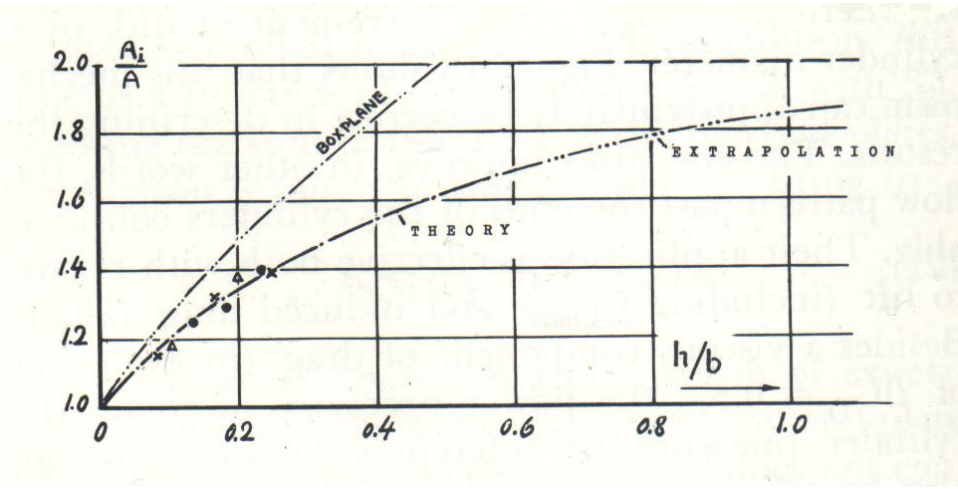

Figure 4.1. Effective Aspect Ratio vs. Gap[4]

The induced drag of a monoplane is given by Eq. (4.1).

$$C_{di} = \frac{C_l^2}{\pi ARe} \tag{4.1}$$

Assuming a realistic value of $e = 0.93$, a quick calculation of the induced drag of the monoplane for the drag analysis was obtained. NACA Report 151 focuses on non-planar lifting surfaces and relates the induced drag of a non-planar wing to a monoplane with Eq. (4.2)[5].

$$C_{di_2} = C_{di_1} - C_l^2/\pi(S_1/b_1^2k_1^2 - S_2/b_2^2k_2^2) \tag{4.2}$$

In Eq. (4.2) the value of $k = A_i/A$ is related to the gap to span ratio by Fig. 4.1[4]. From these relations the induced drag for each of the four final concepts was calculated and tabulated.

Another source of drag is friction and form drag. The airflow over the wing, tails, and struts is assumed to be laminar and so[6]:

$$C_f = 1.328/\sqrt{Re} \tag{4.3}$$

Due to the low Reynolds numbers that this aircraft will be operating at (about 400,000), the

assumption of laminar flow is reasonable and only a small portion the wing will experience turbulent flow. The chord of the tails changes slightly according to the area calculated from the tail volume coefficients and the $AR = 7$ assumption and using the form factors found in Hoerner,

$$FF = 1 + 1.2(t/c) + 70(t/c)^4 \tag{4.4}$$

the drag for the tails of each concept is easily calculated. This form factor was also applied to the endplates for the boxplane concept. However, because the struts have a thickness of 20% which is outside the validity range of the form factors used for the wing and tails, a different form factor is used. (Eq. (4.5))

$$FF = 2(c/t)^{0.75} + 2(t/c)^{0.25} + 120(t/c)^{3.25} \tag{4.5}$$

Interference drag is a result of the boundary layer interactions at the junctions of two different components. This drag is a function of both thickness and chord:

$$C_{d_{int}} = 0.8(t/c)^3 - 0.003 \tag{4.6}$$

The interference at the wing-fuse and strut-wing joint was calculated and tabulated. The interference between the tail surfaces and the mounting pylons is neglected as it will remain constant between the concepts and with the use of thin pylons, $t/c \approx 2\%$, this drag can be considered negligible.

Table 4.1 shows the complete tabulation of the preliminary drag calculations. Here it can be seen that classic monoplane configuration is competitive against the biplanes and is ranked second according to total drag. The 60 ft biplane has considerably lower induced drag and wing interference drag than the monoplane. However, due to the smaller wing chord the tail geometry must be modified thus producing higher the drag on the tail compared to the monoplane. Increased tail drag is also present in the boxplane but the increased efficiency of the wing offsets this and the overall drag is lower. The boxplane concept was chosen to be the final concept because of the lower drag.

Table 4.1. Drag-Estimate of Preliminary Design Concepts

Design	Monoplane	45ft Biplane	60ft Biplane	**Boxplane**
Drag, [lb]	4.7	5.8	4.5	**4.2**

4.2 Airfoil Selection

The wing will be operating at an Re of 400,000 as opposed to typical Re in the millions which increases complexity of airfoil selection. Because HPAs operate at extremely low Reynolds number the drag is dominated largely by the control of the separation bubble. If the separation bubble

becomes large then the pressure distribution around the bubble will have a component against the direction of flight and cause pressure drag. Because the air within the separation must be mixed into the boundary layer, a large bubble will require a large amount of air to be mixed with large losses in momentum resulting in high drag. To reduce the possibility of an excessive bubble or complete separation, transition from laminar to turbulent flow must occur. The most efficient place for transition to occur for low drag is within the separation bubble itself. The location within the separation bubble that transition occurs requires attention as well. If transition occurs too early then there will be a penalty due to increased turbulent flow. If transition occurs too late then the bubble will grow in size and the pressure and mixing losses previously mentioned will result. The separation bubble must also be located as far aft on the airfoil as possible. There is a limit to this because as the airfoil geometry is changed to move the bubble aft, it creates conditions that will allow the bubble to rapidly move forward or the flow to completely separate at off design conditions. This would result in loss of lift and have drastic consequences on the flight[7].

Due to the stringent requirements of HPA airfoils it is impractical to try to design an airfoil without significant prior knowledge and experience in airfoil design. Researching the airfoils previously used yielded three candidates - NACA 4412, FX76MP, DAE 11 - 31.

The NACA 4412 has been used on several HPAs including the 11th JIBR Championship[1]. While it has proven successful at JIBR, it has the highest drag of the three candidates. The Wortmann FX76MP has been utilized many times and this airfoil was designed by Wortmann specifically for HPA use[8]. The location of the separation bubble has been addressed by Wortmann but at the time this airfoil was developed the aerodynamic community lacked the high power CFD tools that are available to current aerodynamicists. The DAE series were developed by Drela to address the issue of transition. This series has the lowest drag of any of the candidates[7].

In addition, the DAE series has a lower pitching moment that will allow a lower structure weight. The combined lowest C_d and C_m in conjunction with favorable boundary layer behavior at off design conditions results in the DAE series being the final airfoil selection for the Iron Butterfly. This series is comprised of DAE 11, DAE 21, and DAE 31 which have been separately optimized for a specific C_l so that they may be used to obtain the desired span wise lift distribution.

4.3 Wing Area Constraint Analysis

The preliminary selection of wing area was achieved by defining a series of wing constraints in terms of lift coefficient, C_l. A design space was plotted with the defined constraints and wing area chose from within the space. The design space for wing area may be seen in Fig. 4.2.

The first and most obvious constraint is stall, C_{lmax}. Estimates for C_{lmax} were determined from XFOIL[2]. XFOIL is an airfoil analysis program, predicts a 2D $C_{lmax} = 1.58$ and due to 3D

[1] Japan International Birdman Rally

[2] XFOIL is released under GNU General Public License[9]

effects of the airflow the 3D C_{lmax} is set at 1.5. This sets a constraint for minimum wing area of 110 ft^2. Further, a stall margin of 15% C_{lmax} was set for both straight and level flight and turning flight. The next constraint is the C_l that corresponds to the drag bucket limit, where drag becomes excessive if C_l is reduced further. This drag bucket limit imposes a maximum area of 210 ft^2. The final constraint is that the tail chord must be equal or greater than 1 ft. This is merely a structural and ease of building constraint that constrains the wing area through the tail volume coefficients. The maximum lift to drag ratio, L/D_{max} represents a wing area that will result in the best L/D at cruise conditions. Each constraint is indicated in Fig. 4.2 and also on the drag polar in Fig. 4.3.

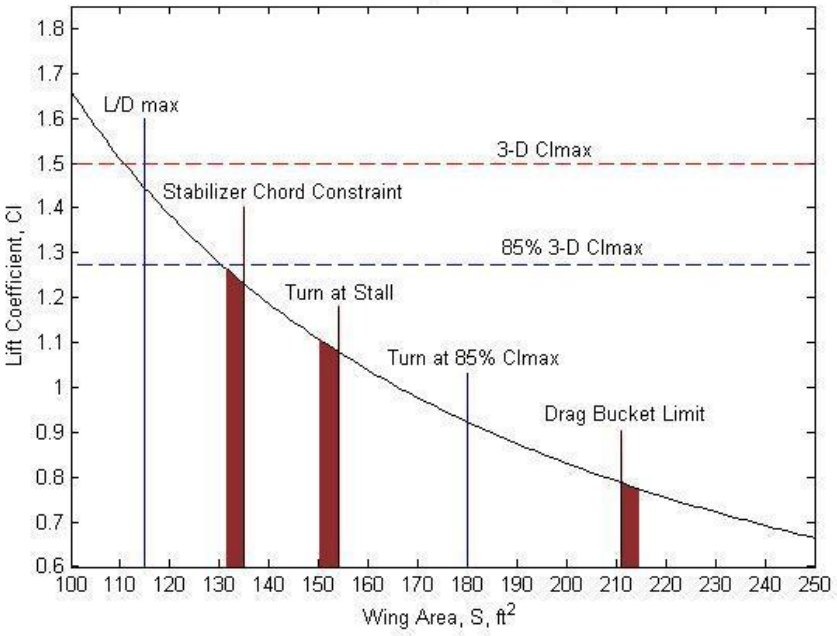

Figure 4.2. Compilation of constraints on wing area

Figure 4.2 indicates that flying at L/D_{max} is not feasible and any area greater than 114 ft^2 will have higher drag. The stabilizer chord constraint is lower than the turn at stall constraint and the required area to fly in a turn at a 15% C_{lmax} stall margin lies in considerably before the drag bucket limit. The lower the wing area the lower the drag. Therefore the stall margin in the turn becomes the lower limit on wing area. The wing area was set at 180 ft^2.

4.4 Friction-F Agreement

To validate the previous drag calculations, a model of the final design was created and analyzed with the program Friction-F. Friction-F will take inputs of length, area, Re, thickness, and percent laminar flow from which it will output a total profile drag coefficient C_{d_0} for the entire aircraft

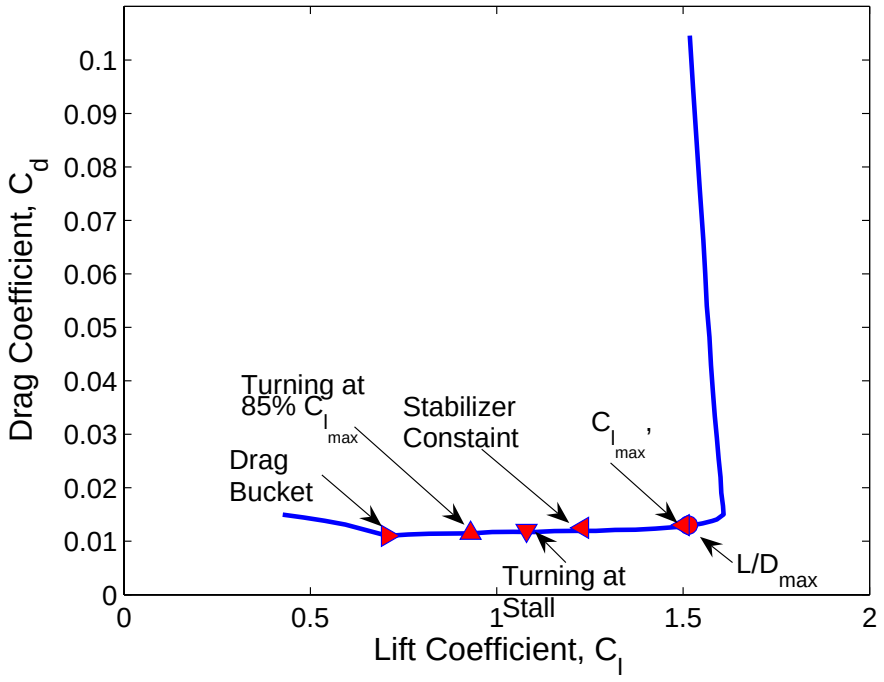

Figure 4.3. Compilation of constraints on wing area indicated on Drag Polar

configuration by calculating skin friction C_F, and the form factor FF, of each component and performing a summation. The model included wings, tails, and struts and comparing the results from Friction-F to the previous results calculated from the Hoerner's drag equations in Section 4.1, a large difference was noticed. This large difference lead to the investigation and validation of both drag analysis's.

Initially the values of C_F were in disagreement, though both analysis's assumed pure laminar flow. The Friction-F code was reviewed and the methodology for C_F compared to the previous drag analysis and it was determined that they were indeed similar and should produce the same results. After much work it was determined that the error was in the Friction-F model resulting in the calculation of C_F for a much greater Re. Once the values for C_F converged, a difference still remained, see Table 4.2.

Table 4.2. Friction-F and Hoerner Drag Analysis Agreement

	C_{dF}	C_{dForm}	C_{d_0}	Drag
Hoerner	0.00603	0.00145	0.00748	2.081
Friction-F	0.00603	0.00140	0.00743	2.068

Here it can be seen that the difference lies in the form factors used to determine drag due to thickness. Drag due to thickness is not a phenomenon that can be derived mathematically

such as friction or induced drag. Due to this, there are several different methods for calculating form factors. Friction-F uses the methodology developed at Northrop Grumman and by looking at Fig. 4.4 it can be seen that these are the most optimistic of the different form factors.

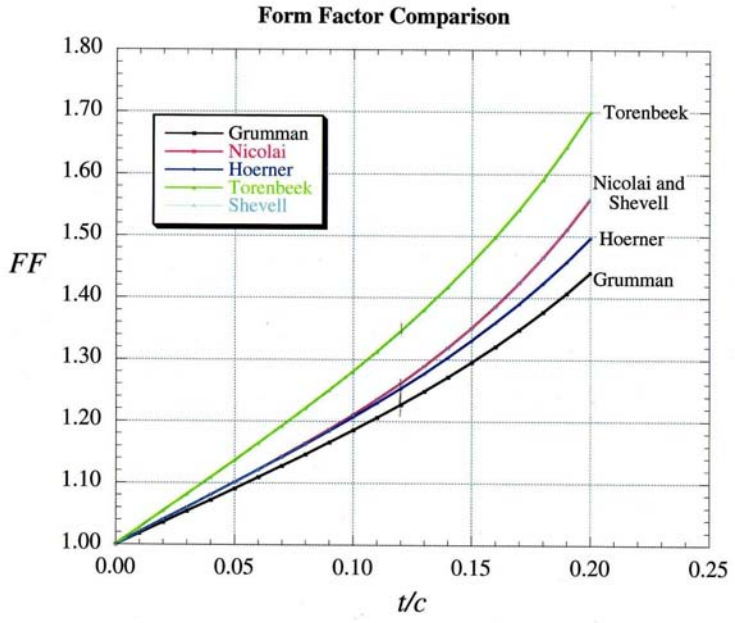

Figure 4.4. Comparisons of form factors developed independently.[10]

Exploring the FF values for individual components it was discovered that the greatest difference lies at high t/c values, great than $t/c = 15\%$, such that the struts had a difference of 3. However, due to the low speeds of HPAs this results in a 0.013 lb difference between designs.

In an effort to minimize the possibility of designing an aircraft with greater drag than the thrust available, the Hoerner form factors were used for final drag analysis though Friction-F remains a useful tool in calculating C_F for flows that both laminar and turbulent.

4.5 Wing Development

The full scale wing twist distribution presented a number of analytical problems. I-Drag[3] is incapable of handling a full geometric model of the wing and therefore is incapable of providing an ideal lift distribution to work to match. To obtain this ideal lift distribution, correlating to minimum drag, AVL[4] was used in an iterative manner to obtain an even downwash angle across the wing. The full scale wing is comprised of a blending of two airfoils, the DAE 11 and the DAE 21. The DAE 21 was designed to provide a lower C_{l_α} than the DAE 11 and was used over the last ten

[3]I-Drag is released as freeware[11]
[4]AVL is released under GNU General Public License[12]

feet of the wing where the local lift coefficient drops. To define twist distribution the wing was decomposed into nine stations. The twist at each station was adjusted until an even downwash was obtained and changes in efficiency per iteration were smaller than 0.5%. The final twist distribution has been tabulated, Table 4.3.

Table 4.3. Tabulated Twist Distribution

Span Location, [ft]	0	2	4	12	20	27.6	28.6	29.5
Top [deg]	1.5	1.5	1.7	1	-0.5	-2.7	-4	-4.6
Bottom [deg]	0	0	1.6	1	-0.5	-2.7	-4	-4.6

The endplates on a boxplane represented a unique design challenge in that their efficiency is highly dependent on their lift distribution. Because I-Drag is incapable of handling a complete geometric model of the airplane including the polyhedral, several simpler models were run and analyzed to identify any trends. These models consisted of straight top and bottom wings that remain parallel and have simple dihedral with angles of 0, 5, 11, and 15 deg. It was seen that increasing dihedral angle only causes the distribution to translate and carry greater loads. However, increasing the dihedral angle had the effect of increasing the loading on the top wing and decreasing the loading on the bottom such that at 15 deg the top wing is carrying almost twice the load of that on the bottom wing. Since this is know to not be the case due to the previous AVL model, the translation effect was considered to be due to complications or errors within the I-Drag program. At 0 deg dihedral the top and bottom wing are loaded equally and the endplate load distribution was used.

Like the wing airfoil, the endplates operate at very low Re and so the low Re airfoil list generated for the main wing from the UIUC LSAT's was reviewed. Due to the low $C_{l_{req}}$ and the symmetric positive to negative loading, only symmetrical airfoils were considered. Due to time constraints the endplates were designed to utilize the NACA 0012. A initial twisting of the endplates, Table 4.4, resulted in an increase in efficiency and reduced the downwash angle at the tips. The final lift distribution and resulting downwash can be seen in the AVL Trefftz Plane plot, Figure 4.5.

Table 4.4. Tabulated Endplate Twist Distribution

Vertical Location, [ft]	-2.5	0	2.5
Twist [deg]	3	0	-3

It can be seen that this wing twist and endplate design results in a very efficient airplane with an induced drag coefficient of 0.011 and a corresponding efficiency of 1.18. With the performance considerations previously discussed this will yield a total target L/D of 20.

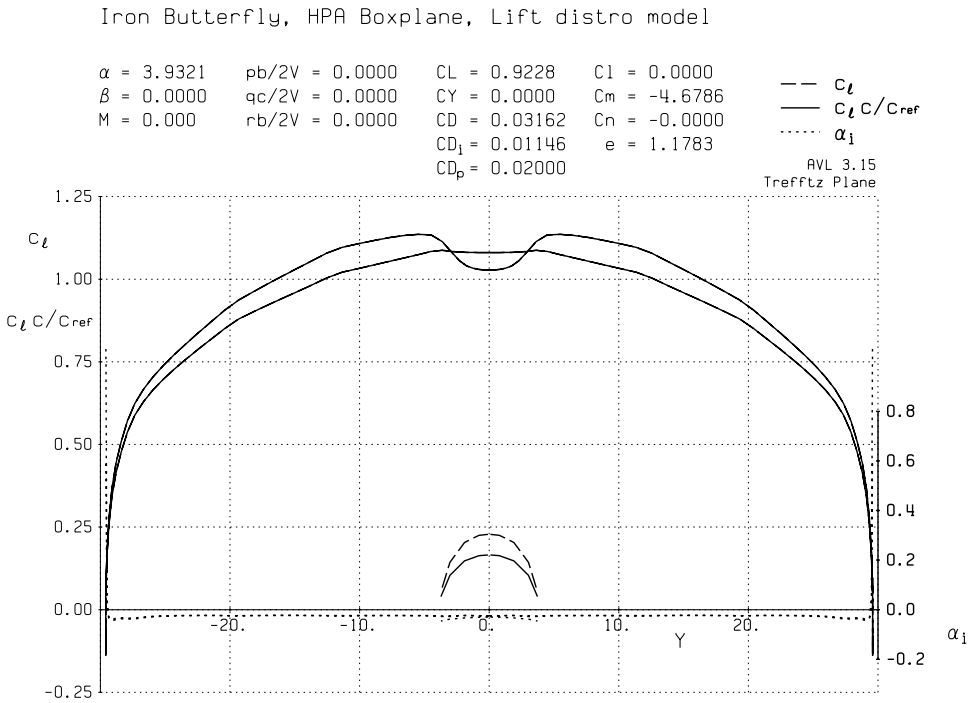

Figure 4.5. AVL Trefftz Plane Plot

4.6 Vertical Tail Planform

A gap of 5 ft and an allowance of 10 deg of rotation at take off required that the tail only extend down 2.14 feet below the tail boom. To maintain efficiency the tail becomes asymmetric about the tail boom so that the lower surface has a low AR and the top surface has a high AR. This asymmetry then requires a definition of the area and loading on each surface. However, when the fin is deflected to produce a moment for a right turn, it produces a rolling moment to the left due to the asymmetry. In addition, the loading of each surface greatly affects the net efficiency of the vertical tail and the more load carried on the bottom surface the greater the induced drag during turning. To further complicate the issue, the greater the rolling moment produced the stronger and heavier the tail boom must be made, which degrades overall flight performance. In addition the rolling moment affects the stability and control of the aircraft. Due to the complexity of this optimization problem and the limited time available, the net tail load was divided evenly between the upper and lower surface with the lower surface comprising 1/4 of the total area required to obtain the desired tail volume coefficient. From this, root and tip chords were adjusted to obtain a tail with an overall AR of 5.6. The tail shape may be seen in the drawing packages in the appendix. This tail produces a rolling moment of 7.8 lbs in a turn and currently appears structurally reasonable. However, future development of the aircraft should include a reassessment of this problem with an optimization including input from structures and stability to obtain the most efficient vertical tail.

5. Structures

At the conclusion of the conceptual design phase, the structural comparisons between a biplane configuration and a monoplane configuration were left to be further quantified. Power required for an aircraft varies with the weight to the 3/2 power whereas it varies linearly with drag[13]. Thus, significant emphasis was placed on producing a lightweight structure, specifically for the spar design. Once the basic configuration was chosen, focus could shift to the development of secondary structures.

5.1 Conceptual Model Testing

Initial attempts to quantify differences between a monoplane and a biplane proved computationally intensive. Instead, models were built of several configurations and compared against one another. Three biplane models were built, two with single struts on each wing and one with two struts on each wing. A cantilevered monoplane structure was also built. The aerodynamic drag from flying wires at the speeds necessary to win the Kremer Sport Prize made them ineffective so they were not used during testing.

All four models used the same amount of load carrying material in their spars. The biplanes

used 1/16 in x 1/8 in basswood whereas the monoplane used 1/8 in square stock. Struts were not accounted for in overall aircraft weight and were made stiff enough to support the assumption of them remaining rigid throughout testing. Rough scaling was employed off the best estimate of aircraft configuration at the time of testing. The models were restrained in a loading fixture and simply supported at the tips. Weights were hung from the center structure. A picture of one of the deformed structures can be found in Fig. 5.1.

Figure 5.1. Deformed basswood biplane model during testing

A plot of measured displacements for applied loads can be found in Fig. 5.2. Model testing showed significant stiffness improvements over the monoplane structure with the biplane configurations. Both biplanes with single struts per wing exhibited similar stiffnesses, implying that number of struts was more important than location. The biplane with two struts per wing was also significantly stiffer than those with single struts. Based on the results of the basswood model testing, the biplane configuration was chosen for further investigation.

5.2 Analytical Solution to the Biplane Structure

Upon selection of the biplane aircraft configuration, it was necessary to quantify displacements and stresses in the structure to adequately size spar shapes and components. The frame structural model, shown in Fig. 5.3, was defined encompassing all relevant aircraft configurations. It was assumed that the struts were rigid and that the beams all had equal cross-sections and material properties for initial analysis.

The problem defined above proved to be statically indeterminate and could not be solved directly. Instead, an implicit solution proved necessary using structural displacements. The six spar sections of the frame were modeled as beams allowing extension and bending. Shear was ignored. A set of two differential equations governed the displacement of the beams in this case, Eq. (5.1) for extension and Eq. (5.2) for bending. P_x is defined to be the distributed loading in the vertical direction along the beams[14]. EI_{yy} are beam cross-sectional properties, its flexural stiffness.

$$\frac{d^2 w_i}{dz^2} = 0 \tag{5.1}$$

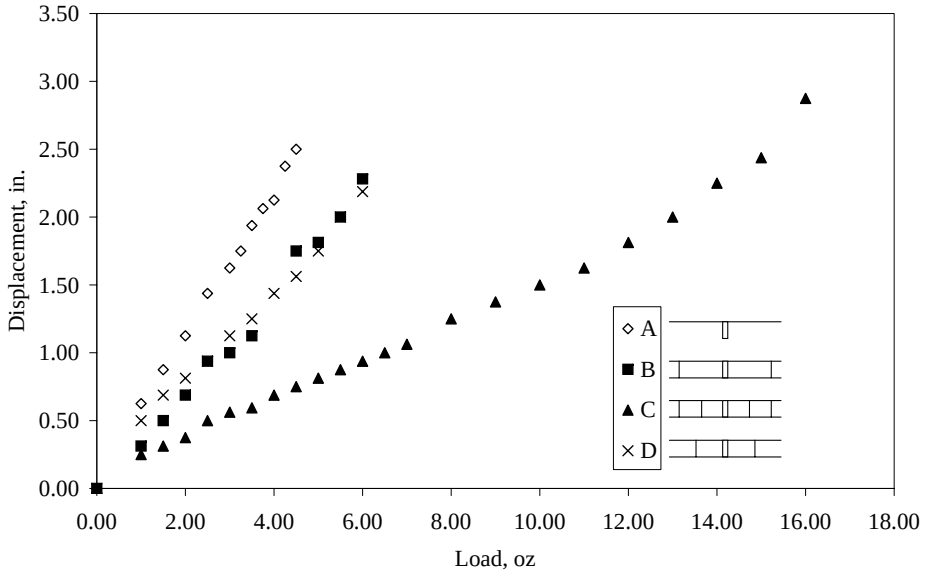

Figure 5.2. Measured displacements for basswood spar models

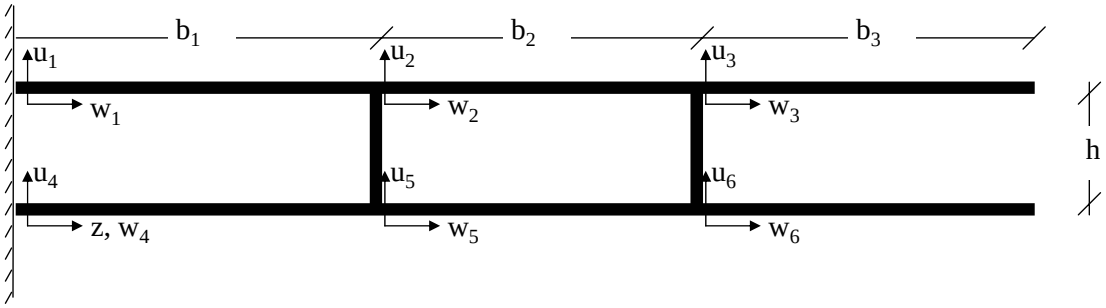

Figure 5.3. Definition of biplane structural components for analytical solution

$$\frac{d^4 u_i}{dz^4} = \frac{P_x}{EI_{yy}} \tag{5.2}$$

The problem was solved in terms of the variables b_1, b_2, b_3, h, EI and EA, the beam's extensional stiffness. From there, determination of the displacement and stress distribution for a specific design case was trivial. Additional assumptions included that of a linearly elastic structure with isotropic properties. All beams were composed of the same constant cross-section.

This problem definition provided a system of 36 coupled differential equations with the necessary 36 boundary conditions. Six came from setting the displacement and slope to zero at the root. Twelve came from displacement and slope continuity at the joints. Six from the free end conditions at the tips of beams 3 and 6. The last twelve came from displacement, slope, force, and moment relations across the struts.

MATLAB®[5] was used to solve the system of equations symbolically. Solutions were initially validated by examining the physical correctness of the solution. In other words, for a positive lift configuration did the structure deflect upward? Displacement shapes were compared qualitatively and quantitatively with the basswood models using material properties derived from the cantilevered monoplane case and will be discussed in detail in a later section.

Shear force and bending moment relations for the basswood biplane spar model with two struts per wing for two different loading configurations were developed to explain the non-intuitive displaced shapes observed. Figure 5.4 shows the solution corresponding to a total loading of 7 oz distributed as 4 discrete point loads of 7/4 oz on each wingtip, a specific case tested during the initial investigation. Figure 5.5 shows the solution corresponding to a lift of 7 oz evenly and constantly distributed over each wing.

Local bending moment in the top and bottom spar ranged from negative to positive values, jumping at the location of each strut. This variation leads to the development of the non-intuitively "s" shaped displaced structures. Tensile forces in the lower spar and compressive forces in the upper spar also jumped in value at each strut. These jumps are caused by the transfer of loads between spars due to the rotation of the struts. Examination of the results showed that the sum of the couple generated by the normal forces in the beams and the local bending moments in each individual spar was equal to the bending moment at that point for a similarly loaded cantilevered beam, a necessary condition for equilibrium.

This analysis was not, however, without its drawbacks. Only relatively simple loading situations could be defined mathematically and thus, actual elliptic or asymmetric loading configurations would prove challenging. The struts were assumed to be rigid, although when actually built they would not fully exhibit this property. Adding to the analysis to better model the physical problem proved tedious and time-consuming. Due to these constraints and the intense time line set for design, a more rigorous and expeditious tool was sought.

[5]MATLAB® is a registered trademark of The MathWorks Inc.

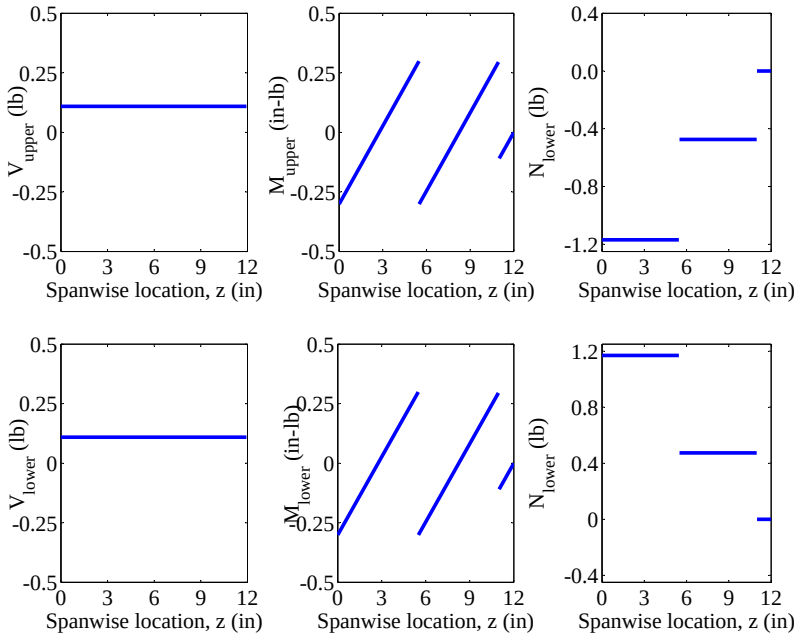

Figure 5.4. Shear force, bending moment, and normal force in 2 strut basswood biplane model with 7 oz lift distributed as tip loads.

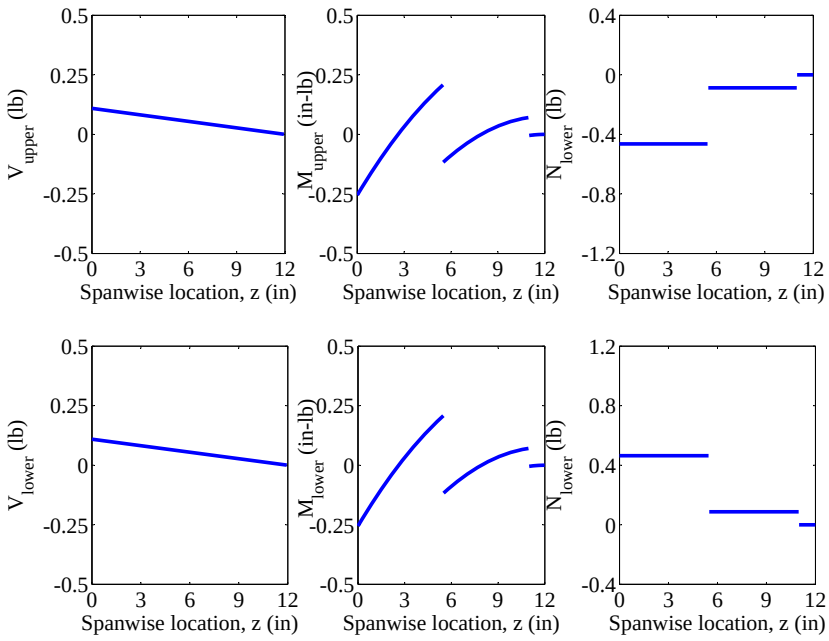

Figure 5.5. Shear force, bending moment, and normal force in 3 strut basswood biplane model with 7 oz lift evenly distributed spanwise.

5.3 ANSYS® Finite Element Models

During the development of the analytical MATLAB® model, ANSYS®[6] FEM software, version 8.0, was made available to the design team. Some experimentation showed that numeric results equal to and surpassing the analytical model could be obtained. The structure was again modeled with linear elastic, isotropic beam elements. Extension, bending, and shear deformations were now included. Each beam from the analytical solution was now broken down into as many as 8 elements. Cross sectional properties and loading could be defined for each element. Thus, using this model tapered spars and more complicated loading configurations were now easily analyzed. However, shear force, bending moment, and normal force diagrams equivalent to Figs. 5.4 and 5.5 are not easily developed, although the capability does exist.

Again, validation was achieved by qualitatively and quantitatively comparing the results of the model against the already-tested basswood biplane spar models. Stresses in the elements could be computed. Nodal displacements were also given in the solution. Comparisons were made only against measured displacements. Shear deflection accounted for less than 0.1% of model displacement, supporting the earlier assumption that shear deformations were negligible. Upon sufficient validation of the modeling technique, ANSYS® was selected as the primary tool for sizing spar components both for the remote control model and the final aircraft.

5.4 Validation of Analysis

Comparisons were made between the basswood biplane spar models tested in early stages of development, the analytical model, and ANSYS® finite element models. Figure 5.6 shows this comparison for the model closest to the actual aircraft geometry, one with two struts per wing. In this case, the load P is equivalent to the lift described earlier. Non-linearities were not accounted for in either the finite element or analytically modeled structure, as exhibited by the straight line curve fits to these solutions. The analytical model slightly over-predicted structural stiffness because the struts were forced to remain rigid. This assumption allowed more of the overall bending moment in the structure to be carried as compressive or tensile forces. Despite the rather weak assumption of modeling the basswood as a linearly, isotropic material, a good fit between the ANSYS® model and the tested basswood models exists.

5.5 Strut Number Analysis

The tradeoff between structural weight and associated drag required a quantitative analysis to determine the best number of struts. For a given amount of spar material, adding struts makes the wing stiffer. Thus, the structural weight of the spars can be reduced by adding struts to achieve the same overall structural stiffness. The finite weight associated with each added strut partially

[6] ANSYS is registered trademark of ANSYS Inc.

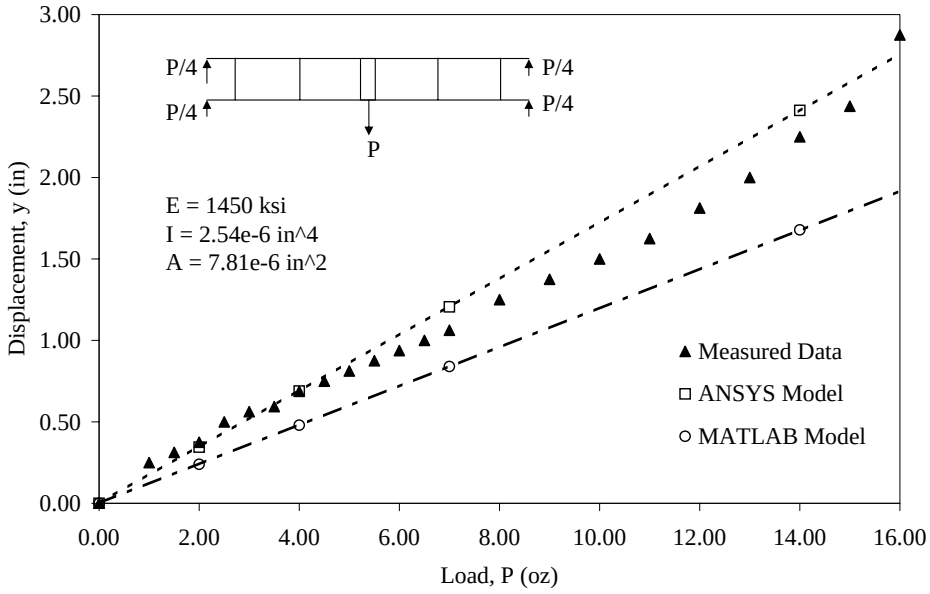

Figure 5.6. Comparison of analytical and ANSYS® finite element models with data

offsets the reduction in spar weight. Even so, any appreciable number of struts per wing added would reduce the overall structural weight.

To quantify the problem and determine the final number of struts to use, several assumptions had to be made. The spar weight was assumed linear with its moment of inertia. Thus, spar weight decrease was directly proportional to a reduction in wing stiffness. Physically this would be equivalent to a case where spar caps are reduced in width to reduce structural stiffness while their height and separation remain unchanged. Added strut weight was assumed proportional to the new spar weight so the strut weight was not a constant value. Thus, the bending rigidity of the struts was kept in line with that of the spars and simple finite element modeling was achievable. Original spar weight was determined as a fraction of the aircraft gross take off weight. Exact values of this ratio were not known, but analysis was completed for the range of 2.5% to 10%.

The analytical process used the unmodified boxplane as the baseline aircraft to which comparisons were made. A number of struts were added to each wing, evenly distributed across the span and the associated reduction in required spar stiffness to maintain reasonable tip displacements was calculated using ANSYS® models. This reduction in stiffness led to an associated reduction in aircraft gross takeoff weight. Each new weight was used to calculate a drag for each strut configuration. As long as drag was reduced, the addition of the strut proved beneficial. Analysis was repeated for several spar weight fractions in the assumed range.

The drag change associated with additional struts comes in two forms. The first is reduced induced drag. By reducing the gross weight of the aircraft, the lift generated is reduced, weakening

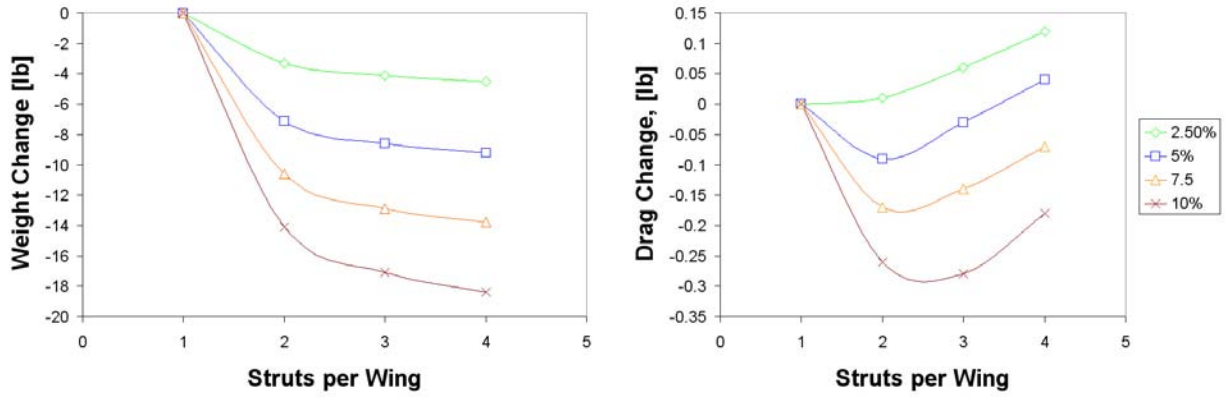

(a) Weight v. Struts.

(b) Drag v. Struts.

Figure 5.7. Strut, spar weight, and drag optimization

the trailing vortices and lowering induced drag. The second drag change is parasitic drag due to friction and interference. Each additional strut adds wetted area and two additional junctions where interference drag is present. These two effects increase drag, thus a balance between increased parasitic drag and reduced induced drag must be established. To obtain accurate changes in induced drag I-Drag was utilized. C_{di} values for each strut configuration and the reduction of induced drag was quantified by changing the I-Drag model to reflect changes in C_L. Increased parasitic drag was calculated using Hoerner form factors and under the assumption that 80% of the flow over the strut was laminar. Values of C_F for this mixed flow were obtained from the program Friction-F. Then by calculating the additional interference drag, the total change in parasitic drag per strut could be calculated. Thus, the total change in drag for each strut configuration was found, and can be seen in Fig. 5.7 At the low end of the spar weight fraction, near 2.5%, one or two struts proved most beneficial. At the high end of the range, near 10%, two or three struts proved most beneficial. Thus, a configuration with two struts per wing was chosen for further investigation. All further calculations will be performed on the two strut configuration.

5.6 Gap

Several studies were made to understand the influence of the gap between the two wings on aircraft performance. Considerations included structural weight, total drag which translates to power required, minimum fuselage height and propeller efficiency. Additionally, the aircraft must fit in the trailer and be relatively easy to work on while assembled. It was assumed that structural weight increased with moment of inertia, spars were untapered and loading was constant along the span for initial studies. 2D ANSYS® finite element models with beam elements were used for all structural bending analysis. Although tapered spars and elliptic loading would be designed for

eventually, each test case required construction of a separate model and a considerable amount of time. These simpler cases would still show the same trends.

Initially, two extreme cases were examined to further understand how the structure deforms, shown in Fig. 5.8. First, when spar stiffness is much higher than strut stiffness, case a, only minimal stiffening is achieved from the struts, they simply deform until each spar carries the majority of the load. Bending moments are carried mainly in each local spar rather than as tension in the bottom and compression in the top. Displacement is governed by each individual spar stiffness and the displacement curve looks similar to that for a single cantilevered beam. For this case, the stiffening desired from having two wings separated by struts is not achieved.

For case b, when strut stiffness is much higher than spar stiffness, a somewhat non-intuitive "s" displacement is exhibited, much like the conceptual model testing discussed earlier. In this case the struts do not deform, but simply rotate. Bending moments are carried as both local bending moment in each spar along with tension in the bottom spar and compression in the top. As in the discussion of the initial conceptual model testing, the variation between position and negative bending moments between the struts is the main cause for the oddly shaped displacement curve. Stiffening by separating the wings is achieved, however, only to a point. A gap is reached at which further increase no longer increases the overall structural stiffness.

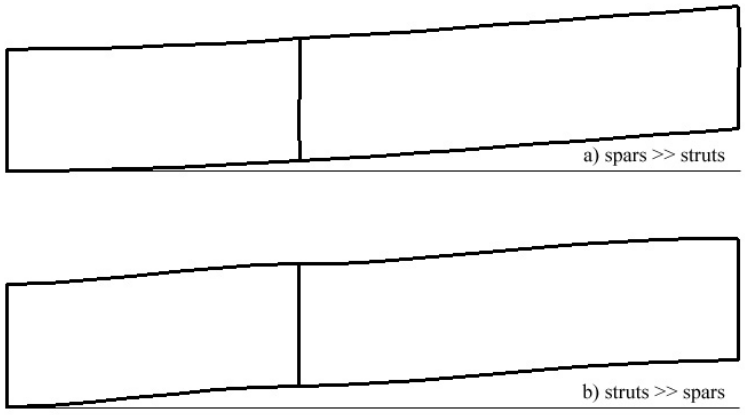

Figure 5.8. Bending for various spar to strut stiffness ratios.

For the final aircraft, however, the strut stiffness and spar stiffness will be on the same order of magnitude. Thus, one final assumption was made in analyzing component weight as a function of gap. The spar and strut stiffness were assumed equal. Models were analyzed with a 1G elliptic load for cruise. Aluminum tubes with outer diameters of 2 in were used for structural members. For each gap, wall thickness was varied to achieve the desired stiffness resulting in a 40 in deflection at the tip, a large but allowable value providing much of the desired dihedral in flight. Knowing the necessary wall thickness, the total weight of struts and spars for each gap could be calculated.

Figure 5.9 shows spar weights as a function of gap. When spar and strut stiffnesses are on the same order of magnitude, significant stiffening is not achieved and structural weight actually increases with gap. Scatter shown in the figure is the result of discretizing the load and sizing the spars to achieve tip displacements less than 40 in but not exactly 40 in. Thus, a curve was fit to the weight versus gap data and used as a better representation of how spar weight varies with gap. This equation is shown on the figure.

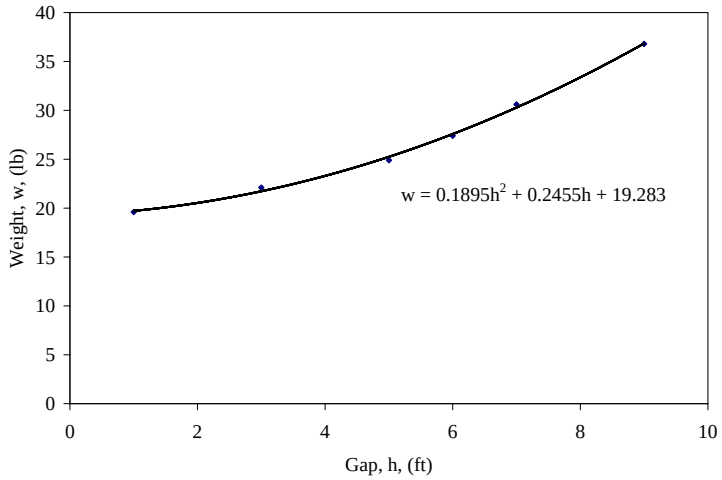

Figure 5.9. Spar weight as a function of gap.

Once structural weight was known as a function of gap, the weight of all other components and pilot were given a constant value of 200 lb for drag analysis. The drag of the wing consists of two main components, induced and friction. The friction drag increases with gap. This was calculated using the Hoerner form factors and with a t/c of 12%. The flow was assumed to be 75% laminar yielding a C_f of 0.00363. Under these assumptions, the friction drag was easily quantified.

Increasing the gap increases the efficiency of the wing and therefore reduces C_{d_i}. However, increasing the gap also requires a heavier spar structure and increases C_{d_i}. To quantify this problem a simple I-Drag model was constructed consisting of straight parallel wings with 11 deg. of dihedral in the center. From this the gap could easily be adjusted accordingly and a quick calculation yielded the corresponding $C_{l_r eq}$ for each case. The C_{d_i} yielded from I-Drag was then used to calculated the total induced drag of that configuration.

The results of each case were tabulated and graphed, Fig. 5.10. Here it can be seen that there is a clear minimum at a gap of 5 ft although that minimum is incredibly shallow. This is 6 in

greater than the minimum gap required for pilot placement and is also small enough to allow easy access to both wings from the ground once assembled. The difference between the worst case and best case is only 3.5% but still large enough to make a measurable difference. It is through this structural and aerodynamic analysis that the final gap of 5 ft was chosen as the final gap.

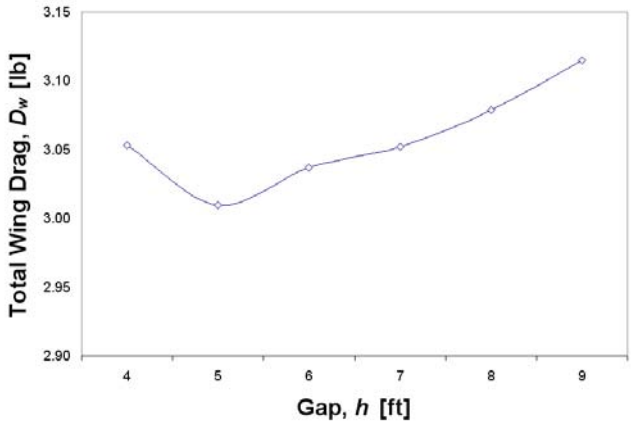

Figure 5.10. Total Wing Drag vs. Gap.

It is worth noting that many simplifying assumptions were made in the analysis of how gap affected aircraft performance. It is suggested that future work study the influence of the ratio of strut stiffness to spar stiffness while including elliptic loading in the analysis earlier. The problem seems to be highly sensitive as a whole and is worth additional investigation. It seems likely that a lighter configuration could be achieved, although the current one will work.

5.7 Constraints for Detailed Structural Analysis

To conduct detailed structural analysis for both the model and the full scale aircraft, several additional constraints were placed on the structure. Wing gap was defined as described above as 60 in. Final deformed shape at cruise was specified from control and stability analysis as a dihedral necessary to turn, discussed in Section 6.3 to be 11 deg of effective dihedral. This deformed shape at cruise was achieved with a combination of built in geometry and structural deformations in flight. Unlike most aircraft, HPAs deform significantly in flight and rigid structures cannot be assumed. However, by allowing the structure to deform significantly, lighter construction can be achieved. Deformation due to wing weight was not accounted for in final deformations.

Instead of the simple dihedral specified, a more efficient and realistic polyhedral was designed for as the structure would bend everywhere along the span, not just at the root. Each wing section was kept to 8 ft in length for the full scale aircraft as most tubes are available with this as a maximum length. To achieve a 60 ft span, the outboard panels were allowed to reach 10 ft in

length since loading was significantly less there. Thus, a small 2 ft section could be spliced on without the addition of significant weight. Limiting the full scale sections to 8 ft resulted in 24 in long sections for the R/C model. An excel spreadsheet written by Martin Brungard[15] was used to design a reasonable polyhedral with similar angles at each panel break that would provide the necessary 11 deg of effective polyhedral, shown in Fig. 5.11 for both the R/C model and the full scale aircraft. Y_{max}, was used as the design factor for initial strain based analysis at cruise in ANSYS®. Spars and struts were the only components modeled, stiffening by the skin and other components provided an additional safety factor. Validation of this structure would be done using stress analysis of the structure for more extreme loading situations. Effect of the components own weight was assumed negligible.

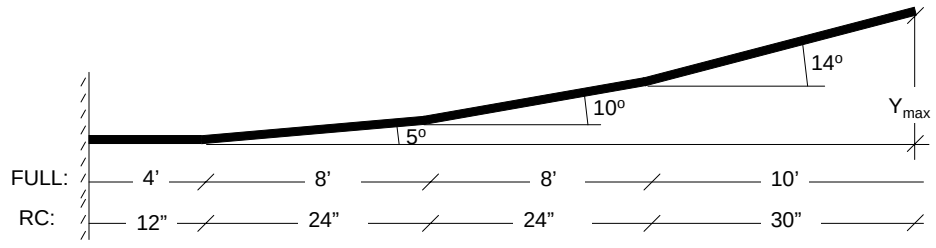

Figure 5.11. Desired polyhedral distribution for adequate turn initiation.

5.8 Material Selection and Structural Layout

Human powered aircraft employ major structural components in layouts very similar to many remote control models, specifically sailplanes. A main spar placed near the airfoil quarter-chord and point of maximum thickness with the possible addition of a trailing spar placed in the rear third of the wing will be used. To connect the two wings, a frame, similar to that on a bicycle will make up most of the fuselage and faired struts will be placed at semi-span and wingtip locations. A single tail boom will extend aft from the main fuselage to which simple, full-flying control surfaces will attach. Both these surfaces and the main wing will use ribs and a stressed skin design to attain the desired aerodynamic shapes. Hinges for the surfaces will utilize the spars themselves and provide relatively simple attachment points. Landing gear will be connected to the main fuselage structure along with the lower wing structure. Basic aircraft shape and these details can be seen in the drawing package in Appendix A2.

Although many human powered aircraft, especially high performance ones, employ composite spars because of their capability of attaining high strength to weight ratios, significant experience is necessary in designing such a spar. Without significant experience composite spars may actually end up being heavier than an associated aluminum spar. Many prototype aircraft have used thin-

walled aluminum tubing as spars to great success including Monarch and Chrysalis. Based on this information and the advice of Juan Cruz, the main structural designer of the Daedalus and many other human powered aircraft, aluminum spars were chosen instead of composite for the full scale aircraft spars. The considerable simplification of analysis by choosing an isotropic material was also considered in this decision. Foam ribs with cap strips of wood or composite tape will be utilized as secondary structure. Fairings around the fuselage will attain their shape utilizing balsa or basswood secondary structures covered in the same material as the wings and possibly using thin fiberglass fairings near the nose.

Final material selection for spars, struts, and the tailboom consisted of the various aluminum alloys. These alloys exhibit almost identical stiffnesses, densities and Poisson ratios. The main difference that sets them apart is their yield strength. Stress analysis, discussed below, showed that it was important to use the alloys with the highest yield strength available, the 7075 series. From Beer and Johnston, 7075-T6 aluminum has a modulus of elasticity of 10.4x106 psi, Poisson ratio of 0.3, yield strength of 73 ksi, and a density of 0.101 lb/in^3[16]. All final analysis assumed the material to be isotropic and in its linear elastic regime.

5.9 Skin Material

The skin used on the aircraft is an important choice, as it is a stressed skin and an essential structural part of the aircraft. Previous HPAs have almost exclusively used tensilized Mylar, which is essentially the material in a cassette tape. Tensilized Mylar, or "Tenzar" as it was called when first introduced in magnetic cassette tapes, is a fiber-reinforced bi-axially oriented polyester film with a heat seal layer, either ethylene vinyl acetate or ethylene vinyl acetate.

In the interest of improving on what has already been done, alternatives to tensilized Mylar were explored. The two most relevant parameters to consider were: tensile strength, and weight (or density). These were combined to create a term called, appropriately, specific tensile strength.

A few different skin materials were considered. Since many of the team members had previous experience with R/C skin materials, these were investigated and used to benchmark the other skin materials. Fig. 5.12 shows the dependence of the eventual total skin weight on the skin material used. Of particular note is the high weight of the older fabric coverings, which gave a skin weight of near 12 lbs[7].

The familiar R/C covering materials are in the middle of this region, such as Monokote, Econocote, Microlite, and similar. All of these materials are shown for the thickness in which they are available. Finally, the line of alphanumeric designators at the bottom of the plot is trade names for different varieties of tensilized Mylar in a thickness comparable to the R/C hobby coatings. Mylar is available in a wide variety of thicknesses. From this figure, it becomes obvious why previous

[7]The value plotted for fabric represents only the fabric itself and enough glue to adhere it. In reality, more glue would need to be added to smooth the surface, thus further increasing the weight.

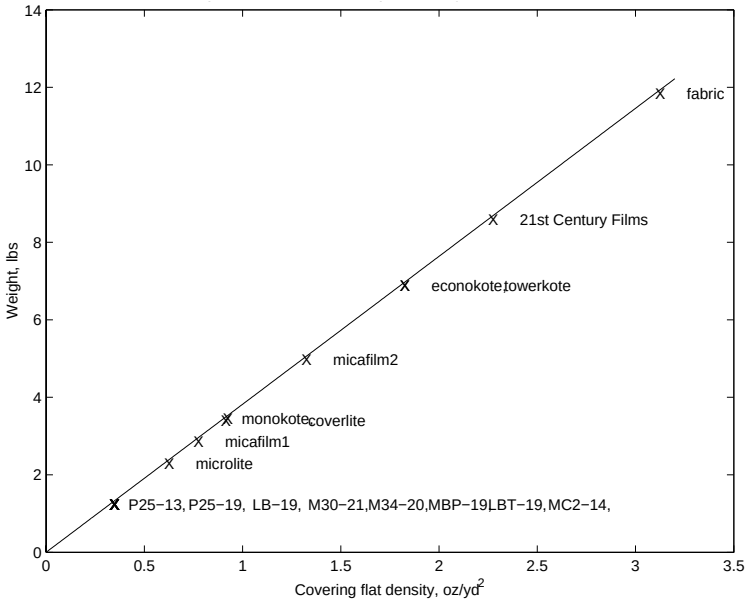

Figure 5.12. Skin weight as function of covering flat density, assumed S_{wet} = 550 ft^2.

HPAs have used tensilized Mylar as a covering material; there is the potential to reduce the skin weight to less than 2 lb, certainly a tremendous weight savings from the fabric covering discussed earlier. For these reasons, tensilized Mylar was selected for the final design.

5.10 Final Structure

Aluminum tubing is available in a variety of diameters and wall thicknesses. (See ref [17], [18], and [19]). Just like for the R/C model spars, only the finite thicknesses available were sized fo3 all components including wing and tail spars, struts and the tailboom.

With the exception of the main wing spar and strut system, all components could be sized analytically without the help of finite element software. Constant cross-section tubes were used in all cases. Both tail spars were sized by placing the entire load the surface was capable of generating at stall at the tip of the spar and calculating the root bending moment. Wall thicknesses were varied to provide a factor of safety of two from yielding. Tip displacements were then checked to be less than 10% of the span. For the elevator spar, an outside diameter of 1 in with 0.020 in thick walls should be used. A single cross section rudder spar would prove excessively heavy. Instead, a "step" taper as in the remote control model will provide a much lighter solution. These cross sections are detailed in the final drawings, but all use a wall thickness of 0.040 in.

Stress sizing of the tailboom provides a very light solution. However, upon investigation of its deflection and slope at the tip it was found that control reversal might occur under full load of the surfaces. Instead, the tailboom was sized with a constant cross-section for a slope of less than 5

deg at the tip under full rudder deflection, the larger of the two surfaces. This tailboom could be made significantly lighter with the use of a tapered boom, however to date no source was known to be available. A 3 in diameter was used to stiffen the boom without the addition of much weight or drag. It is also detailed in the final drawings with a wall thickness of 0.090 in.

A first cut at the spar and strut configuration using an evenly distributed 1G cruise load case with 2 in diameter tubes and 0.030 in thick walls displaced to the desired shape and weighed 32 lbs. However, further stress-based analysis must be used to ensure that the structure is not beyond it's linear elastic regime.

Initial attempts were made to expand the use of ANSYS® for stress analysis as well. However, specifying geometry directly in the program is difficult and tedious. The capability exists to import IGES files and define geometry in that manner. A parametric CAD model of the spar and strut structure in NX 3.0 was defined such that wall thicknesses, gap, and dihedral breaks could be easily updated and re-analyzed. ANSYS® had difficulty developing the geometry from the IGES files, however, mainly due to the large length and very small wall thicknesses.

The team had more experience with stress analysis using NX's in-house analyzer, Structures P.E. Initial meshes and stress distributions were attained using this avenue. A trial case was analyzed with a point-load of 108 lbs at the tip (1G tip load) evenly divided between the top and the bottom in an attempt to merely get some feel for how the stress was distributed throughout the structure. Figure 5.13 shows the overall displacement curve. Different colors denote different values of the octahedral stress. A more instructive view is shown in Fig. 5.14 whereby the stress is seen to be highest near the joint in the struts themselves.

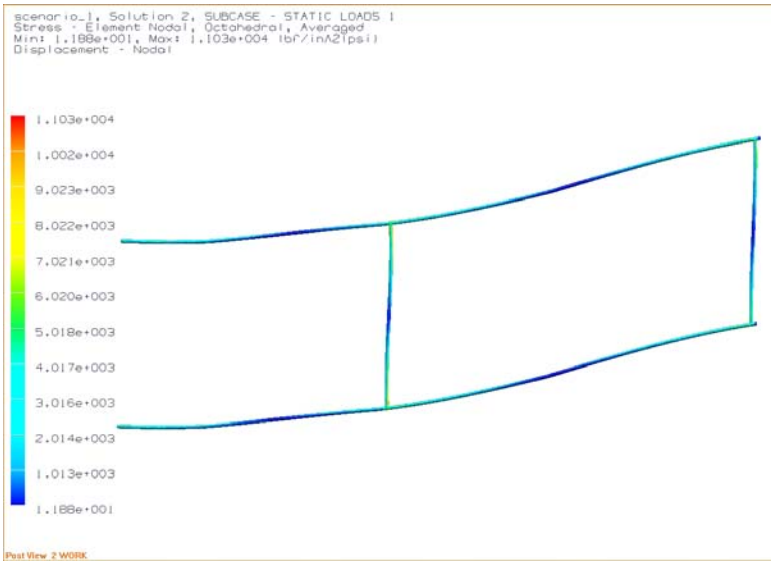

Figure 5.13. Overall stress distribution for a 108 lb point load.

Wall thicknesses were increased near the joint and joiner tubes used to connect the individual

tubes at the joints were also modeled now to more accurately represent the stress at the joint. The loading was discretized for an elliptic 2G load case. Difficulty was again found in generating adequately fine meshes due to the large length and small wall thicknesses. This problem was complicated further by the additional loads instead of point loads. Nonetheless, overall octahedral stress distribution from this case is shown in Fig 5.15.

Magnitudes of the stresses between the first test case and the second varied by an order of magnitude. The team is unsure why, although, this leads one to believe that this stress analysis provides merely qualitative results. More experience is necessary to trust the results from finite element stress analysis and use it to size the spars and struts.

Stress results were inconclusive at best and were suspended on the project for three reasons: the difficulty generating an adequate mesh of the desired structure, the team's significant inexperience with finite element methods, and the time constraints in finishing the scale model. It was felt that the team did not possess adequate experience to validate the results from the stress analysis and trust them. Regardless, before final construction of the aircraft significant stress analysis of all major components including wing and tail spars, struts, tailbooms, and fuselage structure should be conducted. Once local stresses are known, buckling analysis should also be conducted. A variety of loading conditions would prove instructive including the 2G pull-up, entering into a turn, a steady-state turn and gust loading. The safety factors necessary for a light enough structure for this project to be feasible are very low and warrant significant analysis before one can entrust pilot safety to the design.

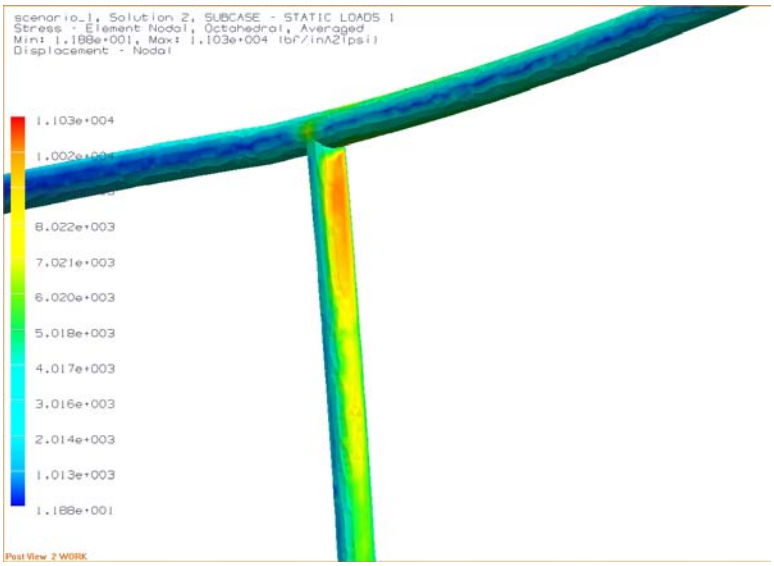

Figure 5.14. Octahedral stress distribution near the mid-span joint.

Due to the preliminary nature of several of the major aircraft components, center of gravity calculations would be rough at best. However, initial analysis shows that as long as the pilot

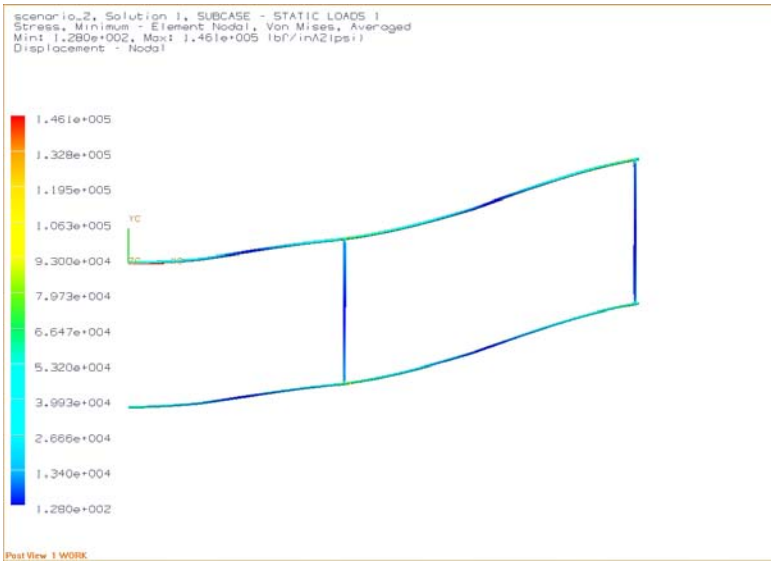

Figure 5.15. Overall octahedral stress distribution for 2G distributed load.

is placed somewhat ahead of the wing aerodynamic center, the aircraft will balance. This exact location should be defined after component sizes are finalized and a more accurate weight statement can be made. A current listing of component weights can be found in Table 5.1. It shows that a 148 lb pilot could still fly the aircraft at the design gross take-off weight of 215 lbs.

Table 5.1. Structural Weight Breakdown

Component	Weight [lb]
Wing spars and struts	25.3
Tailboom	21.7
Rudder Spar	0.16
Elevator Spar	0.80
Wing Ribs and secondary structure	1.56
Tail secondary structure	0.50
Fuselage Frame	5.00
Covering	2.00
Propeller	2.00
Drive Train	3.13
Miscellaneous Hardware	5.00
Pilot	148
	215 lbs

Additional design work could analyze several aspects that may lead to lighter structures. The aforementioned problem of the ratio of strut stiffness to spar stiffness requires more in depth investigation. Also, different strut configurations including non-perpendicular alignments may be

useful. If these changes prove beneficial, a wider range of pilot weight may be achievable. At any event, preliminary sizing shows that with a very small safety factor, the aircraft is capable of the desired structural performance and winning the Kremer prize.

6. Stability and Control

6.1 Requirements

The stability and control requirements were determined based on the mission requirements. Because the pilot is both the propulsion and pilot it was determined the airplane must exhibit significant natural static stability. Further the plane must exhibit positive directional stability. The dynamic motion must be either stable or have long periods. The HPA must be capable of turning at a rate sufficiently fast for completion of the course. The design philosophy followed for the aircraft was to carefully examine the mission, set the requirements for longitudinal and directional control power and stability, develop an initial control scheme derived from examination of similar aircraft, analytically surface sizes, select center of gravity location and dihedral from parametric study with a simplified layout using a vortex lattice code. Finally, a more detailed model was developed to preform final verification that the requirements were met.

6.2 Longitudinal Stability

To ensure minimal pilot longitudinal control effort the HPA was designed to exhibit significant longitudinal stability for a range of pilot weight in normal operating conditions. The horizontal tail size and center of gravity location were selected such that longitudinal motion is stable, the pilot has a full range of controllability, and both parasite drag and trim drag remain low.

Table 6.1 contains the horizontal tail volume coefficient for several HPAs. The table indicates most HPAs have a horizontal tail volume coefficient around that typical for sailplanes about $V_H = 0.5$[20].

Aircraft	Horizontal V_H
Monarch B[2]*	0.49
Musculair 1[21]*	0.57
Bionic Bat[21]*	0.41
VELAIR 89[21]*	0.35

Table 6.1. Horizontal tail volume coefficients of representative HPAs. *Note these values were estimated from drawings in the cited text.

Because the pilot is both the propulsion system and pilot, it should not be expected that he maintain a heavy work load due to insufficiently stable aircraft. Thus the aft limit of the center of

gravity was selected to be that which guarantees the aircraft be 10% stable. The forward limit was selected to insure the HPA has enough longitudinal control authority by guaranteeing the ability to trim the aircraft in cruise without excessive rudder deflection ($\delta e \leq 8\,\text{deg}$). For a typical aircraft, the tail size may be selected from these constraints and with the known CG travel. HPAs have no real center of gravity variation in flight with the exception of variation due to shift in pilot weight. However, it was desired that the aircraft preform effectively for a range of pilot weights. For this reason a minimum of 5% mean aerodynamic chord or $0.05\bar{c}$ (only about 1 in) allowable shift in CG in both directions was required. Figure 6.1 depicts the design space for horizontal tail volume coefficient and center of gravity location. Both the left and right limits for center of gravity are plotted along with the stablitity limit. The selected tail size is indicated in the figure as well.

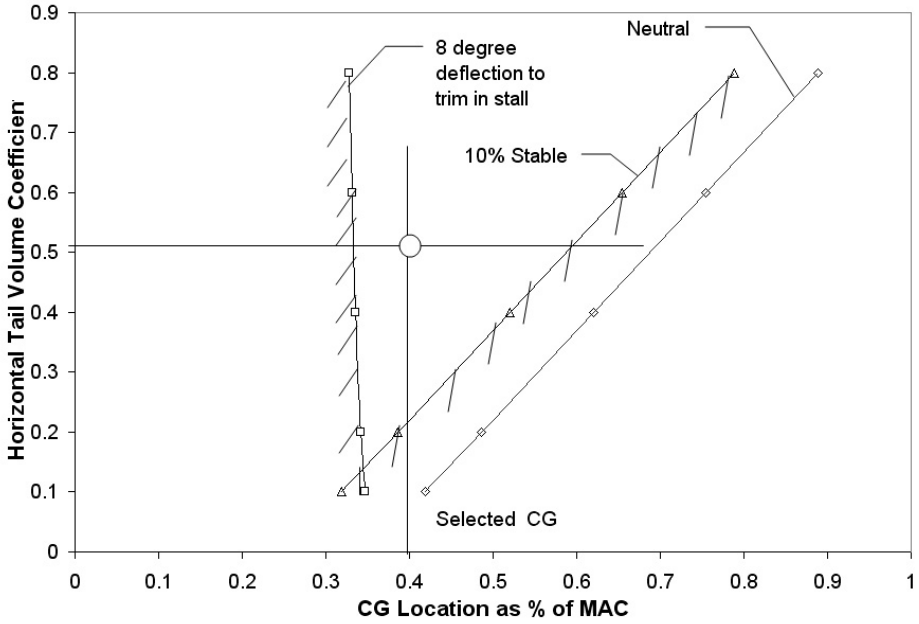

Figure 6.1. Design space for determination of tail volume and center of gravity location

The center of gravity location was selected based on the induced drag on the tail while trimming the aircraft in cruise. The induced drag in cruise was plotted against center of gravity location in Fig. 6.2. The figure indicates a minimum drag for a center of gravity location of about 35% MAC; however, the center of gravity was selected to be at $0.4\bar{c}$ to allow for 5% CG shift and not cross the forward center of gravity limit with a horizontal tail volume coefficient of $V_H = 0.5$.

For monoplanes, the vertical CG location has negligible effect on stability; however, for a biplane with a large gap to chord ratio, the vertical center of gravity location is critical as a large moment may be produced at high angle of attach. This is illustrated through Fig. 6.3. When the center of gravity is located within the lower wing, the lift on the top wing produces a stabilizing moment at

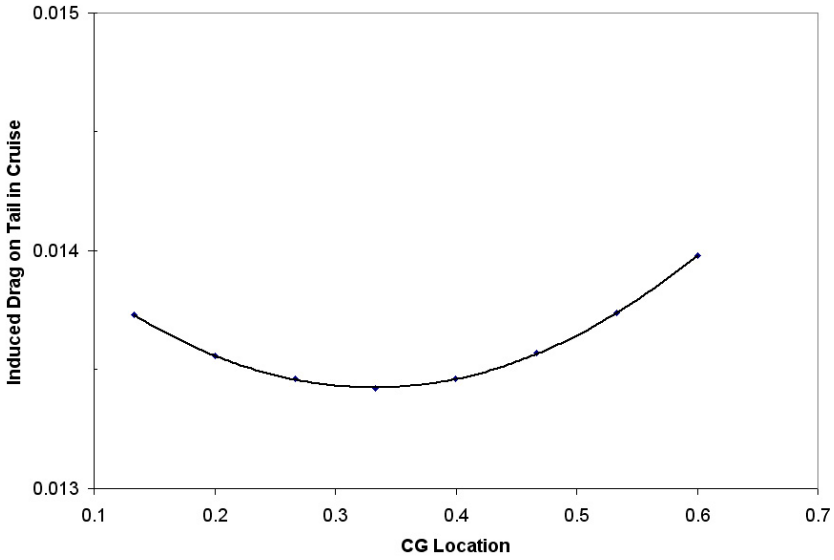

Figure 6.2. Trim drag verses center of gravity location for trim in cruise

high angle of attack. The effects of vertical CG location are seen in Fig. 6.4. The figure illustrates that for a CG located above center, the airplane becomes unstable at positive angle of attack. Similarly, for CG located below center, it becomes unstable at negative angle of attack. Thus a CG located at the middle of the wings was desired.

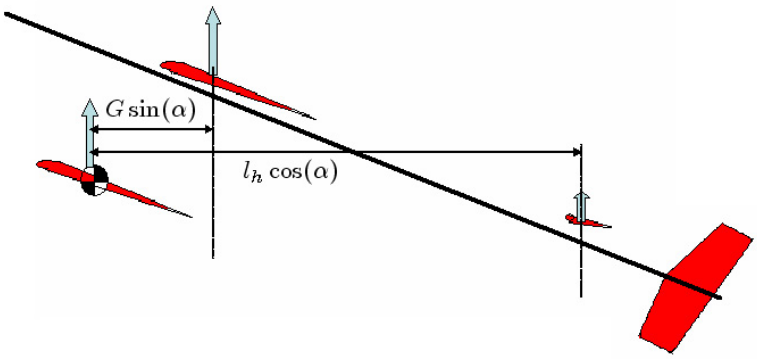

Figure 6.3. Illustration of biplane at high angle of attack depicting effect on stability

6.3 Lateral Stability and Control

The selection of the rudder size, aileron size, and dihedral was performed on the bases of lateral stability and controllability through parametric study.

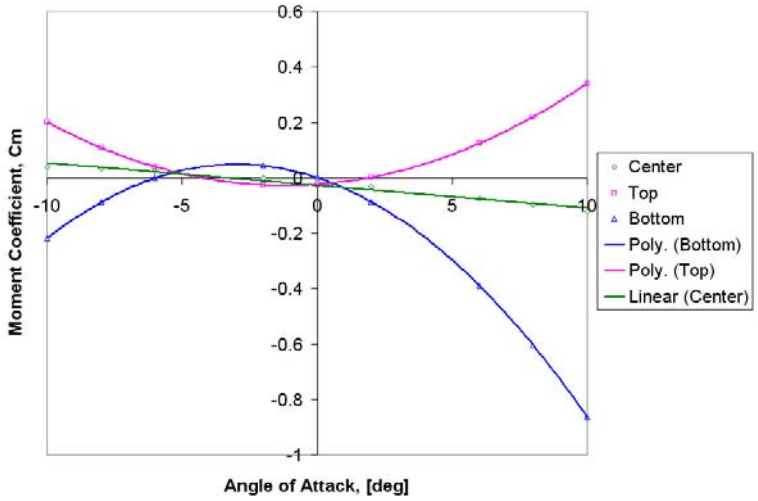

Figure 6.4. Pitch moment with angle of attack for varying center of gravity locations

The role of the vertical tail is to provide directional stability and yaw control. Initial sizing was estimated based on the typical vertical tail volume coefficient. Table 6.2 contains the vertical tail volume coefficient for several HPAs. The table indicates HPAs typically have a vertical tail volume coefficient is about 0.035. This was used as an initial estimate. Formal assessment of directional stability, steady bank, and cross-wind landing were used to specify the tail volume coefficient.

Aircraft	Horizontal V_H
Monarch B[2]*	0.035
VELAIR 89[21]*	0.045
Bionic Bat[21]*	0.030
Musculair 1[21]*	0.02

Table 6.2. Vertical tail volume coefficients of representative HPAs. *Note these values were estimated from drawings in the cited text.

To determine the appropriate tail size a simplified model was created using AVL. The wings were divided into only two panels so that the dihedral could be varied easily without significant remodeling work. Figure 6.5 contains a picture of the simplified model used to analyze the lateral directional control sizes for the aircraft. The smallest rudder tail volume such that the aircraft exhibit significant directionally stability, required less than 5 deg of deflection to land in the most severe cross-wind possible ($\beta = 11.3\,\text{deg}$), and required no more than 9 deg deflection to maintain a banked 15 deg turn was selected. In Fig. 6.6 each of these three constraints are examined. Naturally, increasing the tail size increases directional stability, but it also increases the rudder deflection needed to land in a cross-wind. Further the required deflection to maintain a 15 deg bank angle in a turn is minimized at a tail volume of about 0.06. A tail volume coefficient of 0.05

was selected because it provides good directional stability, requires about 5 deg rudder to land in a cross-wind and nearly minimum rudder deflection in a steady-state turn.

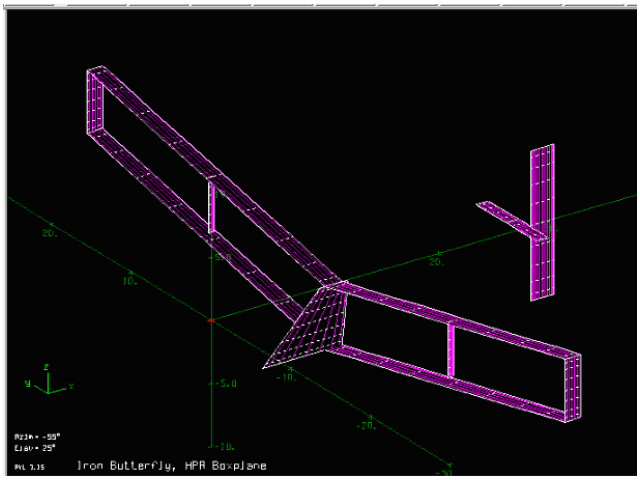

Figure 6.5. AVL model used for lateral control sizing

The wing dihedral was critical for turning. In a steady state turn the rolling moment must sum to zero. Monarch relied on an effective dihedral (C_{l_β}) of about 11 deg to counter the roll due to yaw rate (C_{l_r})[2]. Typically the effective dihedral angle lies between 10 and 13 deg. The design philosophy followed for dihedral angle selection was to use a straight dihedral model to perform parametric study to determine the variation in rudder deflection and slip angle for a coordinated turn with dihedral angle. The results would be confirmed on a more sophisticated polyhedral model with the same effective dihedral. The results are seen in Table 6.3. The results indicate the required slip angle in a coordinated turn decreases while the rudder deflection increases with increasing rudder size. As a trade off a dihedral angle of 11 deg was selected. A realistic polyhedral design was employed to provide an effective dihedral of 11 deg. The polyhedral is described in Fig. 5.11.

Dihedral Angle, Γ	Rudder Deflection, δr	Side Slip, β
10 deg	8.0 deg	5.5 deg
11 deg	8.8 deg	4.6 deg
13 deg	9.6 deg	3.5 deg

Table 6.3. Variation in steady-state coordinated turn deflections with dihedral

6.4 Rolling the Aircraft

The problem of turning HPAs may be related to the large span, low speeds, and extreme light weight. Early attempts to win the Kremer Prize were unsuccessful due to the inability to turn

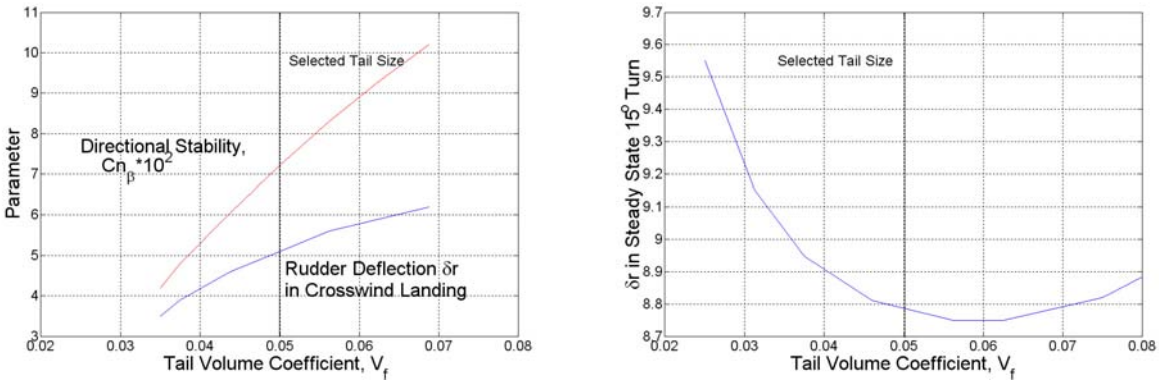

(a) Cross-wind landing and directional stability.

(b) Rudder in steady turn.

Figure 6.6. Vertical tail sizing

rather than the low power available. Initial explanation for the difficulty was attributed to the apparent inertia; however, more recent study has attributed the difficulty to turn to a damping effect rather than inertial[7].

The rolling inertia of an extremely light airplane will contain a component related to the apparent mass. The component results from additional energy needed to accelerate a body of air around the wing of the airplane as well as the airplane itself. For HPAs this effect is substantial. The apparent mass is equivalent to the mass of the circular cylinder of air around the wings. For the Gossamer Condor, the apparent inertia in pitch and roll are 140% and 440% of the actual moments of inertia[7]. Thus conventionally sized surfaces may not be sufficient to accelerate the HPA at the desired rate. Apparent inertia effects must be considered.

The effect of inertia simply restricts the ability to acquire excessive accelerations. There is no restriction making a given roll rate unattainable. This effect alone does not completely describe the rolling difficulties for HPAs. The effects of substantial span and low speeds results in a damping force apposing the rolling motion. A measure of the importance of roll damping may be characterized by the damping time constant defined by Eq. (6.1)[7].

$$\tau_{roll} = \frac{\dot{\phi}}{\ddot{\phi}} \approx \frac{24 I_{roll}}{\rho V b^3 \bar{c} m} \tag{6.1}$$

Where the roll rate is $\dot{\phi}$, the roll inertia is I_{roll}, and m the lift curve slope. If the roll inertia is calculated as purely the inertia of the column of air around each wing, the time constant may be compared to other HPAs in the Table 6.4.

The ineffectiveness of ailerons for primary roll control may be seen by considering a single degree of freedom model in principle coordinates. The equations of motion are:

Table 6.4. Approximation of first order roll time constant for HPAs

HPA	Time Constant τ_{roll}[s]
Condor[7]	0.10
Musculair II[7]	0.05
Iron Butterfly	0.05

$$I_x\dot{p} = L_v v + L_p p + L_r r + \Delta L_c \tag{6.2}$$

Where the control is applied through ΔL_c. In the simplest case when $v = r = 0$ the effect of step aileron deflection is a step deflection of a first order system. Thus the steady state roll rate for a step aileron deflection may be expressed as[20]:

$$p_{ss} = \frac{2VC_{l_{\delta a}}\delta a}{C_{l_p}b} \tag{6.3}$$

Further Eq. (6.3) may be rewritten in terms of the $C_{l_{\delta a}}$ required to achieve a given steady state roll rate. To achieve a roll rate of 10 deg/sec at an aileron deflection of 15 deg, $C_{l_{\delta a}}$ must be at least 0.47. Table 6.5 shows estimates for $C_{l_{\delta a}}$ for different aileron sizes. Note aileron size is defined as the length of aileron from the wing tip and the % chord the aileron occupies. The table indicates that for any realistic aileron size, inherited roll damping prevents turning at the desired roll rate. For this reason, it was determined that ailerons alone would be insufficient and yaw-roll coupling needed to be employed.

Length	% Chord	$C_{l_{\delta a}}$
15	40	0.311
30	40	0.430
15	50	0.351
30	50	0.485
15	60	0.380
30	60	0.520
24	60	0.470

Table 6.5. Ineffectiveness in HPAs to create 10deg/sec roll rate

As Table 6.5 indicates, conventional sized ailerons are insufficient. Over sized ailerons were used in the past on Musculair I, and II[7]. However, as it was seen in Table 6.5 this may still be insufficient. Further problems such as aileron control reversal further complicate the roll problem. For these reasons the Gossamer Condor, Daedalus, and Monarch relied on secondary roll generated through yaw-roll coupling[7]. For the Iron Butterfly, the primary roll control system utilizes yaw-roll coupling through deflection of the rudder. The roll control is supplemented through deflection of ailerons. The ailerons were designed to occupy the outboard 15 ft of the 30 ft semi-span. The

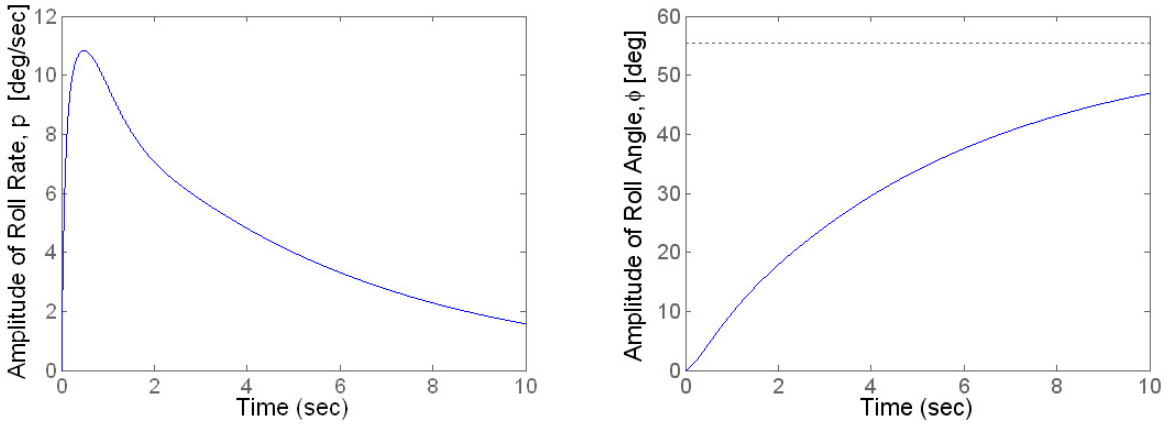

(a) Roll Rate p. (b) Roll Angle ϕ.

Figure 6.7. Response of Iron Butterfly to Aileron-Rudder Step

hinged at the $0.7\bar{c}$ position occupying 30% of the chord.

A six degree-of-freedom(DOF) dynamic model was developed and used to verify the ability to turn with the specified control system. Figure 6.7 indicates the roll response of the aircraft with application of 15 deg aileron deflection and 8 deg rudder deflection. The figure indicates a peak roll rate of about 11 deg/sec occurs and is diminished as time progresses. Also plotted in Fig. 6.7 is the bank angle as a function of time corresponding to the step control deflection. The figure indicates appropriate roll response. The desired 15 deg bank angle is acquired within 1.6 sec.

6.5 Dynamic Stability

Iron Butterfly was required to be dynamically stable in all modes except spiral. The spiral mode was required to be stable or have a time to double amplitude greater than 10 sec. HPAs in general do not exhibit spiral stability; however, the instability grows slow enough that the pilot may maintain control of the aircraft. It was required that the time to double amplitude be no less than 20 sec. Small perturbation theory was used to obtain the longitudinal and lateral directional modes. The eigenvalues for longitudinal motion of both the aircraft and quarter-scale model may be seen in Table 6.6. For a typical aircraft there are two oscillatory longitudinal modes. However, Iron Butterfly experiences a single oscillator mode (Phugoid mode) and then a pair of stable real exponential modes. The first real mode has a time to half amplitude ($t_{1/2}$) of 0.13 sec and the second has $t_{1/2}$ of 0.02. This structure of longitudinal dynamics is typical for HPAs and was felt on Monarch and Chrysalis[2].

The lateral-directional modes were found in a similar fashion. These modes are summarized in Table 6.7. The lateral-directional modes are characterized by a pair of complex eigenvalues

representing the dutch-roll mode and two real stable roots. The first stable root represents the highly damped roll mode, the second is the spiral mode. It must be noted that unlike most HPAs the spiral mode is stable; however, it is marginally stable. The spiral mode is characterized by a time to half amplitude of 11.6 sec. The criteria for dynamic stability were met.

Table 6.6. Eigenvalues and time to half amplitude for longitudinal dynamics

Eigenvalue	Time to half [sec]	ζ	ω
-34.7	0.02	-	-
-5.3	0.13	-	-
-0.072 + 0.74i	9.70	0.17	1.05
-0.072 -7.4i	-	-	-

Table 6.7. Eigenvalues and time to half amplitude for lateral-directional dynamics

Mode	Eigenvalue	Time to half [sec]	ζ	ω
Dutch Roll	-4.92+3.51i	0.14	6.04	0.81
-	-4.92-3.51i	-	-	-
Roll	-2.03	0.34	-	-
Spiral	-0.06	11.6	-	-

6.6 Requirement Compliance Assesment

The analysis provided in the preceding section has indicated the concept Iron Butterfly is capable of preforming the requirements set by the mission. The aircraft demonstrates significant longitudinal and lateral-directional stability. The aircraft is capable of preforming a steady state 15 deg banked turn without excessive control deflection or side slip. The aircraft is capable of landing in a severe crosswind situation. The eigenmodes indicate the aircraft will experience good dynamic properties. It must be noted that small perturbation theory was employed to preform the dynamic analysis. However, more complete nonlinear integration to simulate the dynamic response of the aircraft in realistic flight scenarios could prove invaluable. The aims of this design team were to preform such "simulation" through a dynamically similar 1/4 scale model. The details of the dynamic similarity as well as the flight test results are described in Sections 9.5 and 9.6 respectively.

7. Propulsion System

7.1 Human Power Production

Human power is something that has been studied thoroughly throughout the course of history, mostly in the realm of sporting competition. Many vehicles have relied on this most basic means of power production to meet their transportation goals in many different mediums. Upon closer inspection however, human power production is anything but simple. As with any propulsion system, a very basic conservation of energy equation can be written for the propulsion system:

$$E_{rxn} = W + Q \tag{7.1}$$

Here, E_{rxn} signifies the energy available from the burning of fuels from foods with oxygen while W and Q denote mechanical work and excess heat respectively. Maximizing the effective work is an extremely complicated function of many things. It depends on primarily the availability of fuel to burn and oxygen from the bloodstream. The human body, however, has several sources of energy.

The basic fuel for energy producing reactions in muscles is adenosine triphosphate (ATP) which is the high energy form of adenosine diphosphate (ADP). Oversimplifying, the body processes sugars and ADP into ATP mainly in two separate ways before ATP is used in an energy producing reaction which produces ADP and some other interesting byproducts. It is helpful to imagine ATP as ADP + energy + phosphate and to understand that the reaction goes both ways in the body. The highest power output can be obtained through anaerobic metabolism which, burns glucose obtained directly from a starch called glycogen and breaking it down through a reaction called anaerobic glycolysis. This reaction is complicated. It is, however enough for the purposes of this examination to realize that it does not usually involve oxygen and, in the end, it produces 4 ATP molecules and 2 other molecules known as pyruvic acid. However, one ATP molecule must be used to break down more glycogen to continue the process. Pyruvic acid is then converted into lactic acid by an energy-carrying enzyme that needs to get rid of some excess energy so that it may return and process more glucose. It is difficult to define how efficient this process is because as stated above, some energy is passed on to lactic acid which can be used different processes that create ATP. For the purposes of this discussion, it will be assume that the energy passed into lactic acid is lost. Under these assumptions, the process is on the order of 2% efficient. It is also important to note that the amount of glycogen available in the muscles is finite and comparatively low allowing for only a short period of exertion.

At the other end of the exertion spectrum lies aerobic metabolism. Aerobic metabolism relies on the break down of larger molecules like fatty acids and, to a lesser extent, amino acids to release energy. Aerobic metabolism can also use pyruvic acid as a fuel. This process takes place in the mitochondria of "slow-twitch" muscle fibers. Mitochondria are organelles which contain the

structure necessary to accept oxygen from the bloodstream. Highly trained athletes have increased mitochondrial density; a term meaning increased surface area (in the form of folds) within the mitochondria themselves allowing for higher oxygen absorption. Some energy in the form of ATP is made directly from the breakdown reactions but most of the energy is carried away through enzyme reactions to be made into ATP elsewhere. Again, drastic oversimplification is employed here, and, using the same glycogen as fuel, 37 ATP molecules are produced by this aerobic metabolism process. This process is on the order of 30% efficient. The only byproducts of this process are carbon dioxide and water which can easily be removed.

A purely aerobic effort in most people, however, does not produce enough power to operate a human powered aircraft. The effort required will be one which combines anaerobic metabolism and aerobic metabolism and makes use of the ability of the body to process lactic acid. Athletes train themselves largely based on a heart rate value that is associated with their lactic acid threshold (LT). This heart rate value is defined as the exertion level at which the mechanisms for processing lactic acid through aerobic metabolism can no longer keep up with its anaerobic production. It is above this heart rate at which lactic acid begins to build up creating a burning sensation. A second heart rate value is used at which the maximum volume of oxygen is processed by the body (VO2max). With training, large gains can be made in raising one's LT, however, VO2max is a quantity which, for the most part, is genetic and not trainable. The effort required here will be one between LT and V02max. Figure 7.1 shows plots for several different groups of people of their power output and oxygen consumption and the time for which they can maintain a cycling effort[22].

Two basic lines are shown. The lower of the two is for an average healthy man. The upper line is for first class athletes whom are most likely professional or elite amateur cyclists. Since there is little direction given by the Kremer prize rules on the subject, the power available will be based on this upper line. There are several important things that can be taken from this plot. It can be seen that in very short intervals where anaerobic metabolism can be used, power output can be very high. Note, however, that this graph uses a logarithmic scale along the x-axis, creating a false sense of sustainability. There is a leveling of the data around 10 min where the maximal sustainable effort level is LT. For the use of this design discussion an average intensity of 400 W will be chosen as sustainable for the duration of a 3.5 to 4 min effort. This is chosen such that slightly increased power demands due to flight conditions such as a headwind are not catastrophic.

A second factor to be optimized is the pedaling frequency. Slower pedaling frequencies are more efficient mechanically because they minimize the excess motion of the legs. However, at low pedaling frequencies, different muscle fibers are recruited than at higher pedaling frequencies. At low pedaling frequencies "Type I" fibers, which work predominately from anaerobic metabolism are recruited, creating a very powerful motion with extremely high energy usage. At higher pedaling frequencies "Type II" fibers, which work predominately with aerobic metabolism are used, produc-

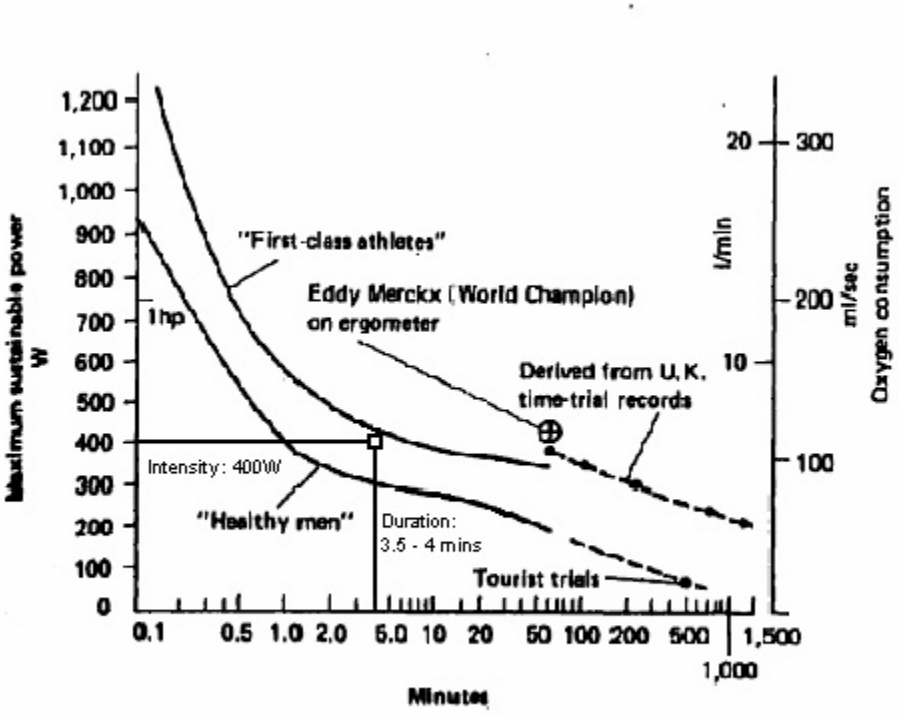

Figure 7.1. Maximum power, oxygen consumption and sustainable time for particular efforts[22].

ing a less powerful and more energy conservative motion. For these reasons, a balance between high and low cadence must be found. Below, in Fig. 7.2 adapted from Ball, the dependency of oxygen consumption on power output and pedaling frequency is shown[23]. It is important to note that the lines representing the experimental data have been artificially extended to reach the design point for this application.

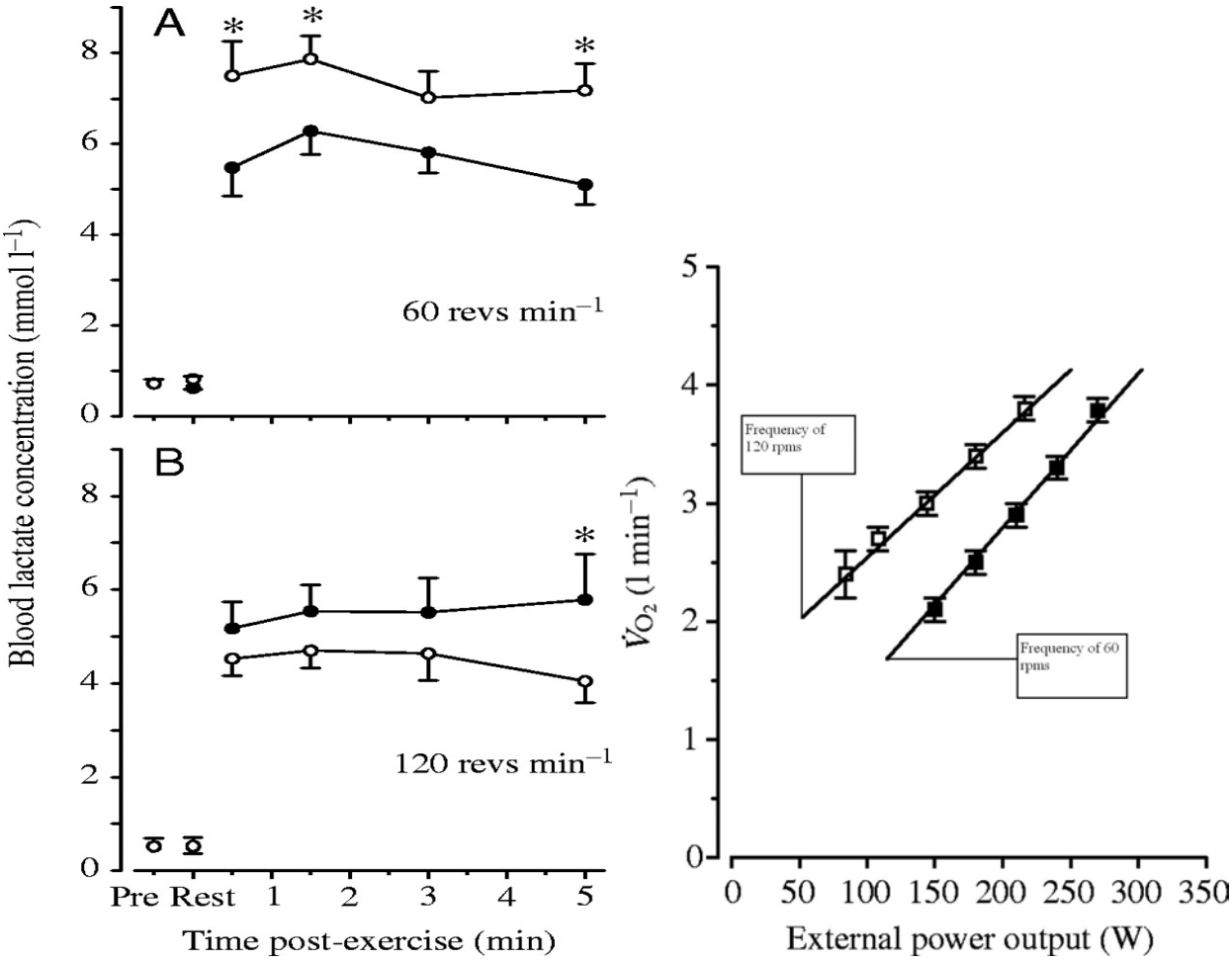

Figure 7.2. Dependency of oxygen consumption on external power output and pedaling frequency as well as the dependency of blood lactate concentration over time on pedaling frequency.[23].

In Fig. 7.2, it can be seen that blood lactate concentration is higher over all the post exercise measurements taken at 60 rpm than at 120 rpm. For the reasons above, a design pedaling frequency of 90 rpm will be used for this application. It appears that at this level there is a good balance of oxygen consumption, mechanical efficiency, and lactate production.

7.2 Cooling

Revisiting the issue of metabolic efficiency, it will be assumed that this effort is far closer to an aerobic effort than an anaerobic one and the overall efficiency of the pilot will be assumed to be 25%. This assumption appears to be a good one due to the fact that in Fig. 7.1 the chosen power output appears much closer in magnitude to the leveling region around the five minutes sustainable time than the maximal efforts around 0.1 min sustainable time. Very simply, a relation between efficiency, available power, and excess heat production can be written.

$$\eta_p = \frac{P}{\dot{Q}} \tag{7.2}$$

This equation shows directly that by picking a desired power output, $P = 400$ W, it will be necessary to dissipate 1600 W of excess heat.

From the above discussion, it is noted that there is a very significant amount of heat to be dissipated in some manner. For the purpose of the design of the cooling system, 2000 W will need to be chosen as an amount of heat that needs to be dissipated to account for variations in exertion level and surrounding temperature. The heat will dissipate in two ways: convection through the skin of the aircraft and a ducting system which will carry cool outside air and exchange it for warmer cockpit air. Eq. 7.3 describes the relationship of heat dissipation.

$$\dot{Q} = \dot{Q}_{conv} + \dot{Q}_{cond} \tag{7.3}$$

First, a general approach to the problem will be outlined. Both the heat flow through the duct and the heat flow through convection depend on the interior cockpit temperature. For the sake of simplicity, the cockpit temperature will be assumed to be constant throughout the interior of the fuselage and time invariant although obviously the interior temperature near the walls of the fuselage will be lower, and it will take time for the air inside the cockpit to heat. Effectively, an equilibrium cockpit temperature is being defined. In the limiting case that there is no duct flow, the cockpit equilibrium temperature will be very high. In this case all the heat is dealt with through convection. In the other limiting case that there is no convection, the duct will be very large and cause a great deal of drag. This is the essence of the trade off. Increasing duct size lowers the cockpit temperature but increases drag. A rigid constraint will be placed at 100^oF over which it will be assumed that power production becomes a problem for the pilot.

Looking more in depth at the convection term, several other things affect the amount of heat that can be dissipated in this manner. It is actually a two part problem. The first part in which the heat is passed through the skin is dependent on the surface area of the fuselage, the thermal conductivity of the skin material, k and the temperature gradient $(T_\infty - T_e)$ across the skin materials thickness, t.

Here the subscripts, e and ∞ denote the interior wall temperature and the exterior free stream temperature. Since the air inside the cockpit is assumed at a constant temperature and zero velocity, it can be assumed that the interior wall temperature is equal to the cockpit equilibrium temperature. The second part of the problem involves convection over the outside surface of the cockpit wall.

$$\dot{Q}_{conv} = hA(T_e - T_\infty) \tag{7.4}$$

$$\dot{Q}_{conv} = 0.664(Pr)^{1/3}\sqrt{Re}\frac{kA}{L}(T_e - T_\infty) \tag{7.5}$$

Eq. (7.5) from Schetz, applies only to a flat plate in laminar isothermal flow, but relates the heat lost through convection to the Reynolds number and Prandtl number[6]. The Reynolds number at any particular point depends on the length from the beginning of the surface and the local velocity. At this point it becomes necessary to assume a fuselage shape so that a velocity profile may be calculated. The fuselage shape was assumed to be a symmetric NACA 0036 airfoil to calculate the local velocities with a vortex lattice panel method. It is also important to note here that the assumption of a NACA 0036 airfoil likely makes the laminar boundary layer assumption in Eq. (7.5) invalid. However, since this is a purely theoretical fuselage shape and relations similar relations to Eq. (7.5) exist for turbulent boundary layers, only Eq. (7.5) will be applied to simplify the analysis method. At this point a m-file script was written in MATLAB®which performs the following:

1. Reads in velocity and position data along the airfoil surface obtained from a vortex panel method code.
2. Selects an amount of heat to be dissipated by convection.
3. Solves for the interior temperature by:

    - Starting with an exterior wall temperature equal to the surrounding temperature.
    - Breaking up the airfoil into many small flat plates with local velocities as found by the vortex panel method and local Reynolds numbers according to their position along the length of the airfoil surface.
    - Integrating the heat dissipation over the length of the airfoil surface.
    - Increasing the exterior wall temperature if the calculated heat dissipation is less than the selected.
    - Combining Eqs. (7.3) and (7.5) to calculate the interior cockpit temperature.

The equations for the ducted mass flow term are simple to evaluate.

$$\dot{Q}_{duct} = \dot{m}C_p(T_{eq,c} - T_\infty) \tag{7.6}$$

This was then used together with Eq. 7.3 to expand the MATLAB®code to do the following:

4. Calculate the amount of power needed to be dissipated through ducted flow.
5. Calculate the amount of mass flow needed for this ducted heat dissipation.
6. Calculate the amount of drag caused by slowing the free stream duct flow to rest in the cockpit as a worst case scenario.
7. Plot this amount of drag versus cockpit temperature.

The plot of this drag versus cockpit temperature is shown in Fig. 7.3. From the figure the a minimum drag of 0.08 lbs may be expected to result from the duct cooling system.

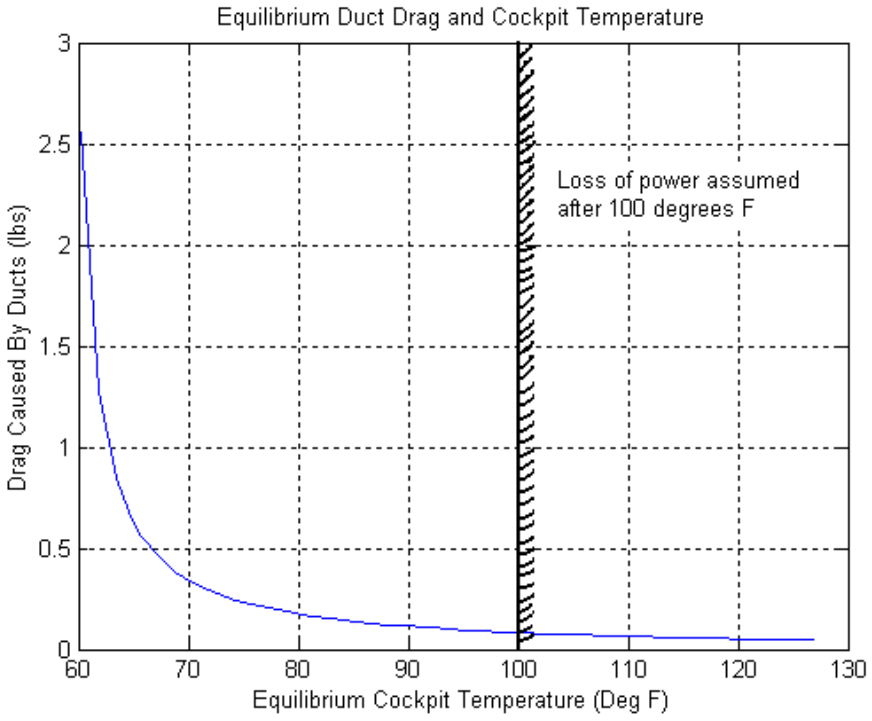

Figure 7.3. Result of MATLAB®code for duct design.

Further iterations of this code will take into account the real shape of the fuselage and boundary layer transition to turbulence. The drag estimate will also be further revised to resemble fully developed flow in a pipe through the cockpit. Still, despite the inaccuracies and assumptions, the trends reflected in the above plot reflect those in actuality and the magnitudes of the drag and cockpit temperature are close to the actual values.

7.3 Drive Train

7.3.1 Concept Development

The drive train of this aircraft has a simple mission. It must produce the highest efficiency with the lowest weight and smallest deflections due to the forces applied to it. For simplicity and historical success reasons, a bicycle-type drive train was chosen. There are several issues which must be resolved to use such a system in a human powered aircraft. First, the axis of rotation of the pedals will be ninety degrees offset from that of the propeller assuming the pilot is facing the same direction as the propeller. Second, the orientation of the pilot in the fuselage must be optimized for maximal power output. Finally, a decision should be made on the structure supporting the pilot and handling the drive train loads. To solve the first constraint, several ideas were considered. The decision matrix below in Table 7.1 details how the decision was made. Here, the figure-of-merits rating scheme of Section 3.3 was employed.

Table 7.1. Drive train decision matrix

Concept	Details	Efficiency	Weight	Resiliency	Total
1	Gear box attached to pedal bearing shaft; Drive shafts connect pedals, propeller	1	-2	1	0
2	Geared roller chain with bevel gear to propeller	0	0	0	0
3	Non-traditional plastic and twistable roller chain twisted 90 degrees	-1	2	0	1

The third option was chosen for its potential for light weight without intolerable losses in resiliency and efficiency. The challenge is to find a sufficiently strong chain which is flexible enough to take the twist. Despite this challenge, this path has been successfully taken in the past by the Gossamer Condor designers. Two promising candidates were selected from the WM Berg company: the “Flex-E-Pitch” line and the “Pow-R-Tow” line of drive chains.

7.3.2 Design Point Definition

At the heart of the drive train problem is the analysis and design of the structure and drive train components. To achieve this goal, it is necessary to assign a design condition on which the loads will be based. For the purposes of this analysis, this design condition will be one in which the pilot is producing the assigned 400 W, but at a cadence of only 45 rpm. This provides for a factor of safety of 2 over normal operating conditions, the 400 W at 90 rpm from Section 7.1). This is a high torque condition as it corresponds to 85 pounds of pressure on the pedals, but one that a normal person is completely capable of producing. It will be important that pilots be aware of this condition and not exceed it. By doing some simple calculations the drive train loads can be calculated. These values are shown in Fig. 7.4.

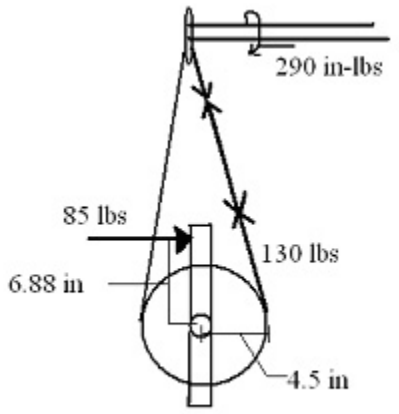

Figure 7.4. Drive train loads and dimensions. The dimensions shown are for standard off the shelf bicycle components (which are usually measured in millimeters).

A gear ratio between the lower chain ring and the upper gear was chosen of 2:1 such that the pilot can pedal at a 90 rpm while the propeller turns at 180 rpm.

7.3.3 Detailed Part Design

To fulfill the light weight requirements of this drive train application, improvements in weight must be made over conventional bicycle components. Bicycle components must be designed for many years of use at relatively high torque to sustain use under much more stringent design conditions than will be required for this application. Since the pilot will be positioned in a recumbent position, it will be impossible for them to put all of their weight on the pedals. Also, the aircraft is meant to fly at a specific power output and will be geared to achieve this output at a specific cadence. The pedal crank arms and pedal bearing axle will therefore be designed to carry these loads with an additional factor of safety of two. To minimize weight and displacement, the "paperclip" crank arm concept shown in Fig. 7.5 below was developed which maximizes the moment of inertia of the cross section to resist bending from pedal force with a minimum amount material.

As can be seen from the design, the part is a hollow shell at the ends and has a large slot in the middle to minimize weight. In further efforts to reduce weight, the pedal crank arms will be produced from a cast magnesium alloy. Magnesium alloy AZ91C was chosen for its extremely high stiffness with very low density when compared with other metals like aluminum and steel. It is known that parts magnesium alloys are not as durable as parts made from aluminum or steel, however this is not a large concern considering the mission of the aircraft.

To design the dimensions of the crank arms, a three dimensional computer (CAD) model of the part was constructed in Unigraphics NX 3.0. The CAD model was then analyzed by Unigraphic's

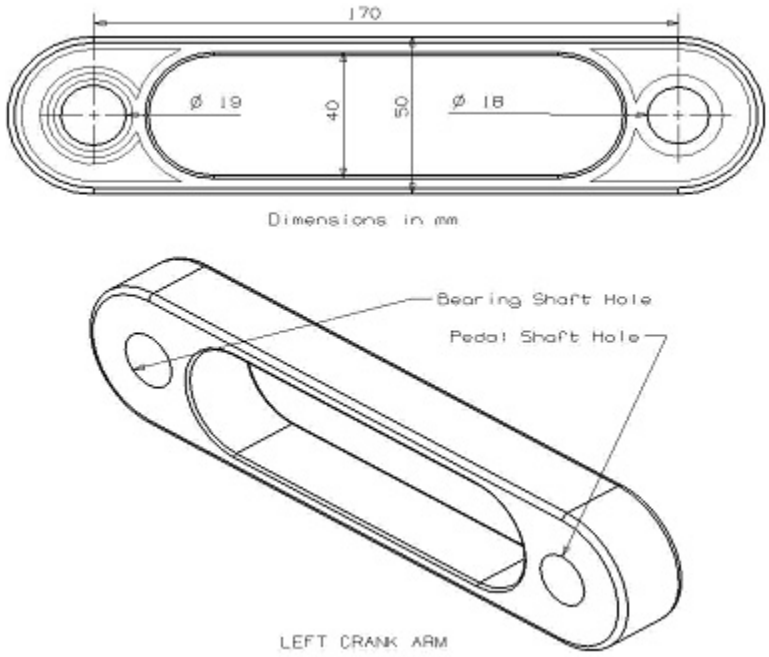

Figure 7.5. Left Pedal Crank Arm.

proprietary finite element structural analysis code, Structures P.E. Brief calculations were done previously to determine a test case load of 85 lbs. Using a fixed constraint applied to the crank bolt hole and point load and moment applied to the pedal shaft hole, it was found that the crank arm would deflect .063 in for a crank arm of length 6.7 in (a standard bicycle crank arm length). It was further found that in this configuration the maximal Von Mises stress was 10600 psi, significantly less than the yield strength of the magnesium alloy (15000 psi). Finally the weight of the part is 6.15 oz., a savings of 1.41 oz. over a popular high end bicycle component. Figure 7.6 shows the finite element model with exaggerated displacements. The different colors denote different values of octahedral stress in the part.

The right crank adds a web feature to which the chain ring will be attached. With the additional web feature, the right crank weighs 6.35 oz. The pedal bearing axle was designed in similar fashion to the crank, using Structures P.E. Figure 7.7 shows the dimensioned shaft below and has a weight of 0.8 oz. It was found that under the design torque of 290 lb-in the shaft twists negligibly and has a maximal stress values that are orders of magnitude less than the yield strength of the chosen aluminum material for this part.

Because the chain ring and gear are thin cast parts which do not require much material, they will be made from aluminum for cost savings over magnesium. The chain ring and gear weigh 4.26 oz. and 2.12 oz. respectively. The final part to be designed is the propeller shaft. This part experiences very low loads. It will be made from extremely thin aluminum tubing with a wall

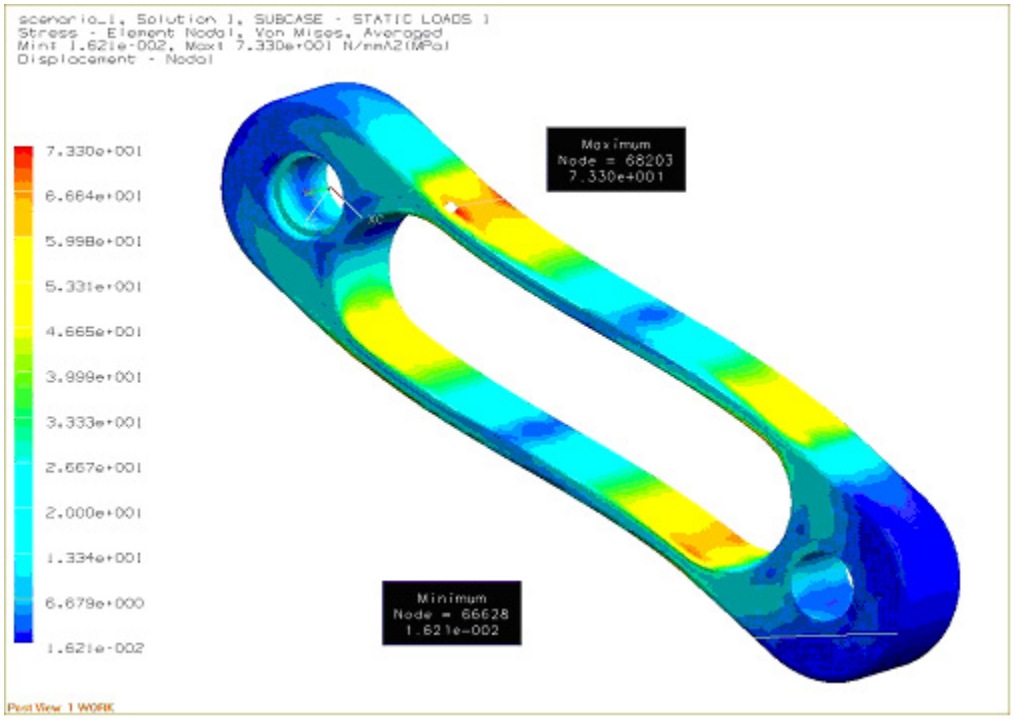

Figure 7.6. Finite element model of crank arm with exaggerated displacements.

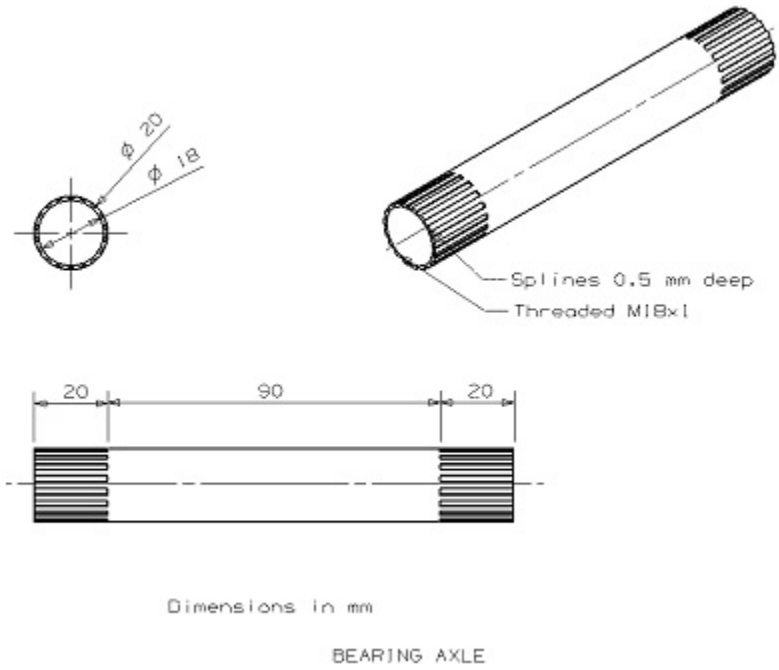

Figure 7.7. CAD of bearing axle shaft.

thickness of 0.04 in. and will weigh 8.75 oz. Table 7.2 details the weights and positions of all the drive train components. The total weight of the drive train is very light at just over 3 pounds.

Table 7.2. Propulsion Weights Table

Part	Material	Weight [oz.]
BB shaft	6061 Al	0.8
BB Bearings	6061 Al	4.24
Left Crank	AZ91C Mg	6.15
Crank Bolts	6061 Al	1.34
Right Crank	AZ91C Mg	6.35
Chain Ring	6061 Al	4.26
CR Bolts	6061 Al	0.13
Gear	6061 Al	2.12
Prop Shaft	6061 Al	8.75
PS Bearings	6061 Al	4.24
Chain		12.32
TOTAL		**50.7**
		3lbs 2.7 oz.

7.4 Pilot Positioning and Seat Design

The issue of positioning the pilot within the fuselage depends on three factors. First and foremost the pilot constitutes a very large fraction of the gross weight of the aircraft and hence needs to sit as close to the aerodynamic center of the wing as possible. Next, the pilot's orientation must be decided. It is important that the pilot be able to see forward to fly the aircraft. Also, for compatibility in training purposes the pilot's orientation must be as close to that of a normal bicycle as possible. The relevant parameters for the similitude of pedaling position are the knee and hip angles at the fully extended position. These angles should be about 175 deg and 90 deg respectively. The 90 degree hip angle requirement sets the angle between the seat back and the line between seat and crank arm axle. The 175 degree knee angle forces the seat to be fore-aft adjustable since no two people are likely to have the same leg length allowing for the same knee angle at a given seat position. Using these constraints, a rough geometric cockpit layout is shown in Fig. 7.8.

The seat position was designed to be adjustable by the use of a two-bolt tube-shaped clamp. The seat frame itself is constructed of very thin bent aluminum tubing and is covered with rip-stop nylon fabric. The assembly drawings of the drive train and fuselage structure, including seat, are shown below in Fig. 7.9 the assembly drawings of the drive train and fuselage structure shown below. The fuselage structure was designed such that members were oriented in the direction of the primary loads on the structure. These loads are predominately vertical, due to the weight of

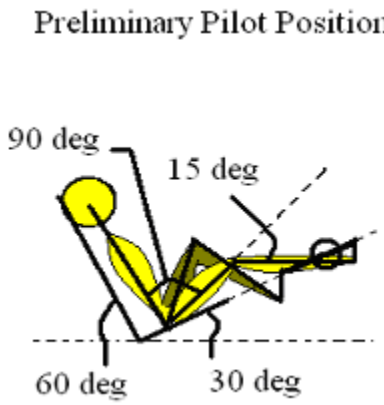

Figure 7.8. Shown are the approximate necessary angles for maximum power production and comfort. These angles will change slightly based on personal preference.

the pilot and lift of the wings, and in the pedal direction due to the pressure applied to the pedals.

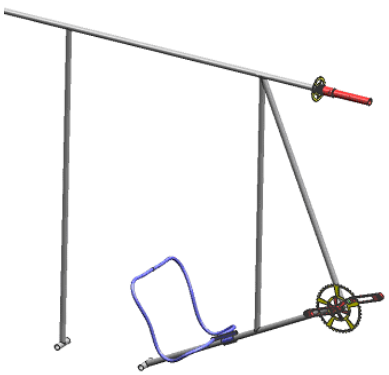

Figure 7.9. Drive Train Assembly.

8. Propeller

In this slow flight regime, a propeller is the most efficient and lightest means of propelling an aircraft and has accordingly been selected for the final design. Given the limited power available and the miniscule power margin of which the aircraft operates, every bit of pilot power must be utilized. However, propellers used on general aviation planes operate on the order of between 75 to 80% efficiency. At the 400W power level, this corresponds to an 80 to 100W power loss simply from the propeller, an unacceptable result. Consequently, the situation required a propeller designed for

this specific flight regime with a target efficiency of 90%. The purpose of this prop design was then to maximize the prop efficiency while minimizing its weight. There are three things that are very beneficial in this design, however. The first is that acoustic noise, normally a major design factor, is irrelevant. Second, the low disc loading[8] allows for small angle approximations to be made in the analysis, while the third is the low rpm at which the prop can spin with very little gearing (it actually spins faster than the engine, a rarity in prop design).

8.1 Design Method and Results

Propeller design is primarily a function of diameter, chord, twist, rpm, and airfoil. In general, the larger the propeller diameter, and lower disc loading this causes, the more efficient it is. The first step in any propeller design is to determine how large a prop one can have. This dimension is limited by geometry, Mach number effects at the tip, and weight. Geometrically, the prop is limited to approximately the current gap between wings to allow for ground clearance. This is a radius of 54 in. For most aircraft, tip Mach number effects are the limiting factor on length. However, this turns out to not be a factor, as at this radius and a relatively high rpm of 360, the tip barely approaches Mach 0.15, and flow about it can still be regarded as incompressible. This is due to 360 rpm being very low for a prop design. Finally, weight is a complicated function of geometry and construction details, and optimization for weight is saved for a later exercise.

The first cut prop design procedure can be summarized as follows:

1. Determine maximum size from geometry
2. Choose the number of blades. For a given mass, using fewer blades is generally more efficient, as it allows the maximum radius prop. In the limiting case, using a one-bladed prop would be very efficient, but the weight needed to counterbalance it is significant. For this reason, a two-bladed prop was selected.
3. Use a flat plate airfoil (or maintain a consistent airfoil between designs). The consistent airfoil section will allow one to isolate the effects of twist and chord, and find the ideal case.
4. Choose a reasonable rpm. 180 rpm was selected given the available gearing ratios. This step specifies a propeller advance ratio in cruise of 0.389.
5. Choose a reasonable lift coefficient C_L. Here, $C_L = 0.8$ was used, as L/D_{max} occurs at this C_L for several airfoils that operate at the Reynolds numbers this propeller sees.

With these variables specified, it remains to optimize the twist and chord for minimum induced loss. An analysis technique was proposed earliest by Glauert in 1936, with a combination of momentum theory and blade element theory.[24] This analysis was restricted to lightly loaded propellers. Using Betzs proposed minimum induced loss span, a design procedure can be constructed using graded momentum theory, which was popularized most recently by Eugene Larrabee[25]. This

[8] Disc loading is defined to be the thrust force on the prop divided by the swept area of the prop disc.

method uses the Betz-Prandtl tip loss correction factor. This has the undesirable effect of reducing the analysis to apply only to lightly loaded blades[9] and low advance ratios, but this is sufficient for the entire HPA flight regime. Despite its usual disadvantages, it is a quick way to get a reasonable performance propeller, and a good place to start, and was used in early design iterations.

An improved design method is the use of potential flow formulation. This design approach is not restricted to lightly loaded blades or low advance ratios, for one solves for the entire helically-symmetric potential flow through a streamtube downstream of the propeller. In essence, the helicoidal vortex sheet that makes up the streamtube can be likened to a rotating rigid screw, whose downstream motion is similar to the apparent motion of a rotating barber pole. This method thus gives a better consideration of the energy imparted to the flow downstream, and the impact on thrust and efficiency. However, these equations must be numerically solved and can become computationally intensive, so the praxis of this theory has historically been a final optimization of a propeller arrived at through another means, and was in the Iron Butterfly design as well. Reference was also made to Adkins' and Liebeck's work regarding the nonlinear prop flow solution with the inclusion of limited downstream viscous effects[26].

Finally, in recognition that many propeller optimizations are conducted to evaluate the cruise thrust and power conditions but that few design methods consider the static case, an in-house MATLAB script was developed to allow for static thrust predictions. This was based on blade element integration of airfoil strip theory along the radius of the blade, and considered only the conditions at a differential section of the blade, ignoring tip vortex effects. All three of the design procedures described above: Larrabees procedure, the potential flow formulation technique, and the blade element method were used in an iterative manner to determine a reasonable propeller geometry. Generally, Larrabees procedure was the starting point, the potential flow formulation used to modify this result, and finally, static thrust conditions were verified using the blade element method. The numerical solution for the potential flow analysis has been automated in FORTRAN under the name XROTOR[27]. This program is maintained by Mark Drela at MIT and was written for a Unix-based machine. It has been used very successfully in the past for HPAs such as MITs Daedalus. The team acquired access to Unix workstations and compiled the routine. In this routine, one is generally concerned with adjusting the span loading of each blade to minimize induced loss. Since one typically designs for a constant C_L throughout the blade, the chord and angle of attack is instead varied to adjust the lift distribution. As such, a plot of CL versus radius is almost meaningless; it is instead much more instructive to plot circulation versus radius. This is done for the prop designed for this airplane in Figure (8.1) along with the local C_L and local efficiency factor η.

Note that the very inboard section does not contribute to the lift. This inner hub radius was neglected in the lift calculations because not only is there often a spinner in this area, any blade

[9]Note the distinction between a lightly loaded disc and lightly loaded blades: a highly loaded disc can have lightly loaded blades simply by increasing the number of blades.

in the area is moving so slowly that its contribution to the lift is negligible, as can be seen by the tendency of the local efficiency η to drive towards zero as the local radius r becomes small. By integration of this local efficiency, one can obtain the total efficiency of the propeller, in this case 89.2%. Note that the circulation plotted has been non-dimensionalized, by the number of blades B, velocity V, and tip radius R. The circulation as a function of radius is well-developed and approaches the lift distribution Betz proposed, which is the propeller equivalent of an elliptic spanload for a wing.

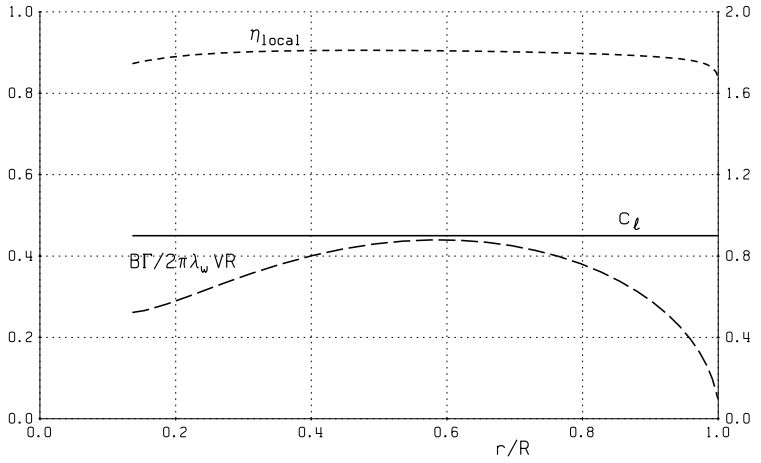

Figure 8.1. Spanwise lift distribution and efficiency for the first propeller blade design.

This is a good place to illustrate the low Mach numbers in which even the prop tip operates.. Again, based on this, it is emphasized that the incompressible approximation is very good here. Finally, note that C_L has been maintained constant at 0.9 along the blade. This was done for convenience, as it will allow one single airfoil to be used for the entire section of the blade. This saves both analysis and production time. Typically, one would specify the C_L at which L/D_{max} occurs for the specific airfoil used. The airfoil used here is the flat plate solution for simplicity, but does provide acceptable results.

8.2 Redesign

8.2.1 Motivation

Airfoil selection to further increase the performance of this propeller had begun, and identified the DAE-series airfoils for use on this propeller, when a final drag buildup for the aircraft was available. With this new information, it became clear that the prop had been optimized for a power output (380W) that was higher than the actual power required for level cruise at the aforementioned V_{cruise} = 33 ft/s. Simple application of the power Eq. (8.1)shows that even after a margin of safety was

#bld= 2	R m = 1.372	$\sigma_{3/4}$ = 0.0540	β_{twist}= 62.070	
Vm/s= 10.060	V/ΩR= 0.3891	P_C = 0.094	C_P = 0.0671	η_{ideal}= 0.9795
h km= 0.000	J = 1.2224	T_C = 0.086	C_T = 0.0502	η = 0.9149
T kN= 0.0314	P kW= 0.3449	RPM = 180.0	β_{tip} = 27.581	

Table 8.1. Performance characteristics of the rediesigned propeller

applied to a high drag estimate of $D = 7$ lbs, (pessimistic estimates are closer to 6.5 lbs), the power required P_{req} is significantly less than this.

$$P_{req} = DV_{cruise} = (7lb)(33ft/s) = 313W \tag{8.1}$$

8.2.2 Results

The same iterative design technique was followed for the new propeller, but the results showed slight efficiency improvement associated with the lower disc loading. The lift distribution and efficiency are shown for the redesigned blade in Fig. (8.2). This gives rise to the propeller performance characteristics summarized in Table (8.1). Although this blade shows a calculated efficiency of 91.49%, real world performance will be reduced, primarily due to the inboard shift of lift and the resulting large amount of twist specificed near the root of the blade. This is visually striking in Fig. (8.3).

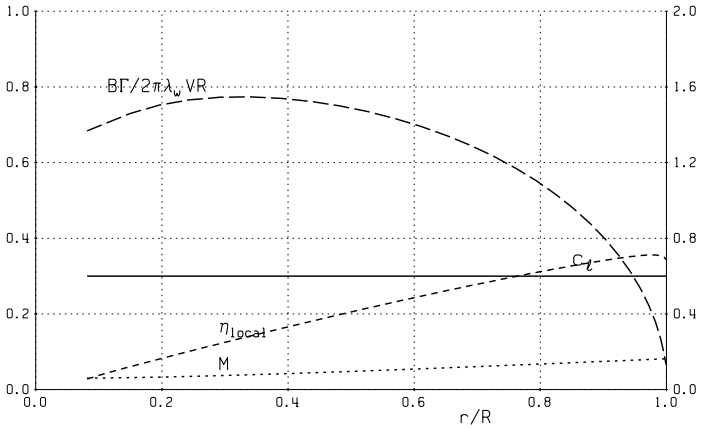

Figure 8.2. Spanwise lift distribution and efficiency for the redesigned propeller blade.

8.2.3 Off-Design Performance

Off-design point calculations were also performed, mainly for the takeoff case (thrust requirements during landing are somewhat relaxed relative to the other mission phases). To illustrate different

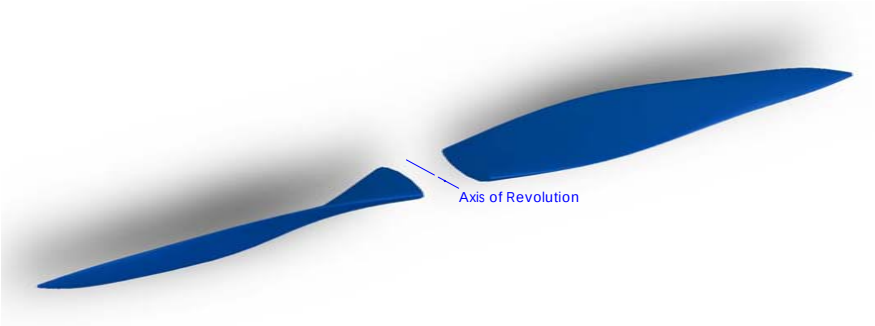

Figure 8.3. 3D CAD model of blades.

operating conditions, we introduce an advance ratio J and a power coefficient C_P as defined in (8.2) and (8.3), where where n is the rotation rate of the prop in rev/s, D is the diameter of the prop in ft, P is power delivered to the prop, ρ is air density, ω the prop angular rotation rate, and R the radius of the prop. A plot of efficiency contour lines and best blade angle contour lines versus these two parameters can be found in Fig. (8.4) and will form the basis for a prop pitch control strategy.

$$J = \frac{V}{nD} \tag{8.2}$$

$$C_P = \frac{P}{\pi\rho\omega^3 R^5} \tag{8.3}$$

8.3 Pitch Controller

8.3.1 Motivation and Constraints

John Langford, co-designer of the MIT Light Eagle human powered airplane, made the statement that the use of "automatic propeller pitch regulation was crucial" to the success of their design[28], a sentiment that we find repeated in other texts. In fact, MIT's Daedalus HPA project experimented with implementation of both a longitudinal and a lateral/directional autopilot to reduce pilot workload[29]. Without a pitch regulator, the propeller is not operating in the most efficient design area, and can waste considerable power, depending on the flight regime. Constraints on this controller were that it had to take two inputs (the freestream velocity and the prop speed), generate one output (blade angle), be lightweight (precluding the use of a traditional computer), and be easily adjusted for multiple users.

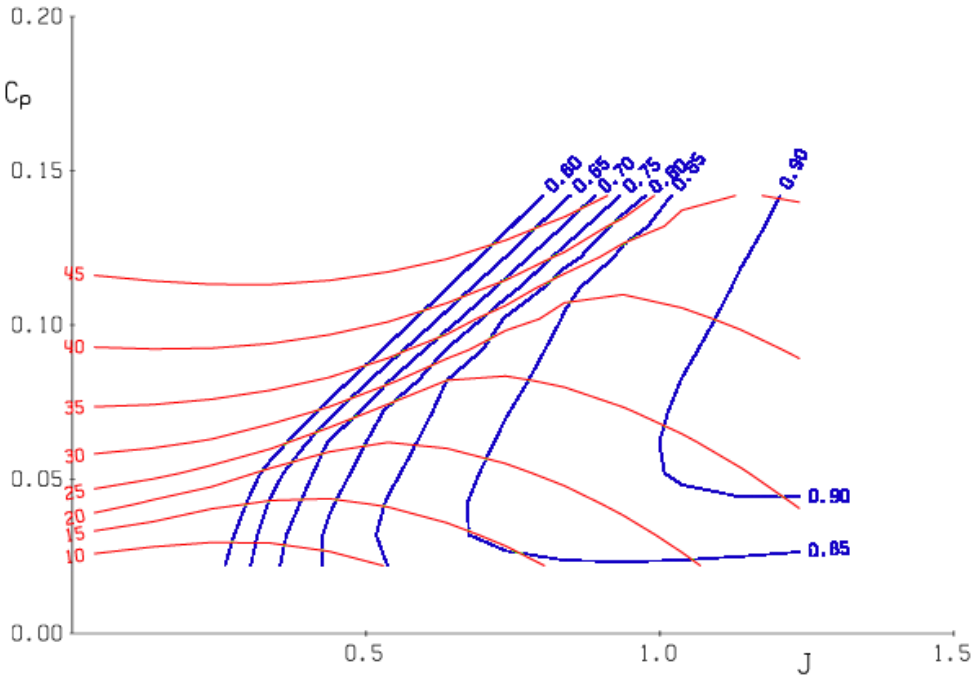

Figure 8.4. Off-design point operating calculations.

8.3.2 Controller Architecture

Accordingly, a two-input, single-output, prop pitch regulation controller was devised as shown in Fig. 8.5. In this controller, measurements are made of the freestream velocity V_M and the prop rotation rate. Measurement noise is assumed high frequency, so these signals are then passed through low pass filters to remove this noise and find the true velocity V and rotation rate.

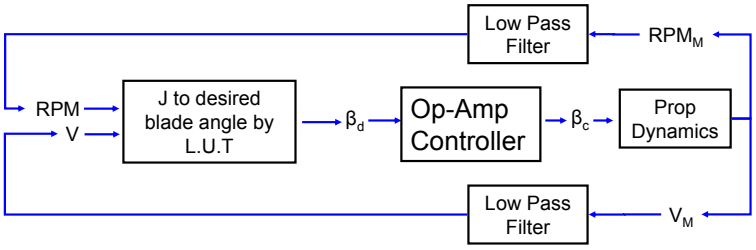

Figure 8.5. Pitch regulation schematic.

The freestream velocity and angular rotation rate can be nondimensionalized via the advance ratio J defined earlier in Eq. (8.2). A look-up-table (LUT) has been generated from efficiency plots such as the one shown in Fig. 8.4. In the pitch controller, this resides on a PIC microcontroller that calculates the advance ratio corresponding to the prop rotation rate and the airspeed, and outputs

a desired blade angle β_d, in the form of an analog voltage.

The desired blade angle is then passed to a traditional proportional-integral-derivative (PID) controller. For weight concerns, this has not been implemented on a digital platform, but is made of discrete components including operational amplifiers, resistors (both adjustable and fixed) and capacitors. The circuit used has been adapted from that shown in Fig. 8.6[30] by the addition of variable resistors to allow for customized user settings. The transfer function $H(s)$ for this compensator is shown in Eq. (8.4)[30], where R_i and C_j are specific resistances as identified in Fig. 8.6.

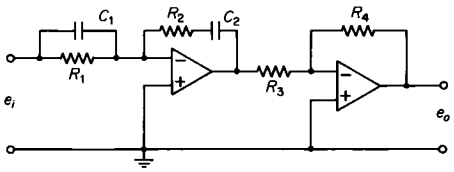

Figure 8.6. Operational amplifier controller.

$$H(s) = \frac{R_4}{R_3}\frac{R_2}{R_1}\frac{R_1C_1s+1}{R_2C_2s+1} \tag{8.4}$$

The output of this stage is the commanded blade angle β_c, which is passed to the servo controlling blade pitch. This servo does add some dynamics to the overall prop dynamics, but the aeroelastic interactions between blade flex and prop angle were outside the scope of this design and probably pretty small. Instead, experimental identification of the PID gains will be used from which the open-loop dynamics for the entire architecture can be found. Tuning of PID gains is a straightforward procedure, for which manuals are available, which is in contrast to aeroelastic research and nonlinear control theory, both of which are topics of current research.

The construction of the controller out of discrete components places it at approximately 30g in weight, not including batteries.

9. R/C Model Development

9.1 Motivation and Purpose

The team had originally planned to construct a full scale prototype of the aircraft; however, too many questions about the design remained and more work than the team thought possible was ahead to finish the prototype by graduation. The team still desired to construct something to prove the design would work and to work out kinks in the design so that a working full scale could built by a future team. The best option seemed to be to build a quarter scale model of the airplane. The model could validate many of the analysis methods used to create full scale design. It could

also answer questions on stability and control that were very difficult to analyze. The model was intended to help refine and improve the full scale design.

9.2 Scaling of the Model

9.2.1 Geometric and Dynamic Scaling

In order for the model to be of real engineering value, it had to be scaled properly. The approach described in NASA's "Similitude Requirements and Scaling Relationships as Applied to Model Testing" was used[31]. The report detailed methods of scaling designs for similarity. For the R/C model to fly dynamically similar to the full scale design, it had to be scaled by Froude number shown in Eq. 9.1. First the model had to be geometrically similar essentially meaning that all the dimensions had to be divided by the scaling factor. A table was included in the NASA report that gave the equations for similarity between properties of the model and full scale design based on the Froude scaling method. A quarter-scale model was chosen because it was most feasible to build adhering to the scaling laws. A 1/5 scale model was very stringent on wait and 1/3 scale model seemed too large. Table 9.1 shows the full scale dimensions versus the model dimensions. It may be noted that the wing thickness is not exactly scaled to one-quarter the thickness of the Iron Butterfly. This is because the Froude scaling does not guarantee that the airfoil will exhibit the same behavior. It is the job of the designer to find an airfoil that will perform on the model similarly to the airfoil on the full scale design.

$$Fr = \frac{V^2}{gl} \tag{9.1}$$

The effects of a property not scaled as described was not found in public literature. The equations were manipulated with the help of Bob Parks, an engineer experienced with model scaling. For example, through manipulation of the governing equations the effect of the weight on behavior in cruise can be found. If the model came in at twice the weight it is supposed to, then the speed it flies would have to be increased by approximately 41%. This can be seen in the example below:

$$C_L = \frac{2W}{\rho V^2 S} \tag{9.2}$$

$$V_1 = \sqrt{\frac{2W}{\rho S C_L}} \tag{9.3}$$

$$V_2 = \sqrt{2} V_1 \tag{9.4}$$

In order for the model to exhibit cruise dynamics similar to the full scale, the velocity would have to increase by the square root of 2 for twice the Froude scaled weight. If another parameter were the target, like turning radius, a similar analysis would have to be performed.

Parameter	Full Scale	Model
Wing Span [ft]	60	15
Wing Chord [ft]	1.5	0.375
Wing Thickness [in]	2.25	0.3294
Wing Gap [ft]	5	1.25
Wing Area [ft^2]	2160	11.25
Gap [ft]	5	1.25
Strut Chord [ft]	0.75	0.188
Stab arm [ft]	15.82	3.95
Stab span [ft]	7.64	1.91
Horiz. Area [ft^2]	99.96	0.52
Stab chord [ft]	1.09	0.27
Stab thickness [ft]	0.13	0.52
fin arm [ft]	18.12	4.53
fin span [ft]	11.95	2.99
Vert Area [ft^2]	245.28	1.28
fin chord [ft]	1.71	0.48
fin thickness [ft]	0.21	1.28
Speed [ft/s]	33.00	16.5
Weight [lb]	215	3.36

Table 9.1. Model v. Full Scale Dimensions

9.2.2 Power and Thrust for the Quarter-Scale Model

The scaling report did not mention anything on how to scale the power or thrust. Instead of trying to create a scaling method, the quarter scale power required was calculated. Using conservative drag estimates, the power required to maintain the cruise velocity in a 15 deg bank came out to only 3.8 W. From R/C experience, this value seemed very low. As a safety factor the propulsive efficiency was set to 0.5, a low value for electric R/C propulsion systems. With this power requirement in mind, hobby electric motors were researched. The smallest AXI outrunner motor available (AXI is pretty much the best motor for the power regime) was quoted as producing approximately 18W of power. This provided approximately 10 W of excess power in a 15 deg banked turn at scaled cruise speed.

These results were still looked on with some skepticism. To ease this doubt and to characterize the electric propulsion system, a wind tunnel test was conducted. The propulsion system was run by a Medusa Research test rig and mounted on a load cell feeding thrust data to the Medusa data logger. The data logger also recorded battery voltage and amperage. A series of tests were run from zero throttle to full throttle over a series of wind tunnel speeds covering the full range possible model velocities.

9.3 Model Aerodynamics

The power limitations of the full scale aircraft are not present in the design of the scale model so airfoil selection includes factors other than minimal drag. Therefore the largest consideration in model airfoil selection was performance similitude to the full scale, requiring matching of C_{l_α} between the full scale airfoil and the selected model airfoil. However, before this final agreement was considered, several smaller considerations such as stall margin and ease of construction.

The model will cruise at a velocity of approximately 16.5 ft/s and with a chord of only 4.5 in placing the Reynolds number in the realm of 40,000. This range of Re is considered very low and presents a new set of aerodynamic problems separate from the full scale. However, these problems have already been addressed by many aerodynamicists and studied extensively at the University of Illinois Urbana-Champaign by Dr. Selig, Dr. Gush, and Dr. Tehrani. This study involved the experimental analysis of a large list of low Re airfoils. The results of this study have been published through SoarTech Aero Publications with the complete list of the airfoils studied and associated Re published online[32]. By reviewing this list, several candidates were selected that were applicable to the Re range of the model.

With a list of candidates, several selection criteria were established: C_{lmax}, stall margin (change in AOA to stall), thickness, and ease of building. The model must fly at equal values of C_L so that the flight dynamics of the full scale aircraft are scaled. An analysis of each airfoil was performed using X-Foil to obtain lift and drag polars. From these polars and the C_{lmax} requirement, several candidates were eliminated. Because a model must be flown off visual indicators only, it becomes much harder to fly close to stall and so a larger difference between cruise AOA and stall AOA is required. This reduced the possible candidates to the Verbitski BE-50, the Morris GM15, and the Eppler 387. Looking at Table 9.2, it can be seen that the E387 has a small stall margin, but a large C_{lmax} keeping it a possible candidate. However, further X-Foil analysis revealed that at cruise conditions the separation bubble is unstable and rapid boundary layer changes result in sudden increases in drag and possible flow separation. This would have large consequences on the flight dynamics of the model eliminating the E387. This left the BE-50 and GM-15 for further consideration.

The model wings will be constructed from ribs and spars with a stress skin covering. This construction technique requires that the airfoil be thick enough to allow an adequate main spar and a trailing edge that can be accurately built without warping. Warping of the TE or the wing itself will have a detrimental effect on performance and reduce the correlation between model dynamics and full scale dynamics. The full scale aircraft will implement ailerons and thus so will the model. Ailerons require an airfoil that will allow room for hinging and control linkages. The Morris GM-15 has both the highest stall margin and highest C_{lmax}, but a thin TE. The fineness of the GM-15 TE does not allow room for the mechanics needed for the ailerons and will also present problems in constructing a warp free TE eliminating the GM-15.

Table 9.2. Comparisons of model airfoil candidates.

Candidate Designation	Clmax	AOA at Clmax	AOA at $C_l = 0.92$	Stall Margin [deg]	t/c	Camber	LE Radius	TE angle
A18 Archer	1.23	8.5	5.5	3	0.728	0.0384	0.0061	9.9
BE 50 Verbitski	1.32	10.5	4.5	6	0.0732	0.0395	0.006	5.85
E387 Eppler	1.27	10.5	8	2.5	0.09077	0.0378	0.0084	3.5
GM15 Morris	1.33	9.5	5.2	4.3	0.0674	0.0476	0.0046	20.9
MA409 Achterburg	1.15	8.5	5.5	3	0.0669	0.0333	0.0043	9.43
MB253515 Bame	NA	NA	NA	NA	0.1496	0.0241	0.0078	18.2
NACA 64A010 Champine	NA	NA	NA	NA	0.1	0	0.0068	12.58
SD8020 Selig-Donovan	NA	NA	NA	NA	0.101	0	0.006	7.8

With all the other candidates now eliminated it is necessary to asses the agreement between C_{l_α} of the full scale DAE series and the BE-50. X-Foil was again utilized to produce lift polars for the BE-50. By plotting the lift polar of the DAE 11 and the BE-50, Fig. 9.1, it can be seen that at the design cruise C_l there is good agreement in C_{l_α} that is required for similar flight characteristics.

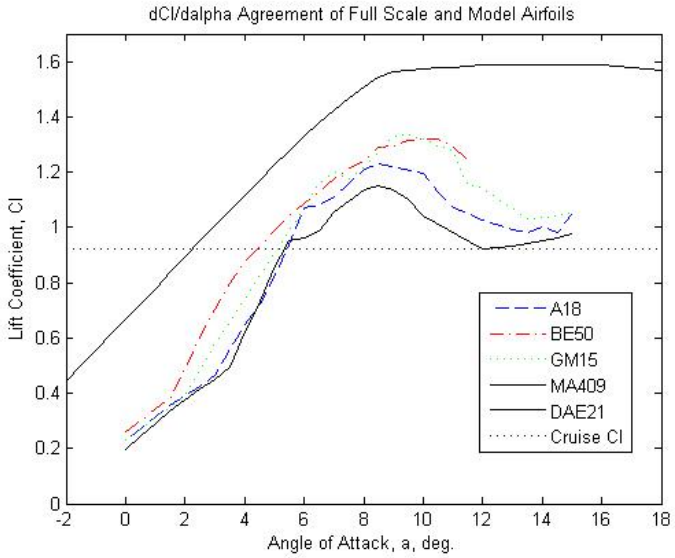

Figure 9.1. Comparison of lift curve slopes for model candidate airfoils to the DAE-11.

The BE-50 has several advantages over the other candidates both in terms of construction and aerodynamically. The airfoil is sufficiently thick for structure and ailerons. Additionally, the top of the airfoil has a large flat section that will allow the wing to be constructed inverted so each rib can be accurately aligned. Aerodynamically, the BE-50 has the lowest drag of the candidates and operates at its minimum drag during cruise in addition to comparable C_{l_α} with the full scale airfoil. This translates to reduced pilot effort to maintain constant cruise speed and reduces sensitivity to small throttle changes. For these reasons, the Verbitski BE-50 was chosen as the airfoil for the model.

9.3.1 Wing Development

With a final airfoil selected for use, the next step in the development of the wing design was defining the twist distribution to provide the most efficient lift distribution. I-Drag was used to compose an initial analytical model of the aircraft configuration, including flight conditions and develop a preliminary twist distribution. I-Drag was used to calculate the minimum induced drag and associated lift distribution for a simplified configuration. Though I-Drag was incapable of providing a final optimum lift distribution, it was useful in the endplate design to be discussed later.

The initial estimate for lift distribution from I-Drag was used to create a more complete AVL model with nine locations per half span, per wing, where the local twist is defined. The initial model was created by analyzing the I-Drag predicted distribution for inflection points and regions of linearity in $\frac{dC_l}{d_y}$. At this stage in wing development the end plates are aligned with the free stream and have zero twist. The AVL model was then run, under straight and level flight conditions, to calculate the lift distribution and associated downwash distribution. An iterative approach was then taken of adjusting the twist at the defined stations to load or unload the local section of the wing until a constant downwash was obtained. The twist was adjusted until the calculated wing efficiency was only showing a 0.5% change and then the model wing twist distribution was considered complete. The twist distributation is tabulated in Table 9.3

Table 9.3. Tabulated Model Twist Distribution

Span Location, [ft]	0	0.5	1	3	4	5	5.9	6.6	7.2
Top [deg]	-1	-0.7	0.2	1.4	0.5	0.2	-0.7	-2	-3.5
Bottom [deg]	2	2	2	1.7	0.5	0.5	-.7	-2	-3.5

Like the wing airfoil, the endplates operate at very low Re and so the low Re airfoil list generated for the main wing from the UIUC LSAT's was reviewed. Due to the low $C_{l_{req}}$ and the symmetric positive to negative loading, only symmetrical airfoils were considered. This left the NACA 64A10 and the SD8020 as the only candidates. The SD8020 was then chosen as the final candidate due to having lower drag. With the airfoil chosen and the desired loading known, the twist distribution was created by defining 5 stations over the endplate. The twist at each station was easily calculated with the use of an X-Foil calculated lift polar, Table 9.4. The twist was then added to the previous AVL model to complete the model wing design. Fig. 9.2

Table 9.4. Tabulated Model Endplate Twist Distribution

Vertical Location, [ft]	-1	-0.32	0	0.32	1
Twist, [deg]	3	2.4	0	-2.4	-3

9.3.2 Tail Design

The design of the model horizontal and vertical tail required a symmetrical airfoil capable of operating at very low Reynolds number. Once again the realm of small R/C gliders was explored to find a suitable airfoil. After reviewing several candidates the HT08 was selected. This airfoil was created by Mark Drela specifically for the purpose of full flying tail surfaces for low Re applications. This airfoil was designed to eliminate the 'dead band' common to full flying surfaces. This dead band is an area of unresponsiveness when deflection angles are low and can be problematic, particularly at low flight speeds. In addition the HT08 exhibits excellent drag qualities in that it has a low

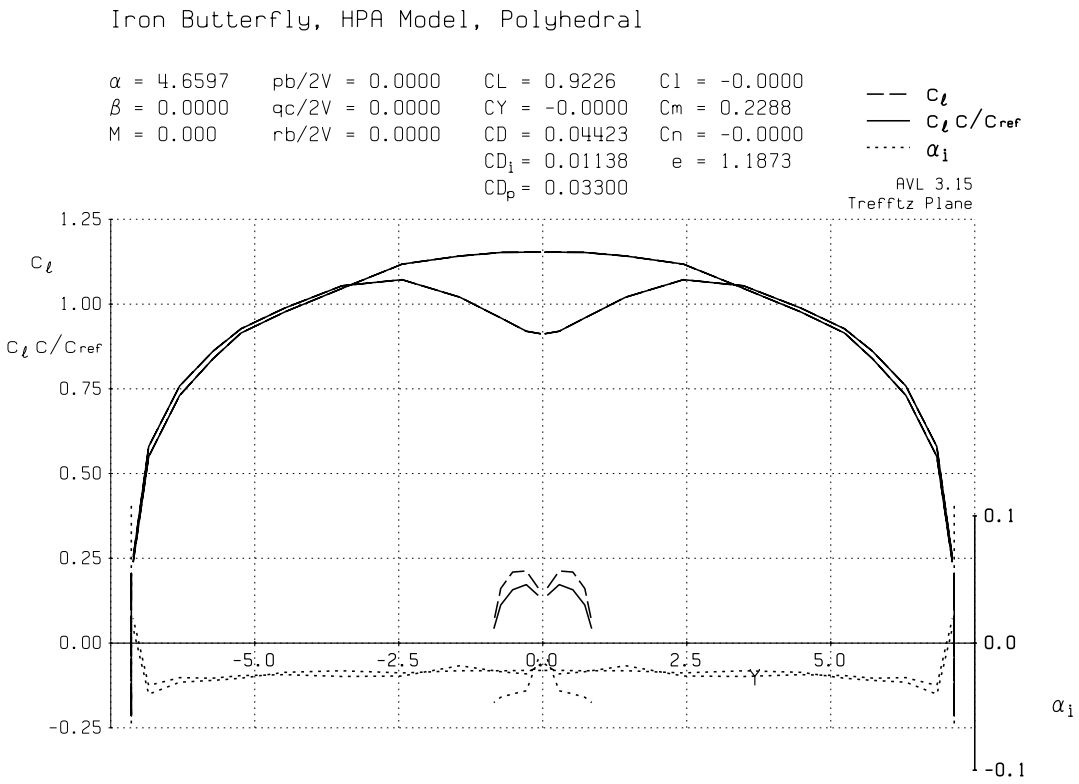

Figure 9.2. AVL Trefftz Plane Plot of 1/4 Model

profile drag, due to a t/c of 5%, low induced drag with a large bucket at the Re regime it will be operating.

With the airfoil chosen the next step was to size the tails. Here there were three main constraints that needed addressed. First was a span limit on the vertical tail to allow 8 deg. of rotation on take off. This limited the span to 37.6 in but was reduced to 36 in to allow construction with off the shelf material lengths. The next constraint was the aerodynamic constraint of limiting the tip Re to 25,000. This keeps the airfoil operating within its design specifications and minimizes unwanted aerodynamic effects from extremely low Re flow. Additionally there was a structural constraint requiring a minimum tip thickness of 0.125 inch. This is both to satisfy strength issues and thicknesses less than 0.125 inch becomes very difficult to accurately construct. With these constraints the following table was generated, Figure 9.5.

	AR	Root Chord	Tip Chord	Tip Re	Tip Thick.	Span
Horizontal	6	4.5	2.5	23,500	0.125	20.8
	6	**4.0**	**3.0**	**28,300**	**0.150**	**20.8**
	6	3.5	3.5	33,000	0.175	20.8
	7	4.0	2.5	23,500	0.125	22.4
	7	3.5	3.0	28,300	0.150	22.4
Vertical	6	8.5	3.5	33,000	0.175	36.0
	6	8.0	4.0	37,676	0.200	36.0
	6	**7.5**	**4.5**	**42,400**	**0.225**	**36.0**
	6	7.0	5.0	47,100	0.250	36.0

Table 9.5. Selection Analysis of Model Tail Size

Because only two geometric configuration of the horizontal tail can be eliminated with the defined constraints it became important to address considerations as well as constraints. The largest consideration is that the lift distribution of the tail is controlled by LE taper and not twist. It was for this reason that the horizontal tail was chosen to have a root chord of 4.0 in, tip chord of 3.0 in and a span of 20.8 in. The rudder was chosen to have a root chord of 7.5 in and tip chord of 4.5 in. With the model tail sizes finalized, the aerodynamic design of the model is complete and performance analysis can begin.

9.3.3 Performance Expectations

The performance of the model is dependant on two main things, the efficiency of the wing and cleanliness of the construction, i.e. minimal protrusions into the free stream. The efficiency of the wing can be accurately estimated with the use of AVL but the parasitic drag due to various protrusions is much harder to quantify without detailed wind tunnel tests and requires the performance of the final model to be defined in terms of an envelope as opposed to a single design point.

The induced drag of the wing, with non-lifting endplates, is reported by AVL to be C_{di} =

0.01165. The addition of the twisted endplates increases C_{di} to a value of 0.01138 to yield a 2.4% decrease in induced drag. This is a small change and a poorly constructed joint between the wing and the endplate could easily negate the decrease in induced drag so great care was required in building a clean junction. However, if flight test time allows for the testing of the model with the endplates removed, i.e. biplane configuration, the reported C_{di} is 0.01181. This means that the twisted endplate configuration should have 3.8% decrease in drag over the biplane and should be a large enough difference to be measurable with glide tests.

At this point only induced drag has been discussed but parasitic drag plays a very large role in the ultimate performance of the airplane. Assuming all hinging and control surface actuation is done internally so that the airplane is completely smooth, assuming all flow is laminar, and including interference effects at junctions, a base drag coefficient, C_{d_0} of 0.0213 is obtained. However, these assumptions are not completely valid in that the airplane will not be completely free of obtrusions to the free stream and there will be regions of flow that are completely turbulent. Using Friction-F to obtain C_f values for partially turbulent flow and using the Hoerner form factors a higher, and more expected, value of $C_{d_0} = 0.0327$ is obtained. Taking the added drag of control rods, horns, etc. into consideration, C_{d_0} is estimated at 0.376, allowing for a 15% increase in parasitic drag. This is significantly higher than the completely clean and laminar case but is felt to be much more plausible and is used to avoid over estimations or potential problems due to having too little power.

Unfortunately there is little that can be done to back-calculate induced and parasitic drag separately from total drag when performing the simple flight testing that is scheduled. One of the simplest ways to determine drag characteristics of an airplane is a simple power off glide test. The glide angle is directly related to the L/D through $\cot(\theta) = L/D$. Because the glide angle is easy to measure, L/D is the major performance parameter being tested. The completely clean, laminar, twisted endplate design has a L/D of 28. This represents the upper limit of the performance. Accounting for turbulence and free stream disruptions, yields an L/D of 19, representing the lower limit. This is clearly a large range, however, if the effectiveness of the twisted endplate is ignored and the C_{di} of the plain boxplane is used and still allowing for a 10% increase in the turbulent C_{d_0} from protrusions gives an L/D of 19.5. This will be the projected.

9.4 Structures

An ANSYS finite element model with material properties from the basswood model testing was used to size the spars for the remote control model combined with those from MATWEB. An average value of 1450 ksi for the modulus of elasticity and 0.3 for Poisson's ratio were used. The need for maximum bending rigidity led to a spar design with caps instead of a constant rectangular cross-section located at the point of maximum thickness in the wing, shown in Fig. 9.3. Cap thickness was limited by rib considerations. A certain percentage of material is necessary to connect the leading edge of the rib to the trailing edge together. Only finite thicknesses of hardwood

and balsa are produced by manufacturers. A standard thickness of 3/32 in provided adequate rib connection material and still provide significant material as far away from the neutral axis as possible for bending rigidity. Thus, only the spar cap width needed to be varied to attain the necessary bending rigidity. Only standard size widths, 1/32 in increments, were considered because of material availability. Struts were built out of wrapped carbon tubes available from www.graphitestore.com[33]. Due to time constraints, model gap was matched to provide the same gap to span ratio as Chrysallis[21]. This set the gap to 25 in.

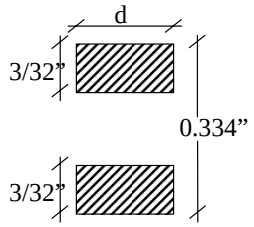

Figure 9.3. Spar cap sizing for remote control model structure.

Displacement-based analysis was used to size all spar caps for the model. For the wing, the distributed elliptic load specificed from aerodynamics was used at cruise conditions. Reasonable tip deflection was picked to be 5% of semi-span, requiring a 3 deg break built in at each panel to achieve the desired model polyhedral at cruise. This tip deflection was specified because it was known to be stiffer than necessary but able to produce a light enough wing. It was desired to reduce the aeroelastic tendancies of the model through stiffer components than what actually would be exhibited on the final aircraft. Aeroelastic testing was left as an exercise for another model. Final model spars were tapered from root to tip in finite sections. Each panel had constant cross-section spars for ease of construction and material availability. However, this “step” taper still provided a much lighter structure than constant cross section along the entire span. Each panel spar width, d, was varied along with strut wall thicknesses to get even deflections at each panel break so that final wing deflection at cruise matched the designed cruise state, mentioned in Section 5.7. Additional considerations were given to overal structural weight, sizing, and wing stiffness. Each panels cross-sectional spar dimensions are specified in the detailed drawings in the appendix.

A simpler sizing method was used for tail surface spars as they could easily be modeled as cantilevered beams. For a significant safety factor, the full lift at stall was applied as a tip load. Cross-sections were sized to keep tip deflections under 10%. The rudder used the same spar cap design as the wing, however the elevator used a rectangular cross-section since it was significantly thinner. Details for these spar cross-sections are also shown in the model detailed drawing in the appendix.

Figure 9.4. Cross-sectional layout of rudder rib, wing similar.

Figure 9.4 shows a cross section of the built-up method used for wing and rudder construction. Due to the elevator's size, the similar built-up method was not feasible. It was sanded out of balsa wood with a hardwood spar inset. Most secondary components were sized based on their general fit and available sizes. Often one thickness was too large, the next smaller size just right, and the next smallest way too small. For example, for wing ribs with a 4.5 in chord, 3/32 in was excessively large and heavy, 1/16 in provided adequate gluing surface and stiffness, and 1/32 in way too brittle and flimsy. Rib spacing was chosen to be 1.5 in, 3/8 of the chord, a good ballpark while still providing adequate aerodynamic shape. A more detailed cross-sectional layout is shown in the detailed model drawing in the appendix. Upon construction, it was found that this method for tail sizing significantly over-designed them. Tail sections could have been made lighter. However, their robust nature will make them more resilient during model testing although their weight aft will make balancing more difficult.

A detailed mass budget can be seen in Table 9.6. Component locations were taken using a datum 4 in in front of the nose, lined up with the tailboom shown in Fig. 9.5. All components were assumed to be point masses at their respective locations and center of gravity was calculated using simple moment balances. Current horizontal center of gravity is located at the desired $0.40\bar{c}$ and vertical center of gravity is right at the center of the two wings.

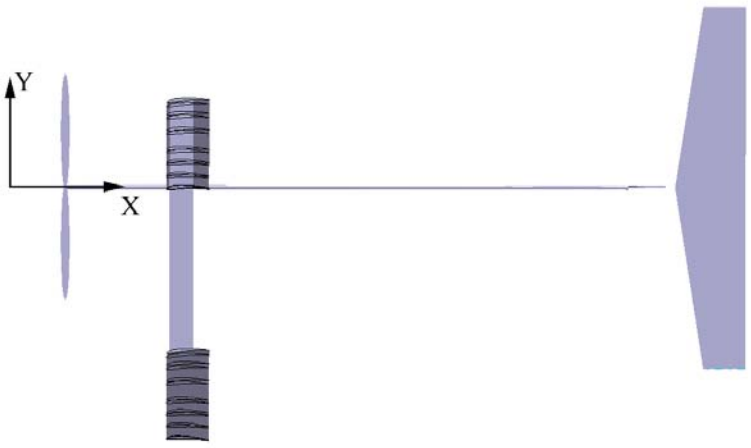

Figure 9.5. Coordinate system used for mass budget and CG calculations.

Table 9.6. Model Weight Breakdown

Component	Weight [oz]	X-Moment Arm [in]	Y-Moment Arm [in]
Wings w/o struts	23.94	22.6	-15.0
Struts - GraphiteStore AE001815	3.52	22.6	-12.5
Rear Angled Strut	0.41	31.7	-12.5
Tailboom - CST T585-40STD	2.22	31.0	0.0
Vertical Tail	2.50	77.2	0.0
Horizontal Tail	1.27	71.2	-2.4
Fuselage	4.00	17.5	-12.0
Landing Gear	1.50	22.6	-25.0
Motor - AXI 2204/54	0.86	4.0	0.0
Prop	0.26	4.0	0.0
Speed Control - CC Phoenix 25	0.59	8.0	-1.0
Batteries - Thunder Power TP1320-2S	2.05	12.0	-2.0
Receiver	0.94	13.0	-24.0
Aileron Servos - HS 55 x 2	0.54	22.6	-20.0
Rudder Servo - HS 81	0.52	16.6	-23.0
Elevator Servo - HS 81	0.52	16.6	-23.0
Nose Ballast	4.06	5.0	0.0
Fuselage Ballast	4.06	10.1	-25.0

9.5 Dynamic/Control Similarity

The 1/4 scale model was designed to preform dynamically similar to the full scale aircraft to test the non-standard control scheme. The static margin, elevator to trim in stall, control deflections, and time to bank are summarized in Table 9.7. The table indicates that there is little difference in the longitudinal characteristic as well as the control parameters. The model should behave similarly in longitudinal control, coordination of a turn, and banking.

	Iron Butterfly	Scaled Model
Static Margin	0.17	0.14
Trim in Stall δ_e [deg]	4.8	6.0
Turning δ_a [deg]	11.1	10.8
Turning δ_r [deg]	7.5	7.9
Turning β [deg]	3.3	8.3
Time to bank [sec]	1.6	1.1

Table 9.7. Comparison of stability and control of design and scaled model.

Tables 9.8 and 9.9 depicts a comparison between the longitudinal and lateral-directional dynamic modes of the model with those of the full scale aircraft. The tables indicate that the dynamic modes of the model are quite similar to the aircraft itself. The longitudinal modes share the form and

are comparable in time to half amplitude, frequency, and damping. Further, the lateral-directional dutch roll and spiral modes are fairly similar as well. The roll mode is significantly different. The time to half-amplitude occurs at about 1/10 of the time it would for the aircraft itself. Overall the scaling was successful, making the model dynamically similar to the Iron Butterfly.

Aircraft	Eigenvalue	Time to half [sec]	ζ	ω
Iron Butterfly	-34.7	0.02	-	-
	-5.3	0.13	-	-
	-0.072 + 0.74i	9.70	0.17	1.05
	-0.072 -7.4i	-	-	-
Scale Model	-10.1	0.07	-	-
	-4.0	0.17	-	-
	-0.17 + 1.0i	4.0	0.096	0.75
	-0.17 - 1.0i	-	-	-

Table 9.8. Eigenvalues and time to half amplitude for longitudinal dynamics

Aircraft	Mode	Eigenvalue	Time to half [sec]	ζ	ω
Iron Butterfly	Dutch Roll	-4.92+3.51i	0.14	6.04	0.81
	-	-4.92-3.51i	-	-	-
	Roll	-2.03	0.34	-	-
	Spiral	-0.06	11.6	-	-
Scale Model	Dutch Roll	-4.65+2.39i	0.15	5.23	0.89
	-	-4.65-2.39i	-	-	-
	Roll	-26.4	0.03	-	-
	Spiral	-0.089	7.84	-	-

Table 9.9. Eigenvalues and time to half amplitude for lateral-directional dynamics

9.6 Flight Testing Results

Just after sunrise on April 30, 2006, the Iron Butterfly quarter scaled model made eight flight attempts. In the first couple flights, the rudder was determined ineffective due to excessive flexibility in The tailboom in conjuction with the pull-pull control system. As a quick fix, guide wires attached the aft end of the tail boom to the inner wing struts, and the rudder was locked in a slight negative(left) deflection as an eyeball estimate to counter propeller torque. The plane was found to be very directionally stable. In most of the flights after the rudder was locked, the plane was observed to turn left regardless of the aileron input given by the pilot. This was attributed to two possible causes: the locked left rudder was overpowering the aileron input and the wing had become twisted during one of the landings. Furthermore, aeroelastic twisting of the flexible wing

in flight indicated that any effectiveness of the ailerons would probably result in excitation of the twisting aeroelastic mode and not impose a rolling moment for the aircraft. Over the eight flight tests, the pilot indicated that the elevator was very powerful and he needed very little input to obtain substantial response. The elevator was designed to require only 8 deg deflection to trim in stall, and therefore it is not unexpected to obtain good elevator authority. However, some of the effect may be due to the fact that the model was balanced slightly above the center of the wings which could cause it to be unstable at large positive angles of attack. For details see the discussion in Section 6.2 and Fig. 6.4. The pilot also noted that there was a very small pitch up margin to stall which was expected.

10. Conclusions

Currently the team stands with a nearly completed full scale design and a quarter scale model that could provide some very valuable flight test data with slight modifications. With stiffening the tail boom and rudder control linkage, the quarter scale model could be ready to provide some good drag and L/D data and will be able to validate the lateral and directional control. Next year's Virginia Tech Human Powered Aircraft Team can complete the model testing and then refine and change the current full scale design to construct a slower and lower powered full scale prototype. With this practice prototype, the team will be able to conduct flight testing to validate the design methodologies used and refine the full scale design. It will also offer a training platform for the competition pilot. A third team will then be charged with building a competition aircraft and winning the Kremer Sport Prize.

A1 Acknowledgement

The Human Powered Aircraft Group at Virginia Tech would like to thank the support of the Aerospace and Ocean Engineering Department faculty for support of the project. We extend special thanks to: the SGA for funding the development of our quarter-scale prototype; Dr. William Mason for significant guidance; Bob Parks, John Langford, Juan Cruz volunteering their extensive HPA knowledge; and students within the Architecture Department.

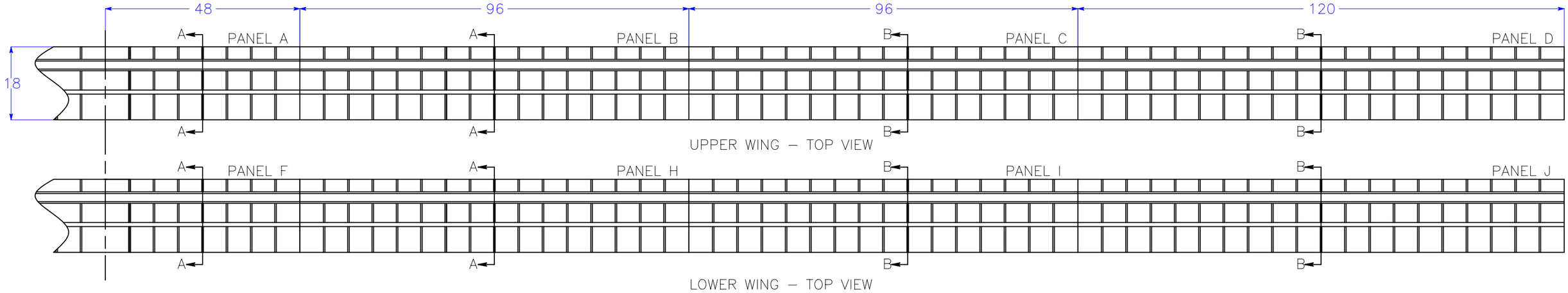

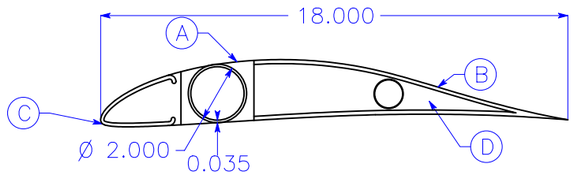

SECTION A–A

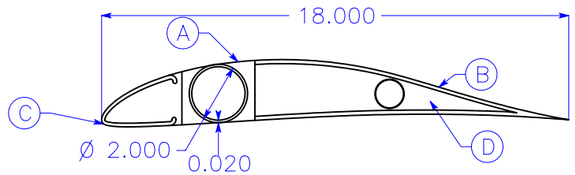

SECTION B–B

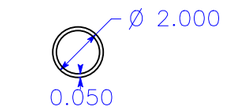

SECTION C–C

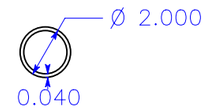

SECTION D–D

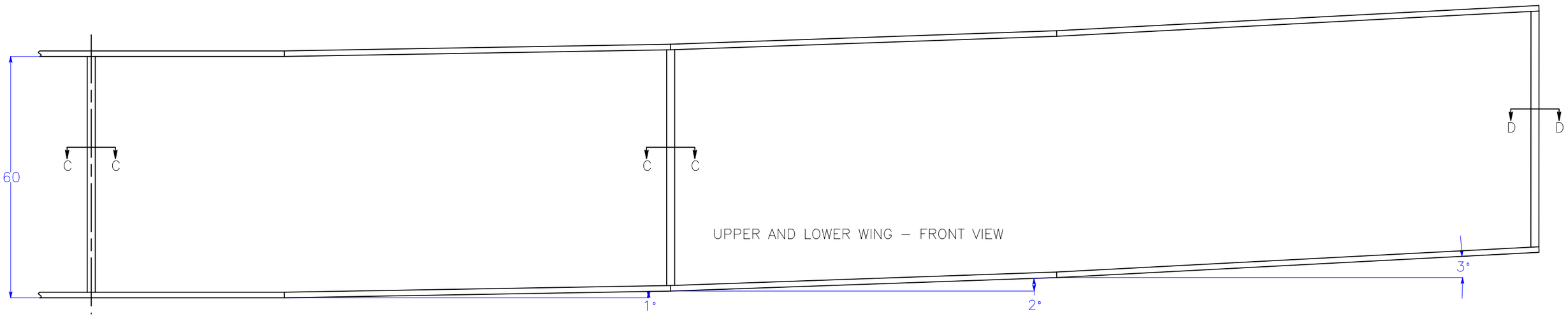

NOTES:
1) ALL SECTION VIEWS 1:6 SCALE
2) ALL OTHER VIEWS 1:24 SCALE
3) WINGS FLATTENED IN TOP VIEW
4) UPPER WING HAS SAME POLYHEDRAL AS LOWER WING
5) CARBON STRUTS FAIRED WITH HOTWIRE FOAM SECTIONS
6) PLANE SPAR AT POINT OF MAX THICKNESS

BALLOONS:
A) 1/64" PLY
B) 1/8" BALSA CAP STRIPS
C) HOTWIRED BEADED FOAM LEADING EDGE
D) FOAM RIBS

IRON BUTTERFLY FULL SCALE AIRCRAFT	
	DRAWN BY: BLAKE JEANS
	CHKD BY: LEE SKIDMORE
	CHKD BY: JASON ROADMAN
PG 1/2	APPRVD BY: CHRIS EMORY

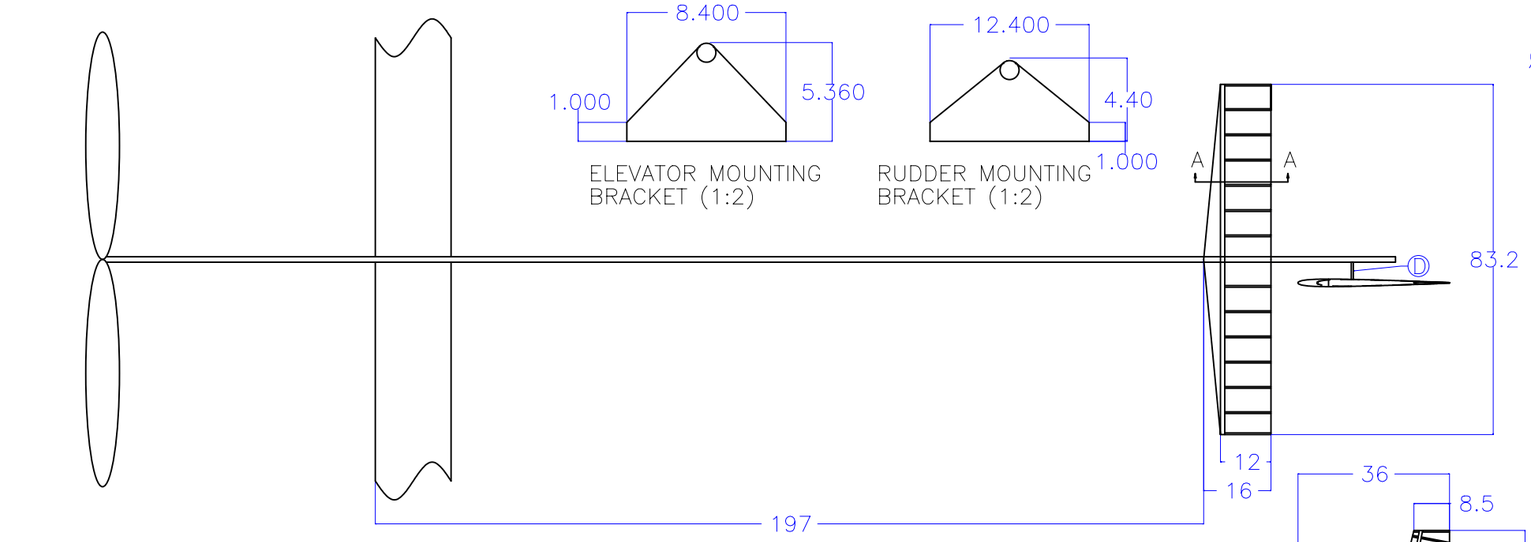

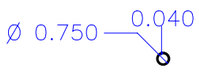

SECTION B–B

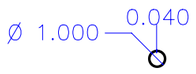

SECTION C–C

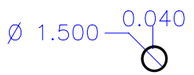

SECTION D–D

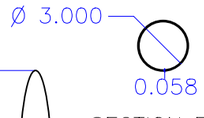

SECTION F–F

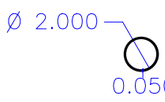

SECTION G–G

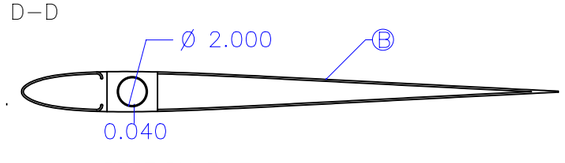

SECTION E–E

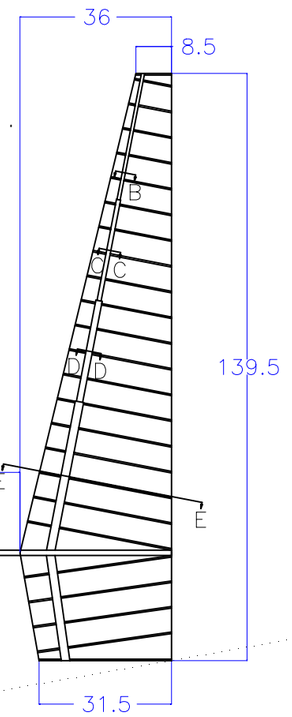

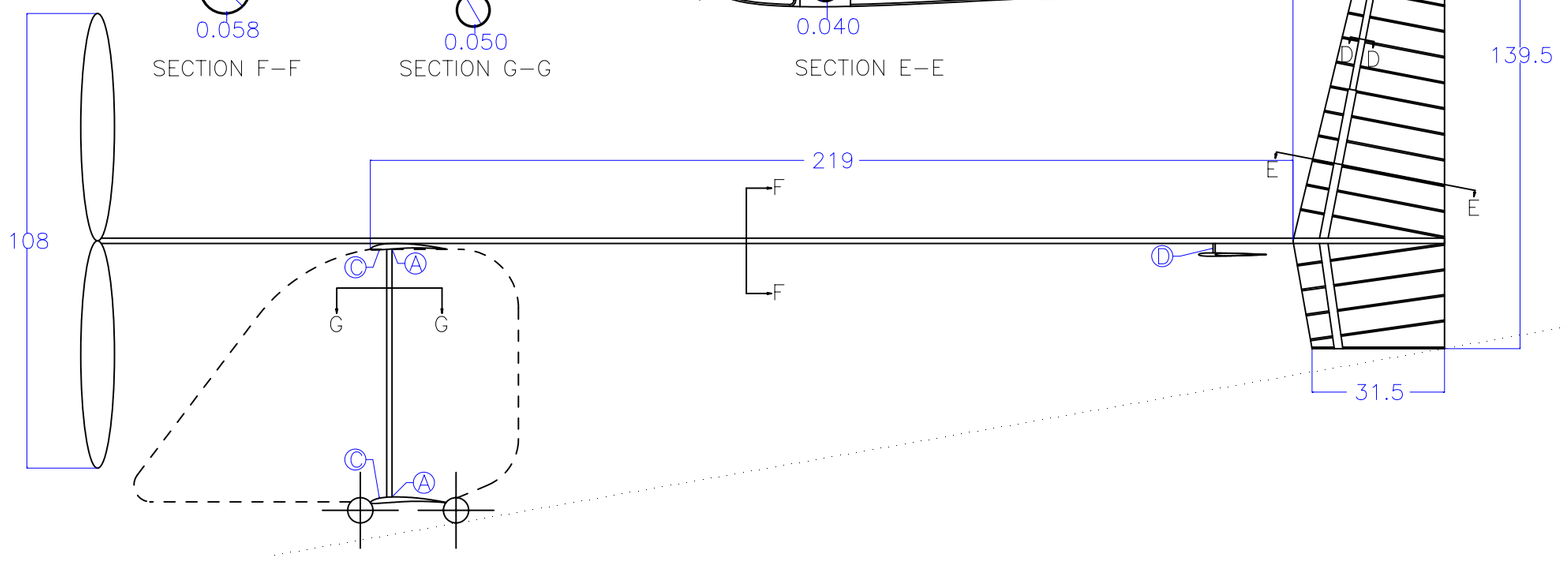

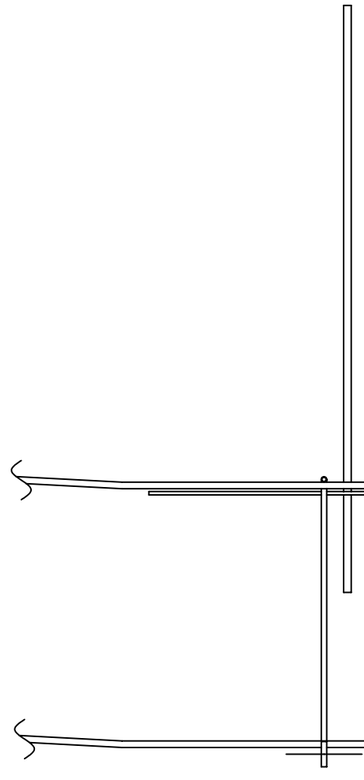

NOTES:
1) ALL SECTION VIEWS 1:9
2) TAIL SCRAPE ANGLE = 10 DEG

BALLOONS:
A) KEVLAR LASHING
B) HT14 AIRFOIL
C) 5 DEG INCIDENCE
D) SURFACES HINGED AT 23% CHORD

	IRON BUTTERFLY FULL SCALE AIRCRAFT	
SCALE: 1:36	PG 2/2	DRAWN BY: BLAKE JEANS

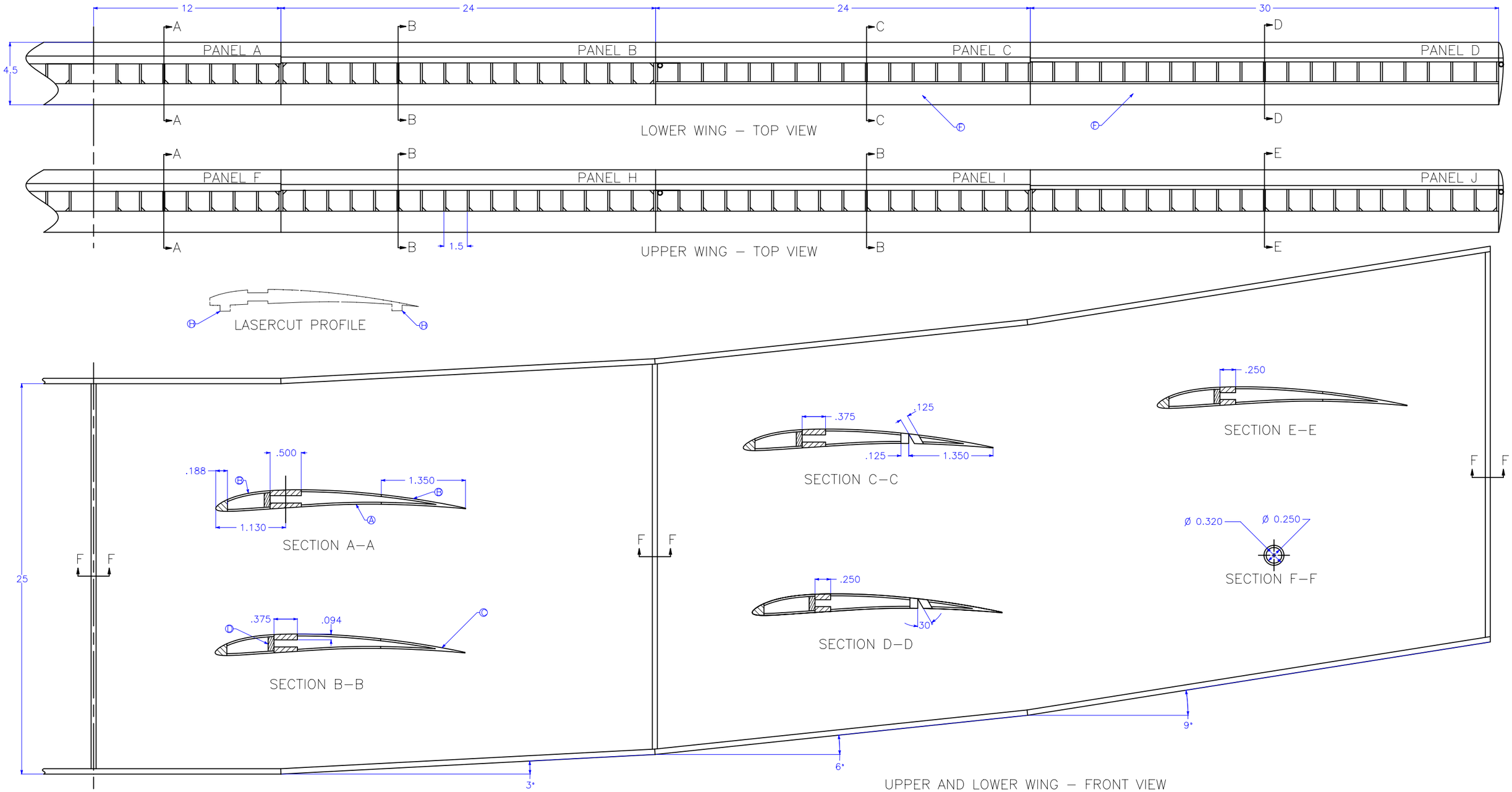

NOTES:
1) ALL SECTION VIEWS 1:1.5 SCALE
2) ALL OTHER VIEW 1:6 SCALE
3) WINGS FLATTENED IN TOP VIEW
4) UPPER WING HAS SAME POLYHEDRAL AS LOWER WING
5) CARBON STRUTS FAIRED WITH HOTWIRE FOAM SECTIONS

BALLOONS:
A) 1/32" CAP STRIP (1/8" WIDE)
B) 1/32" SHEETING
C) MODIFIED BE50 AIRFOIL
D) 3/32" VERTICAL GRAIN SHEAR WEB
E) ROLL–WRAPPED CARBON TUBE
F) AILERON
G) KEVLAR LASHING
H) ALIGNMENT TAB

IRON BUTTERFLY 1/4 SCALE RC MODEL

DRAWN BY: BLAKE JEANS

CHKD BY: LEE SKIDMORE

CHKD BY: JASON ROADMAN

PG 1/2

APPRVD BY: CHRIS EMORY

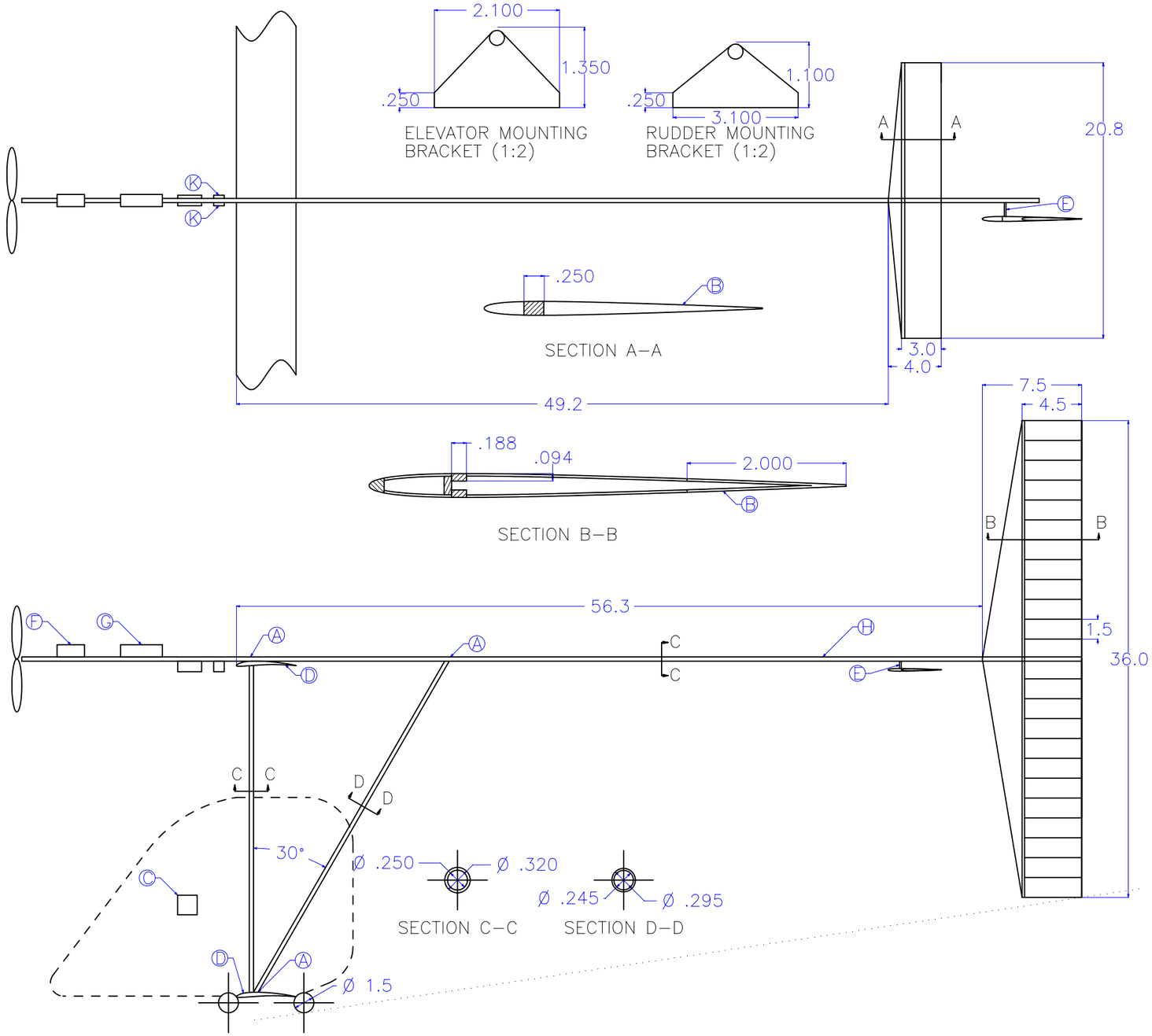

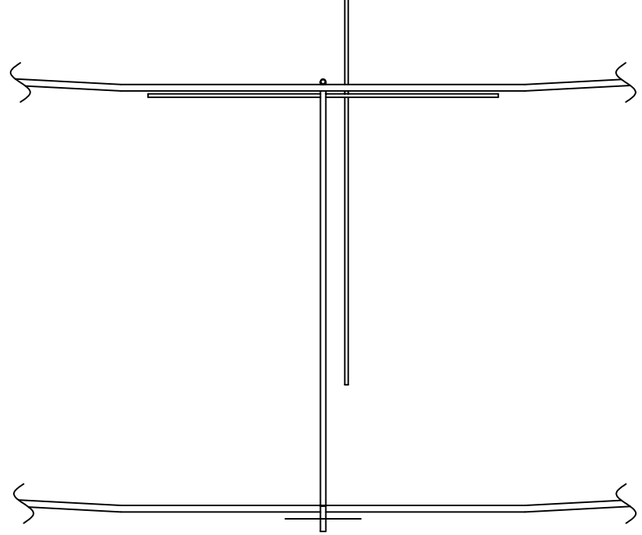

NOTES:
1) ALL SECTION VIEWS 1:1.5
2) TAIL SCRAPE ANGLE = 8 degrees

BALLOONS:
A) KEVLAR LASHING
B) HT08 AIRFOIL
C) ADJUST BALLAST FOR 3.36LB GTOW & CG
D) 5 DEG INCIDENCE
E) SURFACES HINGED AT 23% CHORD

PARTS LIST:
F) CASTLE CREATIONS PHOENIX 25 ESC
G) THUNDER POWER TP1320–25 LI–PO BATTERY
H) GST–T585–40STD TAPERED CARBON TUBE
J) AXI 2204/54 MOTOR
K) HS–81 SERVO

		IRON BUTTERFLY 1/4 SCALE RC MODEL
SCALE: 1:9	PG 2/2	DRAWN BY: BLAKE JEANS

References

[1] J. McIntyre. The Royal Aeronautical Society, Human Powered Flight Group. Avail at http://ourworld.compuserve.com/homepages/j_d_mcintyre/hpag.HTM.

[2] J.S. Langford. "A Human Powered Speed Aircraft Using Electrical Energy Storage". Master's thesis, Massachusetts Institute of Technology, 1984.

[3] J.D. Burke. "The Gossamer Condor and Albatross: A Case Study in Aircraft Design". *American Institute of Aeronautics and Astronautics Professional Study Series*, (AV-R-80/540), 1989.

[4] Hoerner S.F. *Fluid-Dynamic Drag; Practical Information on Aerodynamic Drag and Hydrodynamic Resistance*. Midland Park, 1965.

[5] M.M. Munk. "General Biplane Theory". NACA Report 151, National Advisory Committee for Aeronautics.

[6] J.A. Schetz. *Boundary Layer Analysis*. Prentice Hall, Upper Saddle River, NJ, 1993.

[7] M. Drela. "Aerodynamics of Human-Powered Flight". *Annual Review of Fluid Mechanics*, (22):93–110, 1990.

[8] "Nihon University Aero Student Group: Airfoil Database". Avail at http://www.nasg.com/afdb/show-airfoil-e.phtml?id=1180, 2005.

[9] Drela, M. "XFOIL Subsonic Airfoil Development System". Avail at http://raphael.mit.edu/xfoil/, 2000.

[10] Mason W. "Form Factor Comparison" Generated by request. Virginia Polytechnic Institute and State University.

[11] J. Grasmeyer. "I-Drag". Three FORTRAN programs avail at: http://www.aoe.vt.edu/ mason/Mason_f/MRsoft.html#idrag.

[12] Drela, M. "AVL Extended Vortex-Lattice Model". Avail at http://web.mit.edu/drela/Public/web/avl/, 2004.

[13] J.S. Langford. "The Daedalus Project: A Summary of Lessons Learned". *American Institute of Aeronautics and Astronautics, Inc.* Aurora Flight Sciences Corp.

[14] M.J. Patil. "AOE 3024 Thin-Walled Structures". Structual Ref., Virginia Polytechnic Institute and State University.

[15] M. Brungard. Effective Dihedral Calculator Tool. mabrungard@hotmail.com, avail at: http://www.charlesriverrc.org/articles/design/eda1.xls.

[16] P.F. Beer, E.R. Johnston, and J.T. DeWolf. *Mechanics of Materials*. McGraw Hill, New York, 3rd edition, 2001.

[17] Argyle industries, inc. source for aluminum extrusions avail. at http://www.argylein.com/, 2005.

[18] Aluminumwerk, unne-usa, inc. source for aluminum avail. at http://www.aluminiumwerk.com/, 2005.

[19] Tennessee metal services. source for aluminum avail. at http://www.eaglealloys.com/, 2005.

[20] D. P. Raymer. *Aircraft Design: A Conceptual Approach*. American Institute of Aeronautics and Astronautics, Inc., New York, 3rd edition, 1999.

[21] J.D. McIntyre. HPAG Information CD,. Royal Aeronautical Society.

[22] F.R. Whitt and D.G. Wilson. *Bicycling Science*. MIT Press, Cambridge, 1982.

[23] D. Ball, R.A. Ferguson, and A.J. Sargeant. "Effect of Muscle Temperature on Rate of Oxygen Uptake During Exercise in Humans at different Contraction Frequencies". *The Journal of Experimental Biology*, 205:981–987, 2002.

[24] H. Glauert. *Airplane Propellers*. Springer Verlag, Gloucester, MA, 1935.

[25] E. Eugene Larrabee. Practical Design of Minimum Induced Loss Propellers. *Society of Automotive Engineers Technical Paper Series*, April 1979.

[26] C.N. Adkins and R.H. Liebeck. Design of Optimum Propellers. *American Institute of Aeronautics and Astronautics 21st Aerospace Sciences Meeting,*.

[27] M Drela. X-Rotor Propeller Design Program. Massachusetts Institute of Technology.

[28] J. Langford. Interview on Sept 11. Aurora Flight Sciences, 2005.

[29] S.L. Sullivan R.B.and Finberg. The Flight Control System for the Daedalus Human Powered Aircraft. *American Institute of Aeronautics and Astronautics*, (89-3593), 1989.

[30] K. Ogata. *Modern Control Engineering*. Prentice Hall, Upper Saddle River, NJ, 4th edition, 2002.

[31] C. H. Wolowicz. "Similitude Requirements and Scaling Relationships as Applied to Model Testing". (1435), 1979.

[32] M. Selig, P. Gush, and K. Tehrani. "UIUC Low Speed Airfoil Tests". University of Illinois at Urbana-Champaign, http://www.ae.uiuc.edu/m-selig/uiuc_lsat.html, 2005.

[33] GraphiteStore.com. http://www.graphitestore.com.

[34] J.R. Cruz. "Weight Analysis of the Daedalus Human Powered Aircraft". Massachusetts Institute of Technology.

[35] J.R. Cruz and M. Drela. "Structural Design Conditions for Human Powered Aircraft". Massachusetts Institute of Technology.

[36] M. Drela. "Method for Simultaneous Wing Aerodynamic and Structural Load Prediction". *Journal of Aircraft*, 27(8):692–699, 1990.

[37] M. Drela. "Method for Simultaneous Wing Aerodynamic and Structural Load Prediction". *American Institute of Aeronautics and Astronautics, Inc.*, (89-2166), 1989.

[38] M. Drela. "Low Reynolds Number Airfoil Design for the MIT Deadalus Prototype". Massachusetts Institute of Technology.

[39] B. Etkin and Reid L.D. *Dynamics of Flight: Stability and Control*. John Wiley & Sons, Inc., Danvers, 3rd edition, 1996.

[40] E. B. Kasari. Flight Mechanics. In *Overview: Aircraft Design and Development*, 1973. Presented to Department of Navy Naval Air Systems Command by Virginia Polytechnic Institute and State University.

[41] I. Kroo. "Nonplaner Wing Concepts for Increased Aircraft Efficiency". Standford University, 2005.

[42] C. B. Millikan. "An Extended Theory of Thin Airfoils and it's Application to the Biplane Problem". NACA Report 362, California Institute of Technology.

[43] B.N. Pamadi. *Performance, Stability, Dynamics, and Control of Airplanes*. American Institute of Aeronautics and Astronautics, Inc., Reston, 2nd edition, 2004.

[44] E. Schoberl. "The Musculair 1 & 2 Human Powered Aircraft and Their Optimization". *The Technical Journal of IHPVA*, 1986. http://www.ihpva.org/HParchive/PDF/16-v5n2-1986.pdf.

[45] T. Shalon. "Design and Sizing of the MIT Daedalus Prototype". *American Institute of Aeronautics and Astronautics, Inc.*, (87).

[46] T. Smith. "Skycylce Design". URL translated with Google Translate http://kidachi.kazuhi.to/hpa/links.html.